

Bi-Based High T_c Superconducting Fibers by Melt Extraction

by

Jack J. Chang

Department of Physics, McGill University

Montréal, Québec

July 1991

**A Thesis submitted to the
Faculty of Graduate Studies and Research
in partial fulfillment of the requirements for the degree of
Master of Science**

© Jack J. Chang, 1991

Abstract

Bismuth-based high T_c superconductors were prepared from amorphous precursors made by melt-extraction. As-made amorphous fibers ranged from $0.7\text{ }\mu\text{m}$ to $100\text{ }\mu\text{m}$ in diameter and 0.2 cm to 5 cm in length. Fibers as thin as $1\text{ }\mu\text{m}$ in diameter were crystallized to form continuous filaments composed of single-grain chains.

Superconducting transitions at 105 K and 82 K were measured by SQUID magnetometry performed on annealed fibers of initial composition $\text{Bi}_{1.8}\text{Pb}_{0.2}\text{Sr}_2\text{Ca}_3\text{Cu}_4\text{O}_x$. X-ray diffractometry performed on annealed fibers revealed Bi-2212 ($T_c=85\text{ K}$) as the majority superconducting phase and Bi-2223 ($T_c=110\text{ K}$) as the secondary phase. The volume fractions of superconducting phases were estimated to have lower bounds of 30% for 2212 and 5% for 2223. Differential scanning calorimetry measurements made on as-made amorphous fibers indicate a glass transition at $T_g\approx 685\text{ K}$, followed by a series of exothermic peaks associated with the formation of precursor crystalline phases identified as the low T_c 2201 phase and a BCC Bi-Sr-Ca-Cu-O solid-solution with lattice parameter 4.25 \AA . Further work is required to determine the suitability of these new materials for applications such as multifilamentary conductors.

Résumé

Des supraconducteurs à haute température à base de bismuth sont obtenus à partir de précurseurs amorphes préparés par trempe rapide sur disque rotatif. Ainsi préparées, les fibres amorphes ont des diamètres de 0,7 à 100,0 μm et des longueurs de 0,2 à 5,0 cm. Ces fibres, d'un diamètre aussi petit que 1 μm , sont ensuite cristallisées par recuit afin de former des chaînes de monocristaux.

Des transitions supraconductrices sont observées à 105K et 82K par magnétométrie SQUID sur des fibres recuites de composition initiale $\text{Bi}_{1.6}\text{Pb}_{0.2}\text{Sr}_2\text{Ca}_3\text{Cu}_4\text{O}_x$. Par diffractométrie à rayons X, on a pu identifier la phase supraconductrice majoritaire comme étant Bi-2212 ($T_c=85$ K) et Bi-2223 ($T_c=110$ K) comme la phase secondaire. Les limites inférieures des fractions volumiques des phase supraconductrices ont été évaluées à 30% et 5% pour les phases 2212 et 2223 respectivement. Des mesures de calorimétrie différentielle à balayage effectuées sur les fibres amorphes détectent la présence d'une transition vitreuse à $T_g \simeq 685$ K, suivie par une série de pics exothermiques associée à la formation de phases précurtives cristallines identifiées comme étant une phase à basse T_c 2201 et un réseau CC de maille de 4,25 Å formé de la solution Bi-Sr-Ca-Cu-O. Une recherche plus poussée reste nécessaire afin d'évaluer les applications possibles de ces nouveaux matériaux comme conducteurs à multifilaments.

Contents

Abstract	ii
Résumé	iii
List of Figures	vi
List of Tables	viii
Acknowledgements	ix
1 Introduction	1
1.1 The High T_c Superconducting Oxides	3
1.1.1 The La-Ba-Cu-O compounds	3
1.1.2 The Y-Ba-Cu-O compounds	4
1.1.3 The Bi-Sr-Ca-Cu-O compounds	5
1.2 Physical Properties	7
1.3 Sample Preparation Techniques	7
1.3.1 Solid State Method	7
1.3.2 Rapid Solidification	8
1.3.3 Fibers, Tapes, and Wires	9
1.3.4 Melt Extraction Technique	9
2 Background: High T_c Superconductivity	10
2.1 Phenomenology and Theory	11
2.1.1 Meissner Effect	12
2.1.2 London Theory	12
2.1.3 BCS Theory	13
2.1.4 Ginzburg-Landau Theory	13
2.1.5 Type II Superconductors	14
2.2 Current High T_c Theories	16
2.3 The Bi-Sr-Ca-Cu-O Crystal Structure	18
2.3.1 The Structural Series	18
2.3.2 Chemical Disordering and Defects	21
2.4 Initial Compositions and Heat Treatment	22

3	Experimental Method	24
3.1	Precursor Production	24
3.2	Fiber Production	26
3.3	Heat Treatment	29
3.4	Differential Scanning Calorimetry (DSC)	29
3.5	X-Ray Diffractometry (XRD)	32
3.6	Scanning Electron Microscopy (SEM)	34
3.7	Transmission Electron Microscopy (TEM)	34
3.8	SQUID Magnetometry	34
3.9	Resistance Measurements	35
4	Results and Discussion	38
4.1	As-Made Amorphous Fibers	39
4.1.1	X-Ray Diffraction Analysis	39
4.1.2	SEM and TEM Studies	43
4.2	Precursor Crystalline Phases	50
4.2.1	DSC Analysis	50
4.2.2	XRD Analysis	52
4.3	High T_c Phases	57
4.3.1	Lead-Free Initial Compositions	57
4.3.2	Lead-Substituted Initial Compositions	57
4.3.3	SEM analysis	64
4.3.4	TEM Analysis	68
4.3.5	SQUID Magnetometry	77
5	Conclusions	80
	References	83

List of Figures

1.1	Crystal structure of lanthanum barium copper oxide ($La_{2-x}Ba_xCuO_4$).	4
1.2	Crystal structure of yttrium barium copper oxide ($Y_1Ba_2Cu_3O_7$) . . .	5
2.1	Meissner effect in a superconducting sphere cooled in a constant applied magnetic field.	12
2.2	Magnetization versus applied magnetic field for a bulk <i>type I</i> superconductor exhibiting a complete Meissner effect.	15
2.3	Superconducting magnetization curve for a bulk <i>type II</i> superconductor.	15
2.4	Crystal structures of the Bi-Sr-Ca-Cu-O oxides	20
3.1	Schematic diagram of the melt-extraction fiber casting system.	27
3.2	Schematic diagram of the Perkin Elmer DSC-2c Differential Scanning Calorimeter	31
3.3	Schematic diagram of the Nicolet-Stoe L11 Powder Diffractometer. . .	33
3.4	Plot of resistance vs. temperature for annealed fibers coated with silver paste.	37
4.1	SEM micrograph of an average sampling of fibers.	40
4.2	Enlargement of the thin fiber visible in Figure 4.1.	40
4.3	SEM micrograph of fiber exhibiting bulbous features.	41
4.4	X-ray diffraction pattern of 2:2:2:3 as-made fibers	42
4.5	Phase diagram showing the glass forming region of the $BiO_{1.5}-Ca_{0.5}Sr_{0.5}-CuO$ system.	44
4.6	SEM micrograph of as-made fiber with dark spots.	45
4.7	SEM micrograph of as-made fiber with rough regions.	45
4.8	SEM EDX spectra of smooth region on as-made 2:2:2:3 fibers.	47
4.9	SEM EDX spectra of dark spot on as-made 2:2:2:3 fibers.	48
4.10	SEM EDX spectra of rough region on as-made 2:2:2:3 fibers.	48
4.11	TEM EDX spectra of amorphous fragment from as-made 2:2:2:3 fibers. .	49
4.12	TEM EDX spectra of crystalline fragment from as-made 2:2:2:3 fibers. .	49
4.13	DSC isochronal run performed on 2:2:2:3 amorphous fibers.	51
4.14	XRD patterns for DSC samples at key points on the isochronal curve. .	53
4.15	XRD patterns for 2:2:2:3 fibers held isothermally at 810 K for 1 hour, scanned to 880 K and quenched, and held isothermally 880 K for 1 hour. .	56

4.16 SEM micrograph of a 1 μm Bi-Sr-Ca-Cu-O fiber crystallized into a continuous filament with single-grain chains.	58
4.17 XRD patterns of annealed 2:2:2:3, 2:2:3:4, and (1.8:0.2):2:3:4 fibers (1135 K for 3 hours)	60
4.18 XRD patterns for (1.8:0.2):2:3:4 fibers annealed at 1135 K for 1, 3, 6, and 12 hours.	61
4.19 XRD patterns for (1.8:0.2):2:3:4 fibers annealed at 1135 K for 14.5 hours.	62
4.20 XRD pattern of (1.8:0.2):2:3:4 pellet annealed at 1145 K for 9 days.	63
4.21 SEM micrograph of (1.8:0.2):2:2:3 fibers annealed for 1 hour at 1135 K.	65
4.22 SEM micrograph of (1.8:0.2):2:2:3 fibers annealed for 3 hours at 1135 K.	65
4.23 SEM micrograph of (1.8:0.2):2:2:3 fibers annealed for 6 hours at 1135 K.	66
4.24 SEM micrograph of (1.8:0.2):2:2:3 fibers annealed for 12 hours at 1135 K.	66
4.25 SEM EDX spectra for thin grain in annealed (1.8:0.2):2:2:3 fibers.	67
4.26 SEM EDX spectra for thick grain in annealed (1.8:0.2):2:2:3 fibers.	67
4.27 TEM EDX spectra of 2212 crystal grain found in annealed (1.8:0.2):2:3:4 fiber.	70
4.28 TEM EDX spectra of 2223 crystal grain found in annealed (1.8:0.2):2:3:4 fiber.	70
4.29 TEM EDX spectra of calcium and copper rich crystal grains found in annealed (1.8:0.2):2:3:4 fiber.	71
4.30 TEM EDX spectra of calcium and copper (mixed) crystal grains found in annealed (1.8:0.2):2:3:4 fiber.	72
4.31 TEM EDX spectra of calcium, and copper, strontium rich crystal grains found in annealed (1.8:0.2):2:3:4 fiber.	73
4.32 HRTEM lattice fringe image of crystal grain containing superconducting phases.	73
4.33 HRTEM lattice fringe images of 2212 (a) and 2223 (b) crystal grains found in annealed (1.8:0.2):2:3:4 fiber.	74
4.34 TEM diffraction patterns of 2212 (a) and 2223 (b) crystal grains found in annealed (1.8:0.2):2:3:4 fiber.	75
4.35 HRTEM lattice fringe image showing incommensurate modulation in the a-b plane in a 2212 crystal grain	76
4.36 TEM diffraction pattern showing satellite spots due to incommensurate modulation in the a-b plane in a 2212 crystal grain	76
4.37 Magnetization curve for (1.8:0.2):2:3:4 fibers annealed at 870°C for 12 hours.	78
4.38 Magnetization curve for (1.6:0.4):2:2:3 fibers annealed at 870°C for 12 hours.	79

List of Tables

2.1	The Bi-Sr-Ca-Cu-O family of superconductors.	18
2.2	Lattice parameters of the Bi-Sr-Ca-Cu-O family.	19
3.1	Powders used to prepare precursors pellets.	25
4.1	SEM EDX microanalysis of as-made 2:2:2:3 fibers.	46
4.2	Miller indices, d-spacings, and CuK α scattering angles for the BCC solid-solution.	54
4.3	Composition of 2212 and 2223 crystal grains found in annealed (1.8:0.2):2:3:4 fibers.	68

Acknowledgements

Many people have helped me in the completion of my thesis. I would first like to thank my supervisor John Ström-Olsen for providing me with this project and guiding me through the course of my work. For their technical assistance, I would like to express my gratitude to Peter Rudkowski for pioneering the melt-extraction technique and assisting me in adapting his setup for use in my work, Grazina Rudkowska for sharing her knowledge of melt-extraction of fibers and providing the beautiful SEM photos for my thesis, Alicja Zaluska for the meticulous TEM work she performed on my samples, Xu Yan for her assistance with X-ray diffractometry, Mao Ming for his help with DSC characterization, Pascal Tessier for breaking ground in high T_c research at McGill and sharing his experience with the Bi-Sr-Ca-Cu-O compounds, Julian Cave for performing the SQUID analysis on my annealed fibers, and Frank van Gils for his *Mr. Fix-it* abilities in the laboratory.

For patiently answering all my questions, I express my gratitude to Steve Brauer, without whose help I would have spent countless hours scratching my head in bewilderment. Geoff Soga's comradery and Zen-like influence have greatly touched my life. Ross Thomson's age-old wisdom and artistic prowess have been an inspiration to me. Together, they have made my stay at McGill an enriching and fulfilling experience.

The administrative hell that comes with being a student was made much less painful with the help of Diane Koziol, Betty Pedersen, and Paula Domingues. Martin Lacasse was of immeasurable help in my many battles with the ~~Superconductors~~ \TeX monster and took time out from studying for the preliminary exam to translate my abstract for me.

Finally, to Karen, who brought great change to my life during my first year-and-a-half in Montréal, I wish nothing but the best for the future. And to Jane, who provided me with the incentive to finish on (even ahead of) schedule, I wish happiness and success in the coming years.

Chapter 1

Introduction

Superconductivity was first discovered in mercury by Kamerlingh Onnes (1911), shortly after he liquified helium. The temperature at which mercury becomes superconducting (the critical temperature, T_c) is 4.1 K, very near the boiling point of helium. Subsequently, other materials were discovered to be superconducting with the highest T_c 's generally in the intermetallic compounds of niobium. A slow but steady rise in T_c took place over the years resulting in a T_c of 23 K for Nb_3Ge in 1975.

In 1986, the discovery of superconductivity in oxides based on copper and rare and alkaline earths by K. Alex Müller and J. Georg Bednorz infused great excitement into a field that had long been stagnant (Bednorz and Müller, 1986). Their La-Ba-Cu-O compound superconducts at 35 K, the highest known T_c at the time. Since then, many new superconducting copper oxides have been discovered, with ever increasing chemical and structural complexity. The most notable are the Y-Ba-Cu-O compound, the first to superconduct above the boiling point of liquid nitrogen (77 K) (Wu *et al.*, 1987), the Bi-Sr-Ca-Cu-O compounds ($T_c=85\text{ K}$ and $T_c=110\text{ K}$) which contain no rare earths (Mæda *et al.*, 1988), and the Tl-Ba-Ca-Cu-O compound which is the current record holder at $T_c=120\text{ K}$ (Sheng and Hermann, 1988).

The early push to attain higher critical temperatures has been superceded by the need to solve the applications problem: *How does one get these ceramics into a form suitable for use in devices?* Most work has centered on the Y-Ba-Cu-O com-

pound because it was the first 77 K superconductor. Progress with Tl-Ba-Ca-Cu-O is hindered by the toxicity and volatility of thallium. However, the Bi-Sr-Ca-Cu-O compounds are promising since they can be produced via the glass-precursor route by first forming them in an amorphous state by rapid solidification. Tapes and wires can be formed using rapid solidification techniques and subsequently converted to the superconducting crystalline phases. The high density and homogeneity of the amorphous precursors aid the formation of the superconducting compounds.

This thesis describes the use of one such rapid solidification technique, namely *melt extraction*, to produce amorphous thin fiber precursors of Bi-Sr-Ca-Cu-O which are annealed into the superconducting crystalline phases. The amorphous precursors and crystalline final products were characterized and an attempt was made to understand the process by which the final products are formed. The purpose of this work is to demonstrate that superconducting Bi-Sr-Ca-Cu-O fibers can be produced using the *melt extraction* technique to form the amorphous precursors. It is hoped that this material may prove suitable for use in fabrication of multifilamentary conductors or similar applications.

1.1 The High T_c Superconducting Oxides

Although a vast number of different high temperature superconducting compounds have been discovered, all have common structural, chemical and electronic properties, the most important of which is that they are all based on copper-oxide planes. Superconductivity is believed to occur in two-dimensional copper-oxygen arrays based on the joining of CuO_4 squares at their oxygen corners to form CuO_2 planes (Cava, 1990a). The superconducting CuO_2 planes are separated by charge reservoir layers which act to control the charge on the superconducting planes through the transfer of holes or electrons (via chemical doping). The critical temperature is highly dependent on the charge carrier concentration. The crystal structures of these compounds are very complex, but all the known superconductors can be derived by stacking different amounts and sequences of rock salt and perovskite-like layers¹ with cation content consisting of rare earths or metals and oxygen completing the crystal structure (Cava, 1990a).

1.1.1 The La-Ba-Cu-O compounds

The simplest high temperature superconductor is the original La-Ba-Cu-O compound discovered by Bednorz and Müller with chemical formula $\text{La}_{2-x}\text{Ba}_x\text{CuO}_4$ where $x=0.15$ for the highest critical temperature, $T_c=40$ K (Yvon and François, 1989).² Figure 1.1 shows a schematic drawing of the La-Ba-Cu-O crystal structure. The lanthanum and barium atoms can occupy the same sites within the crystal lattice forming a solid solution. This chemical disorder is necessary in order for superconductivity to be present in the material. The effect of the substitution of barium for lanthanum is

¹A perovskite block can be modelled as a cube with a large metallic cation at the body center (e.g. La in La-Ba-Cu-O) and smaller metallic cations at the corners (Cu). Oxygen atoms occupy the midpoints of the cube's edges. It can also be viewed as a collection of polyhedra where the Cu atoms are located at the center of eight corner-linked octahedra with oxygen atoms at the vertices (Hasen, 1988).

²Barium can be replaced by strontium or calcium as the dopant.

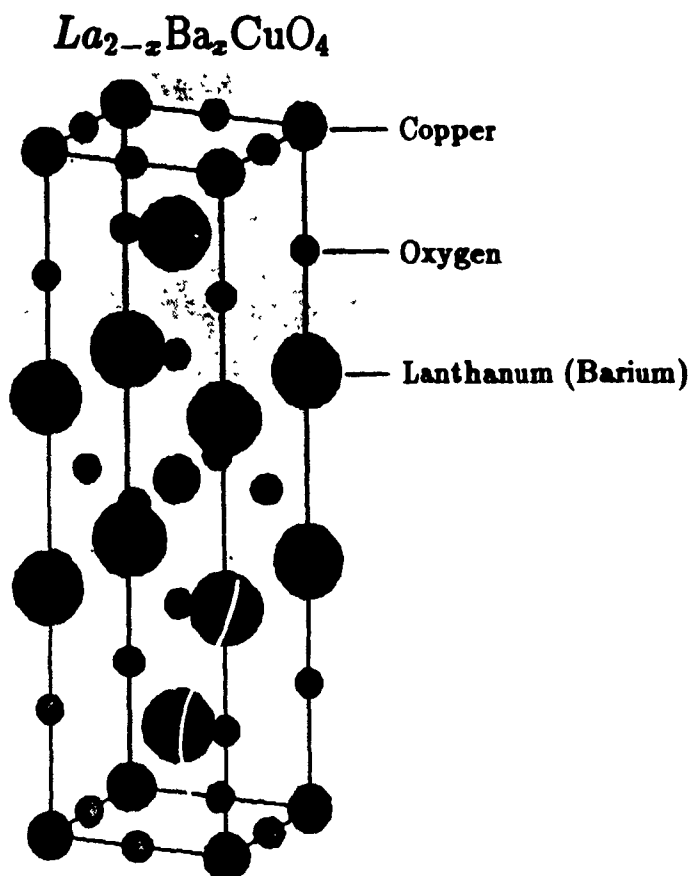


Figure 1.1: Crystal structure of lanthanum barium copper oxide ($La_{2-x}Ba_xCuO_4$).

to alter the valence of the copper atoms so as to optimize the concentration of charge carriers in the copper-oxide planes.

1.1.2 The Y-Ba-Cu-O compounds

The yttrium barium copper oxide superconducting compound is the most thoroughly studied, mainly because it was the first to superconduct above 77 K with a T_c of 93 K. It is known as the *123-phase* for its chemical composition: $Y_1Ba_2Cu_3O_7$. In contrast to the solid solutions that make La-Ba-Cu-O superconducting, the Y-Ba-Cu-O compound has a fully ordered crystal lattice consisting of planes of yttrium, barium, and copper ions as shown in Figure 1.2. The seven oxygen atoms in Y-Ba-Cu-O are crucial for superconductivity since the insulator $Y_1Ba_2Cu_3O_6$ is formed when the carrier concentration is changed by reducing the oxygen content to six. When the

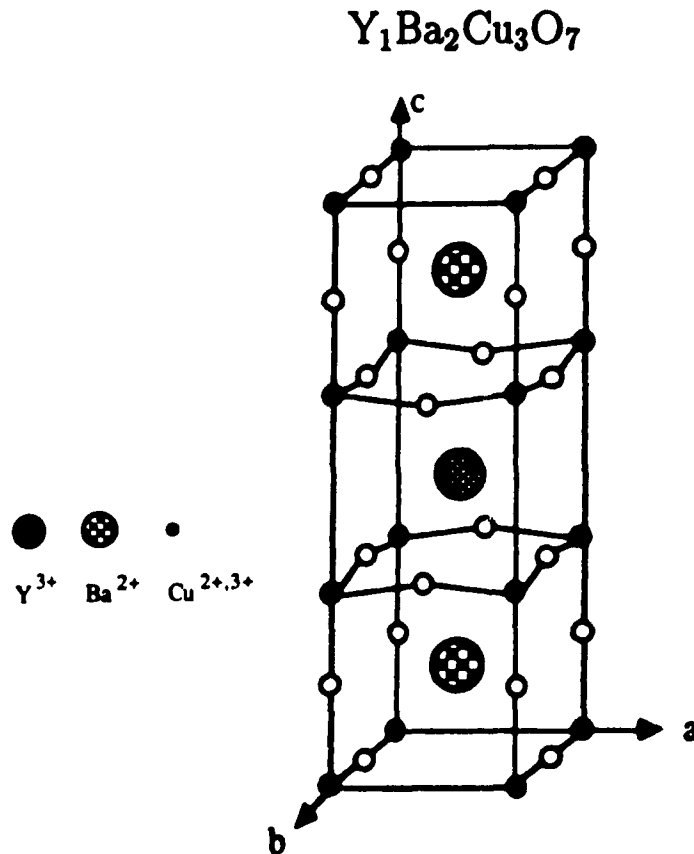


Figure 1.2: Crystal structure of yttrium barium copper oxide ($\text{Y}_1\text{Ba}_2\text{Cu}_3\text{O}_7$) (taken from Tiets *et al.* (1989)).

oxygen content reaches a level where on average 6.5 oxygen atoms are available for every three copper atoms, superconductivity is restored with $T_c=60$ K. As the oxygen content is further increased, T_c increases to above 90 K (Cava, 1990b).

1.1.3 The Bi-Sr-Ca-Cu-O compounds

Michel *et al.* (1987) first discovered superconductivity between 7 K and 22 K in the Bi-Sr-Cu-O system. Because of the low T_c their report did not attract widespread interest. However, attention quickly focussed on the bismuth-containing superconductors when Maeda *et al.* (1988) independently discovered superconductivity in the Bi-Sr-Ca-Cu-O system above liquid nitrogen temperature. Three superconducting oxides were subsequently identified: $\text{Bi}_2\text{Sr}_2\text{CuO}_6$ ($T_c=7$ K to 22 K), $\text{Bi}_2\text{Sr}_2\text{CaCu}_2\text{O}_8$

($T_c \simeq 85$ K), and $\text{Bi}_2\text{Sr}_2\text{Ca}_2\text{Cu}_3\text{O}_{10}$ ($T_c \simeq 110$ K). For brevity, these phases will be referred to as **2201**, **2212**, and **2223**, respectively. The labels correspond to the relative compositions of the cations: bismuth, strontium, calcium, and copper. The structures consist of perovskite-like units containing one, two, or three CuO_2 planes sandwiched between BiO_2 bilayers. The ideal tetragonal symmetry of these crystal structures is complicated by staggered registry, a small degree of orthorhombicity in the a - b plane, and a modulation in the superstructure incommensurate with the primary subcells. As a result, the crystal structure of the Bi-Sr-Ca-Cu-O superconducting compounds is the most complicated of all the high T_c compounds. A detailed description of these structures will be given in Section 2.3.

1.2 Physical Properties

The main difficulty with high T_c superconducting oxides is that these materials are ceramics. They are brittle and cannot be readily formed into shapes that lend themselves to electrical or electronic applications. Single crystals are difficult to grow and polycrystalline samples exhibit weak links between grains and thus have poor performance. However, some successful applications have been achieved with thin film technology in the fabrication of superconducting quantum interference devices (SQUID's) that operate at 77 K.

Due to the highly planar nature of the crystal structures of these high T_c compounds, their transport properties are markedly anisotropic. The key to high critical currents (J_c 's) in polycrystalline samples is achieving good texturing in the final product. By aligning crystal grains in bulk samples so that their a-b planes are parallel, critical currents approaching those found in single crystals can be achieved.

1.3 Sample Preparation Techniques

The following section outlines the development of sample preparation techniques. The original solid state approach is briefly described, followed by the rapid solidification method used to prepare 100% dense amorphous precursors of the Bi-Sr-Ca-Cu-O superconducting compound. Next, a review of various methods reported for preparation of wire-like samples from Bi-Sr-Ca-Cu-O is given. Finally, the melt-extraction technique used in this work to fabricate amorphous Bi-Sr-Ca-Cu-O fibers is described in detail.

1.3.1 Solid State Method

The traditional method of preparing high temperature superconductor samples is by solid state reaction. Affectionately known as "shake 'n bake", the procedure involves repeated cycles of mixing oxide powders, pressing into pellets, and heat treating at

appropriate temperatures and atmospheres. This was the technique used by Bednorz and Müller, Wu *et al.*, Maeda *et al.*, and Hermann *et al.* to prepare their respective T_c record breaking materials. The major drawbacks of this method are that the samples are not very dense, suffer from chemical inhomogeneity, and do not have desirable shapes for applications.

1.3.2 Rapid Solidification

Partly to address these problems, rapid solidification techniques were developed. Amorphous materials have no long-range crystallographic order. The ability to make 100% dense amorphous precursors for Bi-Sr-Ca-Cu-O superconductors was the turning point in the development of high quality samples of this material. Bi-Sr-Ca-Cu-O samples prepared by powder processing suffer from low density (about 40%) and poor sintering. The high density and increased homogeneity of the amorphous precursors alleviate the problem of long-range diffusion during synthesis of crystalline superconducting samples. It was hoped that the rapid solidification route would lead to pure materials with enhanced bulk properties, such as higher critical currents (Hinks *et al.*, 1988).

A variety of rapid solidification techniques have been used to fabricate amorphous Bi-Sr-Ca-Cu-O precursors. *Splat quenching* of molten mixtures onto large heat sinks such as copper or stainless steel blocks is the simplest technique and has proven effective in producing high quality samples. Thin plates with diameters of several centimeters and thickness less than 0.3 mm can be produced in this fashion (Hinks *et al.*, 1988). The *twin roller* method was also employed successfully to produce samples 20–25 μm thick, 5–15 mm wide, and 20–50 mm long (Komatsu *et al.*, 1988b).

These rapidly quenched precursors have definite glass-like properties. X-ray diffraction patterns show broad amorphous peaks and differential thermal analysis (DTA) results indicate a glass transition around 680 K. This suggested the possibility of fabricating glass fibers or tapes from the Bi-Sr-Ca-Cu-O material and thus providing a solution to the applications problems inherent to high T_c oxides.

1.3.3 Fibers, Tapes, and Wires

A variety of methods have been used to prepare wire-like samples from Bi-Sr-Ca-Cu-O compounds, with varying success. The ultimate goal is the production of mechanically durable samples with critical current density $J_c \simeq 10^7 \text{ A}\cdot\text{cm}^{-2}$ at $T=77 \text{ K}$ and $B=10 \text{ T}$. The best results achieved to date have been with tapes produced by *cold rolling* Bi-Sr-Ca-Cu-O powder encased in a silver tube with subsequent heat treatment.³ Critical currents of $10^4 \text{ A}\cdot\text{cm}^{-2}$ at 77 K in zero field and $10^5 \text{ A}\cdot\text{cm}^{-2}$ at 4.2 K in fields above 25 T have been reported (Kumakura *et al.*, 1991).

Other methods reported in the literature for fabrication of wire-like samples from the Bi-Sr-Ca-Cu-O compound are *laser heated pedestal growth* (Qiao *et al.*, 1989), the *sol gel method* (Zhuang, Kozuka and Sakka, 1989), *melt spinning* (Gao *et al.*, 1989) from metallic alloys, *drawing of fibers* from glass preforms (Komatsu *et al.*, 1990), and *gas-jet fiberization* (Miller *et al.*, 1990). The latter three methods involve use of rapid solidification. Of these, *gas-jet fiberization* is most similar to the *melt-extraction* technique used in this work.

1.3.4 Melt Extraction Technique

Originally devised by Maringer and Mobley (1975), the *melt-extraction* technique has been developed by Rudkowski, Rudkowska, and Ström-Olsen to allow continuous casting of fine metallic fibers down to less than $5 \mu\text{m}$ in diameter. The details of this technique can be found elsewhere (Rudkowski, Rudkowska and Ström-Olsen, 1991).

In this work we adapted this procedure to produce amorphous fiber precursors for subsequent crystallization of the Bi-Sr-Ca-Cu-O high temperature superconductors. A full description is given in section 3.2.

³The rolling enhances texturing in the sample.

Chapter 2

Background: High T_c Superconductivity

The phenomenon of superconductivity has been widely studied and is well understood for conventional metallic superconductors. Detailed discussions on conventional superconductivity theory can be found in numerous texts, of which *Introduction to Superconductivity* by Tinkham (1975) is an excellent example. The following chapter is not intended to reproduce such volumes. Rather, a qualitative discussion of the phenomenology of superconductors is presented and a brief sketch of the theoretical background required to interpret the results obtained in this work is given. In addition, recent progress in high T_c theory will be discussed and the detailed description of Bi-Sr-Ca-Cu-O crystal structure promised earlier will be given. A discussion on starting compositions and heating treatments for the preparation of Bi-Sr-Ca-Cu-O samples completes the chapter.

2.1 Phenomenology and Theory

What Kamerlingh Onnes observed in 1911 was the complete disappearance of electrical resistivity in various metals such as mercury, lead and tin. This occurred in a small temperature range at a critical temperature T_c characteristic of the material. Thus, *perfect conductivity* was the first characteristic of superconductors to be discovered. The next was *perfect diamagnetism*, discovered by Meissner and Ochsenfeld (1933). Not only did they find that a magnetic field is excluded from a superconductor, but also that a field is expelled from an originally normal sample as it is cooled through T_c . This could not be explained by perfect conductivity, which would trap flux in. The existence of a reversible *Meissner effect* implies that superconductivity will be destroyed by a critical field H_c which is related thermodynamically to the free energy difference between normal and superconducting states.

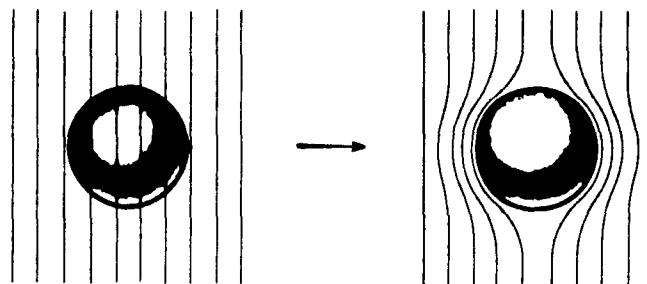


Figure 2.1: Meissner effect in a superconducting sphere cooled in a constant applied magnetic field; on passing below the transition temperature the magnetic field B is expelled from the sphere.

2.1.1 Meissner Effect

Below T_c , a superconductor behaves as if inside the specimen $B=0$ (see Figure 2.1). A simplified but useful result can be obtained if we limit ourselves to long thin specimens with long axis parallel to the applied field B_a . For ideal, 100% dense specimens in this special case (Kittel, 1986),

$$B = B_a + 4\pi M = 0 ; \quad \text{or} \quad \frac{M}{B_a} = -\frac{1}{4\pi} , \quad (2.1)$$

where B is the measured magnetic field and M is the magnetization of the sample (note that *CGS* units have been used). By measuring the magnetization of a superconducting sample in a magnetic field, one can determine the volume fraction of superconducting material within the sample, since 100% volume fraction would yield the result of Equation 2.1.

2.1.2 London Theory

At a temperature below T_c in zero field, a sample will be completely superconducting. As a magnetic field is applied, flux begins to penetrate the surface of the sample.

Surface eddy currents flow up to a characteristic penetration depth λ . This is known as the *intermediate state*. When the applied field reaches the critical value H_c , the magnetic flux penetrates the sample completely and superconductivity is destroyed. This is the behaviour of what are classified as *type I* superconductors and is described by the London equations (London and London, 1935):

$$\mathbf{J} = -\frac{c}{4\pi\lambda^2}\mathbf{A} \quad (2.2)$$

$$\nabla\mathbf{J} = -\frac{c}{4\pi\lambda^2}\mathbf{B}, \quad (2.3)$$

where \mathbf{J} is the current density and \mathbf{A} is the vector potential. For thick samples, the amount of sample into which the magnetic field has penetrated is negligible compared to the excluded portion and the flux can be thought of as having been completely expelled. When the sample thickness is of the same order as λ , the flux penetration becomes significant and a more careful analysis is required to determine the maximum flux exclusion possible.

2.1.3 BCS Theory

A microscopic theory of superconductivity was successfully formulated by Bardeen, Cooper, and Schrieffer (1957) and gave us our first detailed understanding of superconductivity. The key to BCS theory is the idea that even a weak attractive interaction, such as that caused in second order by the electron-phonon interaction, can result in the formation of bound pairs of electrons, known as *Cooper pairs*. These pairs comprise the superconducting charge carriers. Whether or not the electron-phonon interaction is responsible for superconductivity in the high T_c oxides is a topic of much debate.

2.1.4 Ginzburg-Landau Theory

Seven years prior to BCS, Ginzburg and Landau (1950), introduced a formalism that embodied the macroscopic quantum-mechanical nature of the superconducting

state and led to a better understanding of its unique electrodynamic properties. The Ginzburg-Landau theory introduces an important parameter κ which is the ratio of the penetration depth λ (see London Theory) to the coherence length ξ (characteristic of the distance over which electrons can interact to form bound pairs). For type I superconductors $\kappa \ll 1$. This is associated with a positive surface energy for a domain wall between normal and superconducting materials in the intermediate state.

2.1.5 Type II Superconductors

When κ is large instead of small, i.e., if $\xi < \lambda$, then we have a *negative* surface energy between normal and superconducting regions. This results in a subdivision of normal and superconducting domains within the body of the sample of size limited by the microscopic length ξ . Abrikosov showed (1957) that this occurs for $\kappa > 1/\sqrt{2}$ and called them *type II* superconductors to distinguish them from the earlier *type I* variety. For these materials, instead of a discontinuous breakdown of superconductivity in a first-order phase transition at H_c , there is a continuous increase in flux penetration starting at a first critical field H_{c1} (the so-called *mixed* or *vortex state*) and reaching total flux penetration at a second critical field H_{c2} (see figures 2.2 and 2.3). Because of the partial flux penetration, the diamagnetic energy of holding out the field is less, so H_{c2} can be much greater than the thermodynamic critical field H_c .

The new high T_c oxides are *type II* superconductors and thus hold much hope for applications in high-field superconducting solenoids above liquid nitrogen temperatures. However, in addition to difficulties in fabricating the requisite structures for such uses, limitations in critical currents resulting from poor sample quality pose a significant barrier to practical applications.

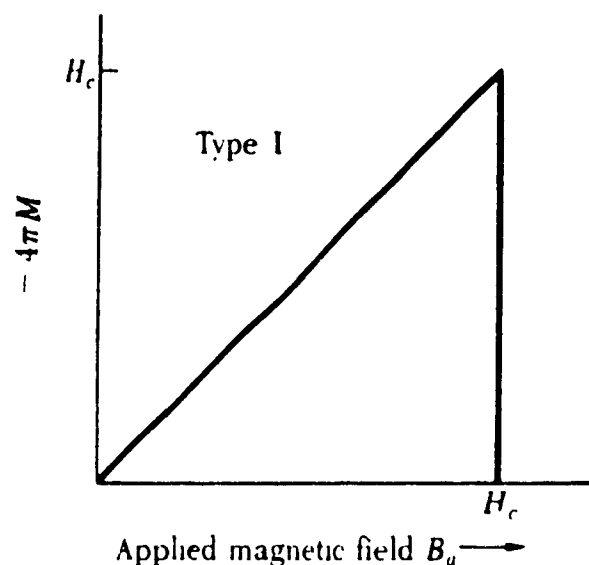


Figure 2.2: Magnetization versus applied magnetic field for a bulk *type I* superconductor exhibiting a complete Meissner effect. The sample is superconducting below H_c and normal above H_c . (Taken from Kittel (1986).)

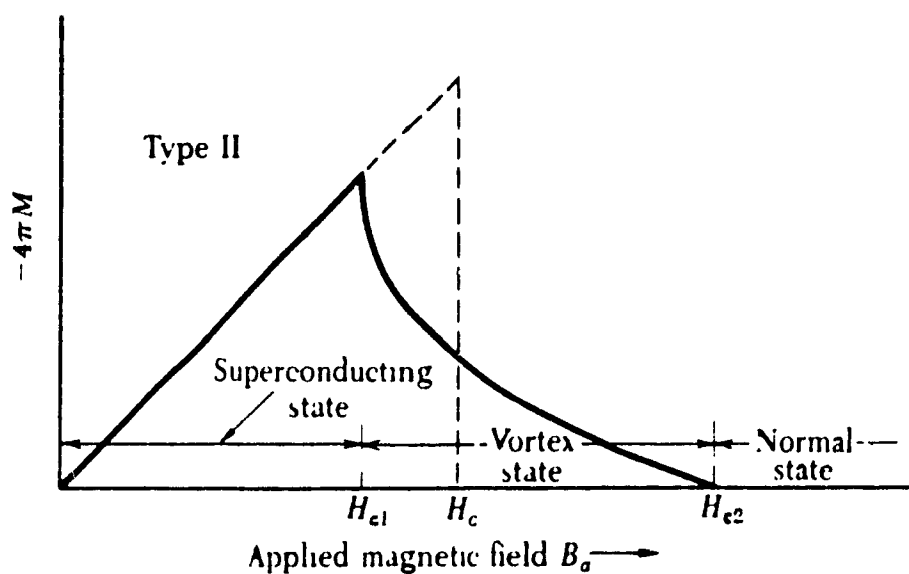


Figure 2.3: Superconducting magnetization curve for a bulk *type II* superconductor. Flux starts to penetrate at H_{c1} and the sample is in a *mixed* or *vortex state* until the applied field reaches H_{c2} . (Taken from Kittel (1986).)

2.2 Current High T_c Theories

The traditional theories of superconductivity (*e.g.* BCS, Ginzburg–Landau) benefited greatly from a thorough understanding of normal metals. Accordingly, the normal state of high T_c oxides should give insight into the superconducting state. Aside from their remarkably high transition temperatures, what sets high T_c superconductors apart from conventional superconductors are their anomalous normal state properties. Some noteworthy properties are the temperature dependence of the Hall coefficient (Ong, 1990), the linearity of the resistivity as a function of temperature (Gurvitch and Fiory, 1987), the nearly constant thermal conductivity (Steglich, 1988), and the unusual optical conductivity (Timusk and Tanner, 1990). These anomalous characteristics are the clues that point to the microscopic mechanism(s) responsible for superconductivity in high T_c oxides. It is generally accepted that the conventional BCS mechanism, namely *electron-phonon coupling*, must contribute. The small *isotope effect* in La-Ba-Cu-O (Batlogg *et al.*, 1987b) and Y-Ba-Cu-O (Batlogg *et al.*, 1987a) in addition to their anomalous normal state behaviour spurred theorists to come up with other mechanisms for superconductivity in these systems.

Proposed high T_c theories are becoming as numerous as the varieties of superconducting compounds discovered to date. After an initial period of confusion, the situation has calmed down considerably, and a serious and concerted effort is now being mounted to develop theories that make substantial contact with commonly agreed upon experimental facts. The precise nature of currently popular high T_c theories is beyond the scope of this volume (and its author). They can, in general, be divided into those that describe the superconducting and those that describe the normal state. Here are some of the more noteworthy ones:

Modified weak-coupling BCS theory and other BCS-like mechanisms have been pursued by many in an attempt to remain on familiar ground. Workers in this field believe that the high T_c oxides superconduct via the same intrinsic mechanism as conventional superconductors and that the theory requires only minor modifications

to fully describe their properties. Less conventional proposals for theories of superconductivity are the *spin bag* model put forth by Schrieffer *et al.* (1988; 1989) (which also makes some normal state predictions) and *Interlayer Josephson Pair Tunneling* proposed by Wheatly, Hsu and Anderson (1988).

Theories attempting to describe the normal state of high T_c superconductors are the *resonance valence bond* (RVB) model proposed by Anderson (1988), the *Hubbard* model and related *t-J* model (which have received much interest), and the *Marginal Fermi-liquid* model. The basic idea is that normal state properties cannot be arrived at from a Landau Fermi-liquid picture.

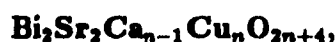
The difficulty now is that new proposed mechanisms do not predict enough differences in the superconducting properties of high T_c materials to distinguish one model from another. Any new mechanism must also microscopically explain all the strange normal state properties. It will be impossible to prove or disprove any new theories until they can describe both superconducting and normal state properties in sufficient detail.

2.3 The Bi-Sr-Ca-Cu-O Crystal Structure

Before understanding high T_c oxides it is necessary to characterize their crystal structures. Their highly two-dimensional nature and other structural qualities are key to the mechanism that makes superconductivity possible. Intimately related to these factors is the chemistry of high T_c systems. Comprehensive knowledge of the crystal structures permits a more accurate analysis of the charge distribution and determination of valences of atoms within the unit cell. Understanding the physical characteristics of high T_c oxide systems will give us insight into the mechanisms behind their electronic properties.

2.3.1 The Structural Series

The Bi-Sr-Ca-Cu-O family of superconductors has three members. The chemical formula of the structural series can be denoted as follows:



where n can equal 1, 2 or 3 and corresponds to the number of CuO_2 planes in the unit subcell. Table 2.1 summarizes the members of the family. The 2201 phase

n	compound	T_c	label
1	$\text{Bi}_2\text{Sr}_2\text{CuO}_6$	7-22 K	2201
2	$\text{Bi}_2\text{Sr}_2\text{CaCu}_2\text{O}_8$	85 K	2212
3	$\text{Bi}_2\text{Sr}_2\text{Ca}_2\text{Cu}_3\text{O}_{10}$	110 K	2223

Table 2.1: The Bi-Sr-Ca-Cu-O family of superconductors.

consists of alternating double BiO_2 and CuO layers separated by strontium layers. The 2212 phase can be generated from the 2201 phase by adding a calcium and

CuO layer. Another addition results in the 2223 phase. Figure 2.4 shows schematic diagrams of the Bi-Sr-Ca-Cu-O crystal structures. These compounds have the most complex structures of all the known high T_c compounds. The symmetry was at first thought to have been *tetragonal* but is now accepted as *orthorhombic* (with $a \simeq b$). Figure 2.4 actually shows only half of each unit cell. There is crystallographic shear perpendicular to the c -axis resulting in a *staggered registry*. In addition, electron diffraction studies reveal the existence of superstructures in the a - b plane that are incommensurate with the a - b lattice parameters. This long-range *incommensurate modulation* is due to a small displacement of bismuth atoms from their equilibrium positions. The existence of $n=4$ structures has been reported but it is not known if the corresponding compounds are superconducting.

The lattice parameters of the Bi-Sr-Ca-Cu-O compounds are tabulated in Table 2.2. An excellent review of the Bi-Sr-Ca-Cu-O crystal structure has been published

compound	space group	a (Å)	b (Å)	c (Å)
$\text{Bi}_2\text{Sr}_2\text{CuO}_6$	Amaa	5.362	5.374	24.62
$\text{Bi}_2\text{Sr}_2\text{CaCu}_2\text{O}_8$	Fmmm	5.414	5.418	30.89
$\text{Bi}_2\text{Sr}_2\text{Ca}_2\text{Cu}_3\text{O}_{10}$	I4/maa	3.814	3.814	37.00

Table 2.2: Lattice parameters of the Bi-Sr-Ca-Cu-O family.

by Matheis and Snyder (1990) and was used as a reference for much of the characterization performed in this work.¹ The JCPDS Powder Diffraction Files were also used to index the oxides and carbonates used in sample preparation and to identify crystalline phases in as-made and heat treated samples.

¹Also, Yvon and François (1989) have compiled a comprehensive review of the crystal structures of all the known high T_c oxides with an emphasis on the historical precedence of findings.

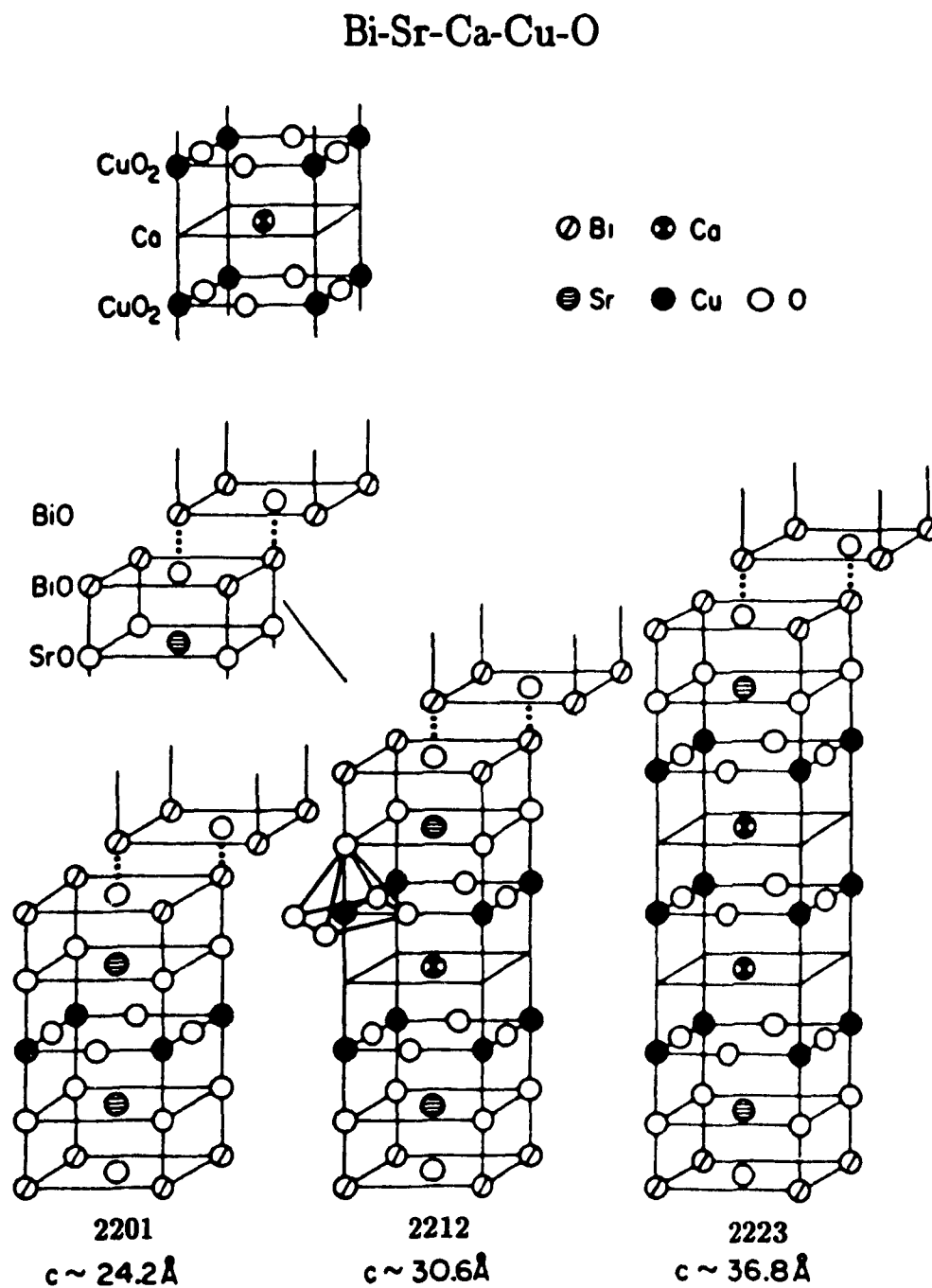


Figure 2.4: Crystal structures of the Bi-Sr-Ca-Cu-O oxides (taken from Xu *et al.* (1990)).

2.3.2 Chemical Disordering and Defects

Another factor complicating the Bi-Sr-Ca-Cu-O structures is chemical disordering of the cations within the unit cell. The stoichiometries and crystal structures given in Table 2.1 and Figure 2.4 are idealized. The actual superconducting compounds exhibit substitution of the calcium site by either strontium (Grader *et al.*, 1988) or bismuth (Sunshine *et al.*, 1988). The strontium site can also be occupied by calcium (Kajitani *et al.*, 1988). Defects such as stacking faults and twinning make it difficult to grow high quality single crystals of the Bi-Sr-Ca-Cu-O compounds. The higher T_c 2223 phase is particularly difficult to isolate and single-phase samples have not been produced to date. The precise chemical and structural properties of individual samples are highly dependent upon initial composition and sample preparation technique. All these anomalies contribute to making accurate characterization of these compounds very challenging.

2.4 Initial Compositions and Heat Treatment

Due to the complexity of Bi-Sr-Ca-Cu-O compounds, one cannot simply mix up the constituent oxide powders in the desired final stoichiometry and hope to get a single-phase sample. It is often found that all three Bi-Sr-Ca-Cu-O phases (2201, 2212, and 2223) and additional impurity phases are found in prepared samples. Some progress has been made in understanding the transformations due to heat treatment and in optimizing the initial compositions to attain the desired end products, mostly by heuristic methods. In this section we briefly describe some of the successful techniques used to obtain high quality samples and leave detailed discussion to subsequent chapters.

The 2201 phase is of little practical interest due to its low T_c . It is, however, important for understanding the formation of the higher T_c phases since it is the first superconducting phase to form when a mixture of constituent oxides is heated. The low formation temperature of 2201 (< 1000 K) is convenient for solid state synthesis since it ties up the bismuth atoms, preventing Bi_2O_3 from melting before the higher T_c phases can form.² The 2212 phase begins to form around 1070 K but optimal temperatures for maximum phase purity are closer to 1125 K. The 2223 phase forms from the 2212 phase after prolonged annealing at temperatures approaching the melting point of the material, which depend on the particular initial composition used (generally from 1125 K to 1145 K). The optimal furnace atmosphere for Bi-Sr-Ca-Cu-O materials has been determined to be air or a mixture of oxygen and an inert gas (Bhan, Khan and Rothaemel, 1989). A pure oxygen environment is not necessary because maximum oxygenation is not as crucial to the superconducting properties of Bi-Sr-Ca-Cu-O compounds as it is for other compounds such as Y-Ba-Cu-O.

By starting with a mixture of the appropriate metallic oxides³ such that the cation ratios are 2:2:1:2 for Bi, Sr, Ca and Cu, the result after proper heat treatment will

²The melting point of Bi_2O_3 is 1090 K.

³i.e. Bi_2O_3 , SrO , CaO , and CuO (or SrCO_3 and CaCO_3).

be a multiphase sample. Single-phase 2212 materials can be obtained with a nominal initial composition 4:3:3:4, where excess Bi_2O_3 and CuO act as a flux to aid in the formation of 2212 from 2201 (Tarascon *et al.*, 1988).

The 2223 ($T_c=110\text{K}$) phase has proven to be very difficult to isolate. Most work on producing high quality 2223 samples has involved use of rapid solidification techniques to form amorphous precursors. The higher density and better homogeneity possible with such methods (compared to solid state synthesis techniques) should allow better diffusion of cations through the matrix, and therefore, facilitate increased growth of the 2223 phase (as well as improving transport properties). Starting compositions rich in calcium and copper were reported to enhance growth of the 2223 phase (Shi *et al.*, 1989c; Shi *et al.*, 1989b). However, the single most effective technique for stabilizing the 2223 phase has been partial substitution of lead for bismuth (10–20%).⁴ The precise role of lead in the crystallization processes is unclear but it is suspected that lead enhances the diffusion of calcium and copper and thus affects the growth of the 2223 phase (Shi *et al.*, 1989a). It has also been proposed that the lead substitutes Bi^{3+} ions by Pb^{2+} ions resulting in a charge transfer between Bi_2O_3 and CuO_2 layers that creates additional holes and improves superconducting behaviour (Bansal *et al.*, 1991).

⁴First reported by Sunshine *et al.* (1988).

I

Chapter 3

Experimental Method

In this chapter, we describe the details of sample preparation, fiber production, heat treatment to transform the amorphous precursors into the superconducting compounds, and characterization techniques used to analyze samples during each phase of the experimental work.

3.1 Precursor Production

The oxide and carbonate powders used were obtained from Johnson Matthey Aesar Group (Toronto, Ontario). The compounds and their purities are listed in Table 3.1. The only strontium oxide powder available was of a technical grade and was determined (by X-ray diffraction) to have reacted to form a hydroxide. Thus, it was not suitable for preparing samples with accurate molar ratios and the more stable carbonate was used in its place. All starting powders were stored and weighed under argon atmosphere. Their phase purity was determined by X-ray diffraction and (apart from SrO) all powders were found to have negligible impurity levels. It has been reported that the use of starting powders with purity greater than three nines did not improve sample quality (Knauf *et al.*, 1991).

compound	purity
Bi_2O_3	99.9%
SrCO_3	99%
CaO	99.95%
CuO	99.9%
PbO	99.99%

Table 3.1: Powders used to prepare precursors pellets.

The solid state method was used to prepare precursor pellets for use in the *melt-extraction* procedure. The steps performed to produce the pellets are listed as follows:

1. The constituent oxide (and/or carbonate) powders are weighed to give the desired cation ratios.
2. The powders are mixed by ball milling in a Spex Industries Inc. Model 8000 Mixer (Edison, N.J.) for 10 to 15 minutes inside a hardened-steel vial with balls of varying size to form a uniform grey mixture. Isopropyl alcohol is used as a wetting agent (it is otherwise expected to be inert).
3. The mixed powder is dried and then cold pressed at $\simeq 20,000$ psi to form pellets (1 cm diameter, $\simeq 0.5$ cm thick).
4. The pellets are pre-reacted by heating at 1020 K overnight in air. This is to tie-up bismuth atoms by forming intermediate compounds (*e.g.* the 2201 phase), thus preventing Bi_2O_3 from melting when the samples are heated to higher temperatures (see Section 2.4). The colour of the sample is now greyish-black.
5. Steps 2 and 3 are repeated to ensure a homogeneous sample.

6. The pellets are sintered at 1125 K overnight in air to form the higher T_c compounds. After heating, 2212 is the majority phase, the remainder being made up of 2201, 2223, and various impurity phases. The colour of the sample is now a deep black.
7. Steps 2 and 3 are repeated once again and the pressed pellets are the final products used for fiber fabrication.

Precursor pellets were prepared with the following cation ratios. The order of the cations is Bi:Sr:Ca:Cu (no lead) and (Bi:Pb):Sr:Ca:Cu (with lead):¹

- 2:2:1:2, 2:2:2:3, 2:2:3:4, 2:2:4:5 (no lead).
- (1.8:0.2):2:2:3, (1.8:0.2):2:3:4, (1.6:0.4):2:2:3 (with lead).

Fibers were made from the different initial compositions and heat treated to investigate the effect of composition on final crystalline products.

3.2 Fiber Production

The *melt-extraction* technique used to fabricate Bi-Sr-Ca-Cu-O amorphous fiber precursors is discussed in detail in this section. Figure 3.1 gives a schematic diagram of the apparatus used. The steps performed to produce the fibers are as follows:

- The precursor pellet is placed on a boron nitride crucible and heated with a propane torch until uniformly melted (determined by visual inspection).
- The crucible is raised until it minimally contacts the edge of a rapidly rotating molybdenum wheel (wheel speed $\simeq 10\text{--}20$ m/s).
- Heat from the propane torch is continually applied to keep the sample in a molten state and the height of the crucible is constantly adjusted to maintain proper contact with the wheel.

¹Note that compositions written with colons (:) refer to initial compositions and those without (e.g. 2212 and 2223) refer to the superconducting compounds.

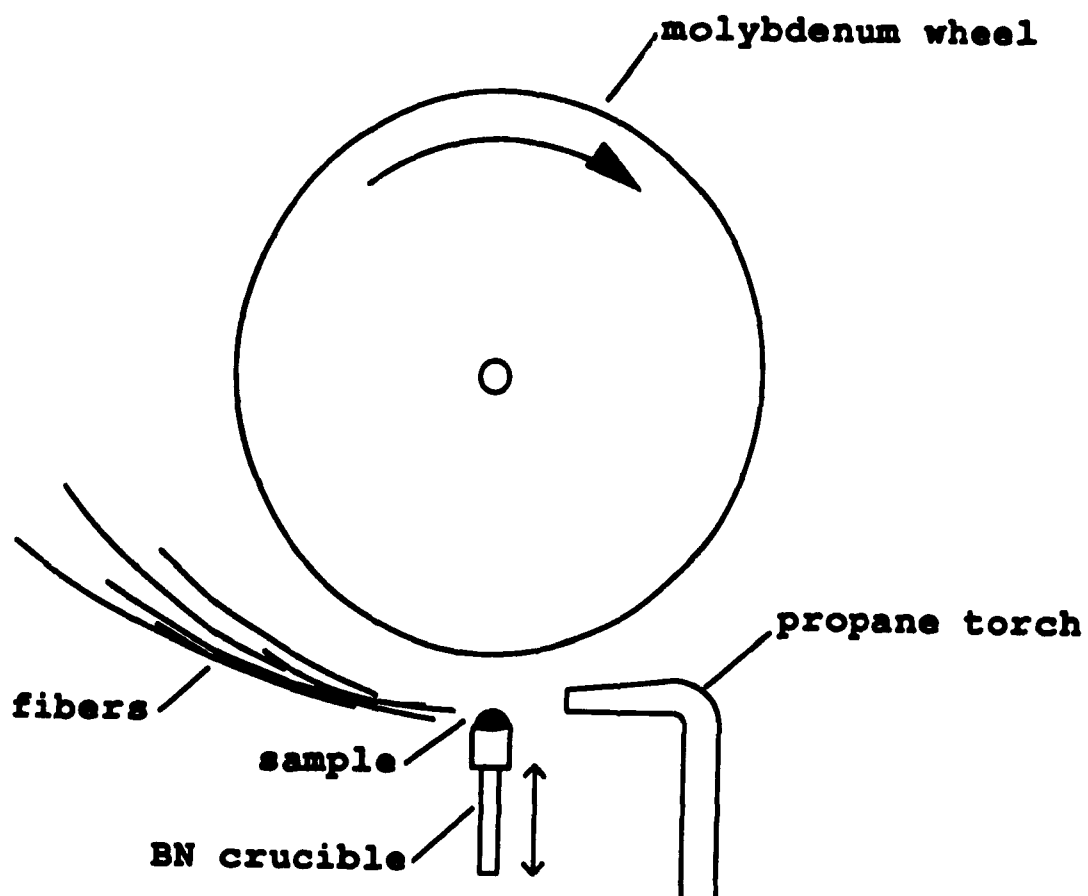


Figure 3.1: Schematic diagram of the melt-extraction fiber casting system.

- The process is continued until the sample is observed to have undergone a compositional change (3–5 minutes). This is determined to have occurred when the melt no longer exhibits a convex shape and loses its fluidity. Fiber production is stopped at this point by lowering the crucible away from the wheel.

The procedure is carried out in air. The wheel speed is limited by turbulence created by the spinning wheel inhibiting contact of the melt with the wheel edge. The cooling rate varies as the wheel speed making higher wheel speeds desirable for the production of high quality amorphous samples. The main constraint on turbulence is the low viscosity of the Bi-Sr-Ca-Cu-O melt ($\eta \simeq 1$ poise²)(Zheng, Hu and Mackenzie, 1991). Boron nitride is used for the crucible material because of its high melting point ($> 3000^\circ\text{C}$), low reactivity, and machinability.

Other methods of heating the sample that proved to be ineffective were:

- Use of a R.F. induction furnace to heat the precursor pellet. The samples had high enough conductivity at room temperature to be heated until they glowed a dull red but would not melt.
- Use of a graphite crucible heated with a R.F. induction furnace to indirectly heat the precursor pellet. Poor thermal contact between the graphite crucible and the pellet prevented quick and uniform melting of the sample.

Initial attempts at melting samples using these methods were done in an evacuated chamber partially backfilled with argon gas. A rapid loss of sample constituents due to evaporation was observed, resulting in a high rate of change in composition.

The reason for using the R.F. induction furnace is historical. It is the method used to heat samples for melt-extraction of metallic glass fibers, the process from which this technique was adapted. The propane torch proved an *ad hoc* solution to the heating problem. It provides relatively good control over the melting process and does not seem to introduce significant impurities into the fibers.

²c.f. $\eta_{\text{water}} \simeq 100$ poise at 20°C , 1 atm. (CRC, 1990).

The as-made fibers were characterized using differential scanning calorimetry (DSC), x-ray diffractometry (XRD), scanning electron microscopy (SEM), and transmission electron microscopy (TEM).

3.3 Heat Treatment

After fabrication, the amorphous Bi-Sr-Ca-Cu-O fibers were subject to heat treatment at temperatures ranging from 1125 K to 1145 K. The as-made samples were placed in alumina boats supported by an alumina crucible. The crucible was then loaded directly into a preheated furnace and the fibers annealed in ambient air atmosphere for periods ranging from 0.5 hours to 3 days. The horizontal single-zone tube furnace is resistively heated and has a maximum temperature of 1250 K. Temperature settings were maintained using a type-K thermocouple temperature controller reliable to within ± 5 K.

At the end of the heating period, the samples were immediately removed from the furnace to air quench the samples. This was in an attempt to preserve any phases that are stable only at higher temperatures, namely the 2223 phase, and has been reported to be effective in sharpening the observed normal-to-superconducting transition of Bi-Sr-Ca-Cu-O samples (Komatsu *et al.*, 1988a; Bansal *et al.*, 1991). The annealed fibers were then characterized by x-ray diffractometry (XRD), scanning electron microscopy (SEM), transmission electron microscopy (TEM), and SQUID magnetometry as described in the following sections.

3.4 Differential Scanning Calorimetry (DSC)

In isochronal experiments, the heat flow into and out of a sample was measured using a Perkin Elmer DSC-2c Differential Scanning Calorimeter (see Figure 3.2). The calorimeter has two holders which are heated resistively, one containing the sample and the other containing a reference. The two holders are programmed to be heated

or cooled at a specific rate and the difference in power required to keep the two holders at the same temperature is recorded as a function of temperature. This measurement is useful for characterizing the glass transition and crystallization of a sample.

The sample holders were preheated to a temperature of 330 K and samples scanned at a heating rate of 40 K/minute. Once the sample reached the desired final temperature (as high as 900 K) it was cooled at a rate of 320 K/minute back down to 330 K. The samples were heated under a flow of argon gas (99.998% pure) to help stabilize sample temperature, prevent oxidation of calorimeter parts at high temperature, and to remove any gases emitted by possibly volatile samples (to protect the DSC). No significant differences were observed when runs were performed in ambient air atmosphere.³ Sample masses were typically 5–10 mg and aluminum sample pans were used for all runs. Since the thermal processes of interest here are not reversible, they can be more clearly resolved by subtracting from the data a background run performed on an empty sample pan.⁴

Both the endothermic glass transition and exotherms resulting from the latent heat of crystallization are observed. Information acquired from DSC work were combined with x-ray diffraction results to investigate the nature of samples at various stages of the crystallization process as identified from the *heat flow vs. temperature* curves. Also, samples were held isothermally after scanning to various final temperatures and x-ray diffraction measurements performed on the samples to investigate the effect of annealing on crystal growth.

³Heating in an inert atmosphere is known to lower the melting point of Bi-Sr-Ca-Cu-O compounds and influence crystallisation kinetics at higher temperatures, but has little effect at the temperature ranges used in DSC analysis (Nassau *et al.*, 1989; Bhan, Khan and Rothaemel, 1989).

⁴It is preferable to rescan the sample and subtract the second run from the original scan. However, the Perkin Elmer DSC-2c does not permit calculations to be performed on such subtracted scans.

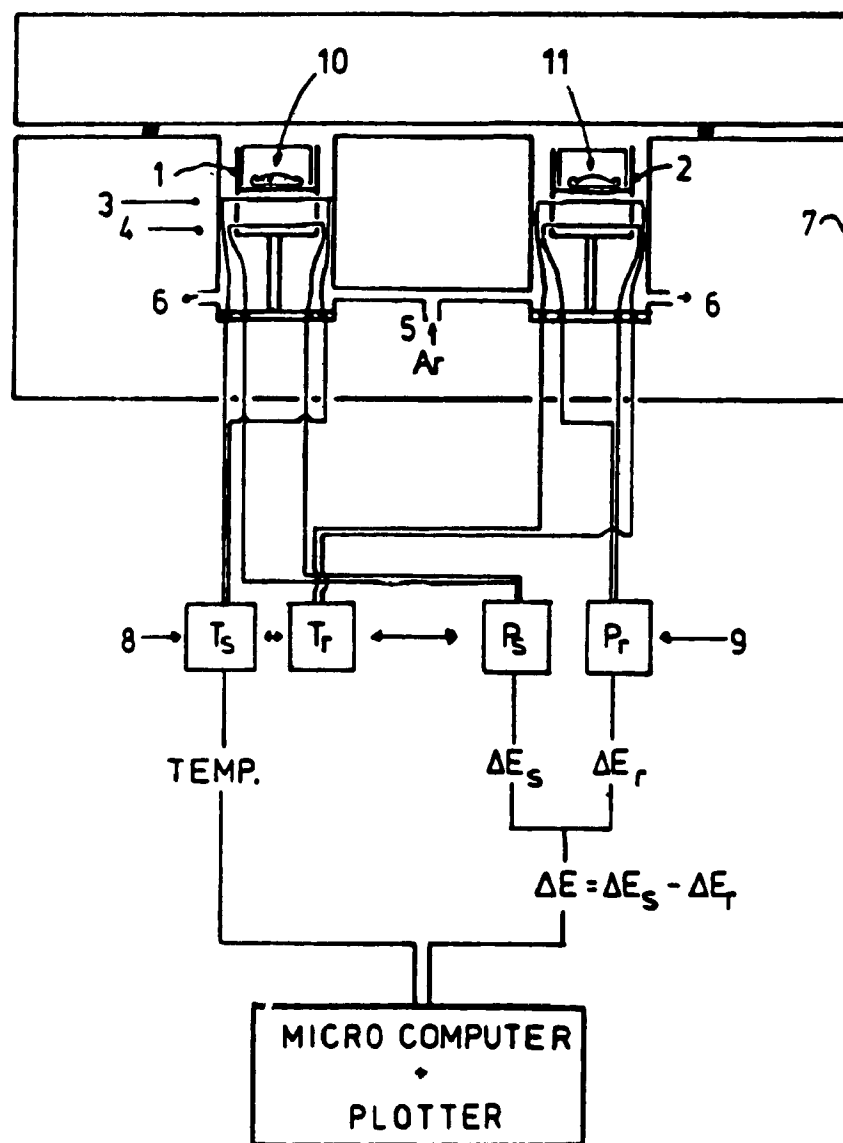


Figure 3.2: Schematic diagram of the Perkin Elmer DSC-2c Differential Scanning Calorimeter (taken from Richter (1988)).

- | | |
|----------------------------|---|
| 1 - sample holder | 7 - aluminum body (heat sink) |
| 2 - reference holder | 8 - thermometers for sample and reference |
| 3 - resistance thermometer | 9 - power supplies for heaters |
| 4 - heater | 10 - sample confined in aluminium pan |
| 5 - argon inlet | 11 - reference sample |
| 6 - argon outlet | |

3.5 X-Ray Diffractometry (XRD)

The X-ray diffraction measurements of as-made and heat treated fibers and precursor pellets were performed using an automated Nicolet-Stoe L11 Powder Diffractometer equipped with a copper target (see Figure 3.3). A graphite monochromator was used to select CuK_α radiation with a weighted average wavelength of 1.54178 Å. The diffraction geometry used was the conventional reflection mode. Fibers and precursor pellets were powdered using an alumina mortar and pestle and mounted on glass microscope slides with 3M double-sided tape. Starting powders were applied directly to the tape without special preparation.

The data collection system stored 2θ and the measured intensity, where θ is the Bragg angle. Measurements were taken over a range $2\theta = 4^\circ\text{--}60^\circ$. Recorded 2θ values for amorphous peaks were converted to nearest-neighbor distances using the Ehrenfest relation,

$$R_{\text{nearest-neighbour}} = \frac{\lambda}{\sin \theta \cdot 1.627}, \quad (3.1)$$

where λ is the wavelength of the x-ray radiation and the value 1.627 is the Ehrenfest constant. 2θ values for crystalline peaks were converted to d-spacings using the standard Bragg relation

$$2d \cdot \sin \theta = n\lambda \quad (3.2)$$

and compared with values published in the literature to identify the phases present.

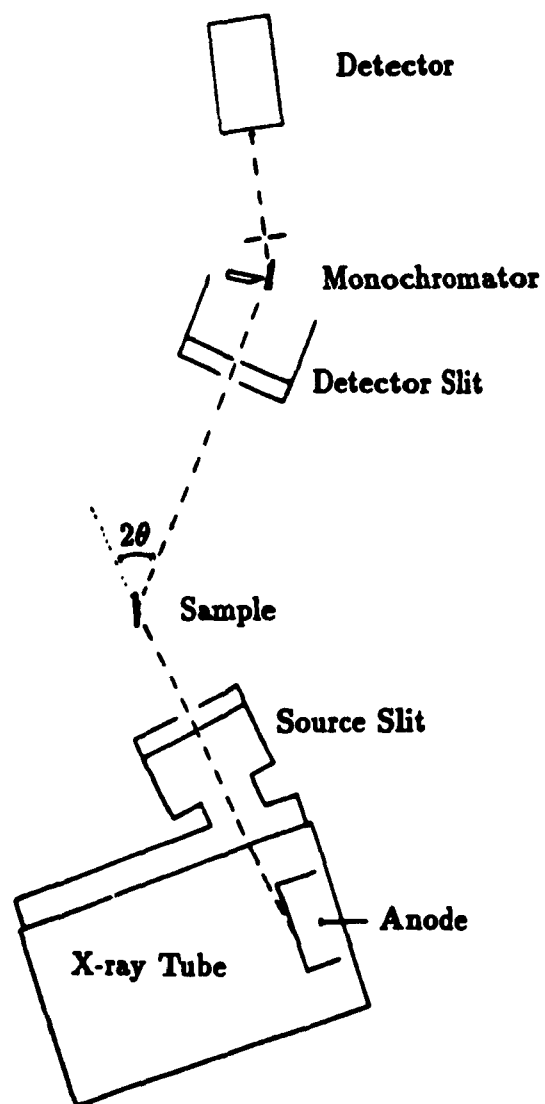


Figure 3.3: Schematic diagram of the Nicolet-Stoe L11 Powder Diffractometer (taken from Marshall (1986)).

3.6 Scanning Electron Microscopy (SEM)

The surface morphology and composition of as-made and annealed fibers were investigated using a JEOL T300 and a JSM 840A scanning electron microscope. Both microscopes were operated with an accelerating voltage of 20 keV. Energy Dispersive X-ray spectroscopy (EDX) was performed and sample composition was determined using a Tracor Northern Series II X-ray Microanalysis System. Samples were prepared by mounting onto aluminum sample holders with 3M double-sided tape and depositing a thin film of gold-palladium alloy.

3.7 Transmission Electron Microscopy (TEM)

Transmission electron microscopy analysis was performed using a Phillips CM20 Transmission Electron Microscope with an accelerating voltage of 200 keV. Observations were made in the standard bright field transmission mode and in the diffraction mode. Lattice fringes were viewed using the High Resolution capabilities of the microscope. Sample composition was determined with an EDAX 9900 Energy Dispersive X-Ray spectrometer (EDX).

Samples were prepared by the *crushing method* using an alumina mortar and pestle. This method produces fragments of random sizes and shapes and thus thin samples with a particular lattice orientation are difficult to find. Ion beam milling is a more controlled method for thinning samples for TEM analysis but attempts at milling thin fibers were unsuccessful. The crushed samples were mounted by evenly distributing them onto nylon, copper, and nickel grids coated with a thin carbon film.

3.8 SQuID Magnetometry

SQuID (Superconducting Quantum Interference Device) magnetometer samples were prepared by sandwiching them between two pieces of sticky capton and placing the capton inside a gelatin capsule. The sample mass was approximately 1 mg. Individual

fibers were mounted such that they were longitudinally aligned with the applied field.

Magnetic measurements were made using a Quantum Design SQUID Magnetometer, model MPMS. Susceptibility measurements were performed by first cooling the sample to 5 K in zero field, applying a field of 50 Gauss, and then measuring the magnetic moment as the sample was gradually warmed above the critical temperature (*zero field cooled* or ZFC curve). The applied field was maintained and the magnetic moment measured as the sample was cooled again down to 5 K (*field cooled* or FC curve).

3.9 Resistance Measurements

Attempts were made to determine the resistivity of annealed fibers. The main obstacles barring successful measurements were the fragility of the fibers and the inability to make good electrical contacts. The first method tried was encasing a bundle of annealed fibers in indium/tin solder. The alloy was chosen for its low melting point so as not to damage the crystalline phases present in the fibers. Electrical contacts were poor due to insufficient wetting of the fibers with the solder. Thus, no superconducting transition in resistivity was seen cooling the solder-encased fibers below 77 K.

The second method used was one reported to have been successful with fibers drawn from a glass preform (Komatsu *et al.*, 1990). As-made fibers were coated with silver paste before annealing.⁵ After annealing they were mounted onto a glass slide with vacuum grease and leads were attached with more silver paste. The sample was placed in a cryostat and cooled down to 4.2 K. The resistance measured using an AC bridge with a current density of approximately 0.1 A/cm². A plot of resistance as a function of temperature for coated (1.8:0.2):2:3:4 fibers annealed at 1135 K for 7 hours showed only a metallic response and no superconducting transition (see Figure 3.4).

⁵Applying the silver paste to annealed fibers might impair their superconducting properties due to penetration of the fibers by the organic solvent in the paste.

It is suspected that the resistivity of the silver paste *only* was measured and that contact problems between the silver paste and fiber were the cause.

Final attempts at resistivity measurements consisted of mounting as-made fibers onto alumina slides by gluing the ends down with silver paste. Annealing of the silver paste is reported to produce low resistance contacts (Khare *et al.*, 1989). By not coating the body of the fiber, it was hoped that the current would be forced to pass through it and any superconducting transition would be detected by resistance measurements. Unfortunately, no samples prepared in this manner survived the annealing process intact.

A method of making multifilamentary composites from fibers by gas-jet fiberization has been reported (Miller *et al.*, 1991). The procedure involves evaporating silver onto as-made fibers, shaping them into a yarn, and inserting them into a silver tube. The composite is then cold isostatically pressed and annealed. This technique might successfully be applied using fibers made by the melt extraction method described in this work.

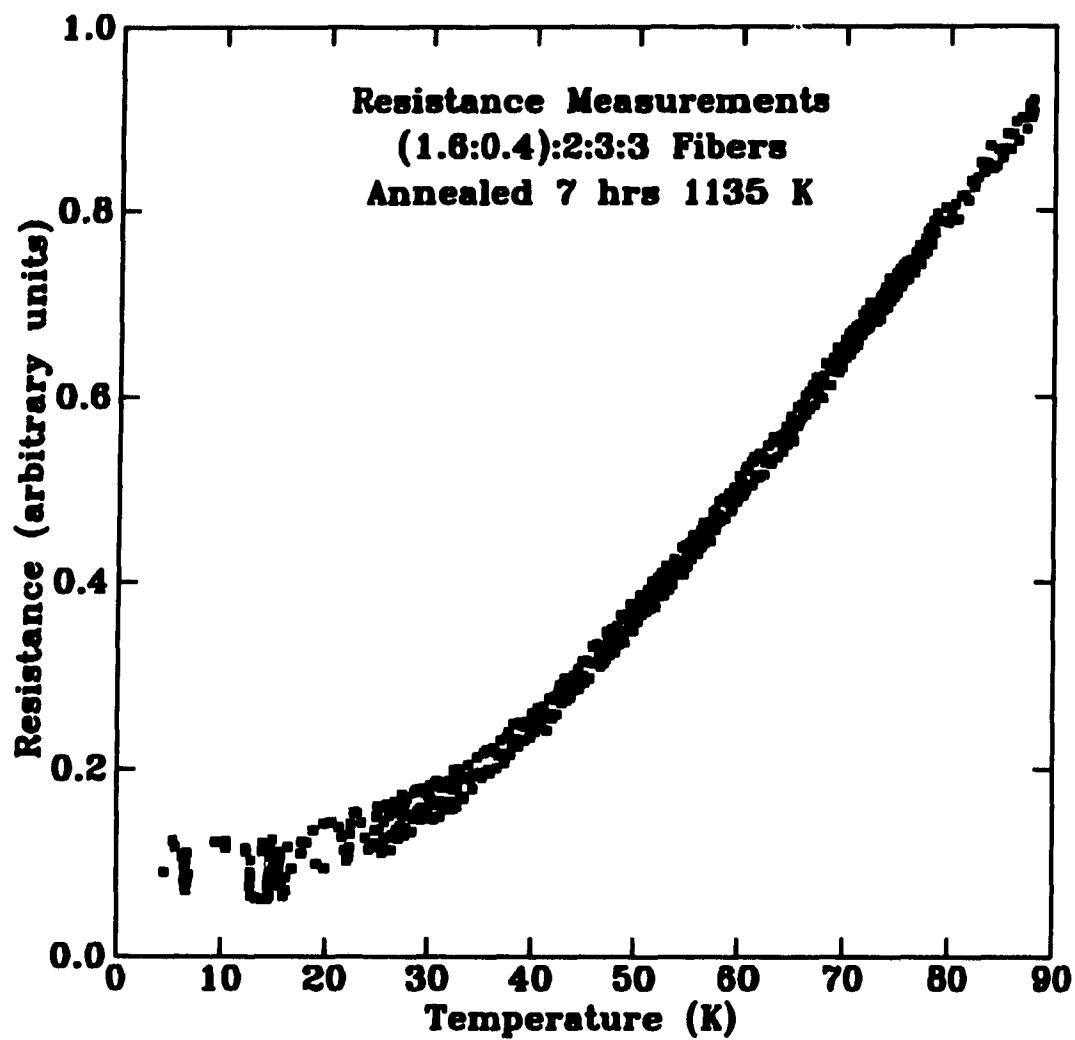


Figure 3.4: Plot of resistance vs. temperature for (1.8:0.2):2:3:4 fibers coated with silver and paste and annealed at 1135 K for 7 hours. No superconducting transition is visible.

Chapter 4

Results and Discussion

In this chapter, the results of characterization studies performed on as-made and heat treated fibers are presented. The crystallization of precursor and superconducting phases was studied using the techniques described in Chapter 3. The effect of addition of calcium and copper to nominal compositions and the substitution of lead for bismuth was investigated with particular attention paid to the formation of the 2223 phase. The change in microstructure with annealing time was also examined in order to gain a qualitative understanding of the evolution of the grain structure within heat treated fibers. Finally, the superconducting properties of heat treated fibers were investigated by squid magnetometry.

4.1 As-Made Amorphous Fibers

Thin, amorphous fibers were fabricated using the melt-extraction technique described in Section 3.2. Fiber dimensions ranged from $0.7\mu\text{m}$ to $100\mu\text{m}$ in diameter and 0.2 cm to 5 cm in length. Median dimensions were approximately $30\mu\text{m}$ in diameter and 1.5 cm in length. Figure 4.1 shows a sampling of the different shapes and sizes of fibers produced. Higher wheel speeds tended to produce finer and smoother fibers, although fibers of various sizes were produced in a given run. Figure 4.2 shows an enlargement of the thinnest fiber visible in Figure 4.1. The bulbous features exhibited by some of the fibers (see Figure 4.3) are thought to be disturbances caused by Rayleigh breakup that were frozen-in during solidification (Brodkey, 1967, for details). This is reasonable since the melt pulled off by the wheel would behave effectively as a liquid jet until it solidified. Thinner fibers would have solidified more quickly and had less time to break up. The ratio of bulb size to fiber diameter is approximately 2:1 and is in agreement with the theoretical value for idealized jet breakup (Brodkey, 1967).

The fibers were brittle but could be easily handled with fine tweezers. In addition to fibers, shot and flakes of various sizes may be produced. The net yield of fibers was approximately 2%, a value comparable to that achieved with gas-jet fiberization (LeBeau *et al.*, 1989). The calcium and copper-rich initial compounds were difficult to melt uniformly, making fiber production problematic. Thus, fibers from the 2:2:3:4 and 2:2:4:5 initial compositions could only be made in limited quantities.

4.1.1 X-Ray Diffraction Analysis

X-ray diffraction patterns from powdered as-made fibers show broad peaks indicative of an amorphous structure. A typical diffraction pattern is shown in Figure 4.4. The large peak at $2\theta \simeq 30^\circ$ is a common feature to all rapid solidification work on Bi-Sr-Ca-Cu-O (Minami *et al.*, 1988, for example). The Ehrenfest relation (see Equation 3.1 gives a d-spacing of approximately $3.7 \pm 0.2 \text{ \AA}$ which is consistent with inter-

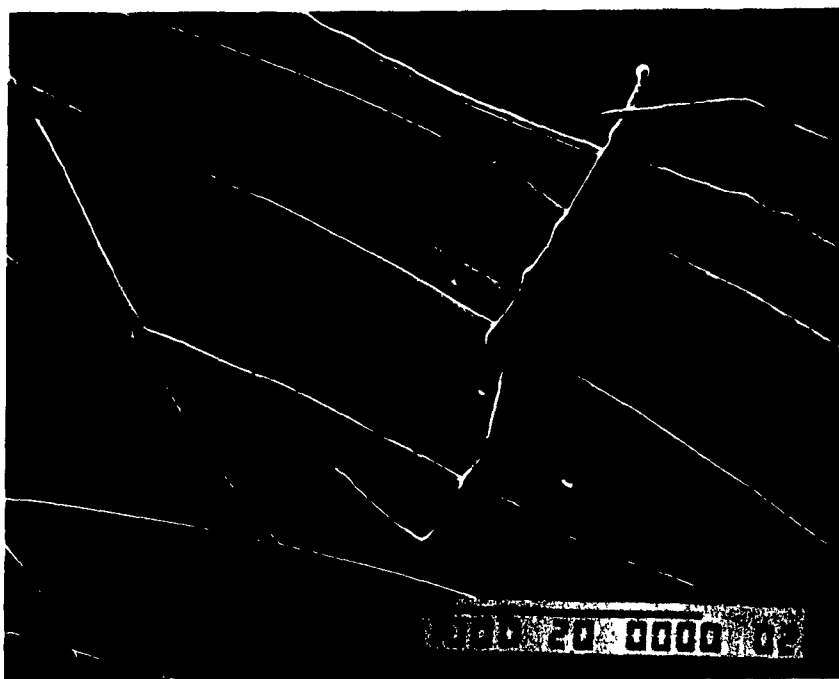


Figure 4.1: SEM micrograph of an average sampling of fibers. The scale marker is 1000 μm long. The boxed region is shown enlarged in Figure 4.2.

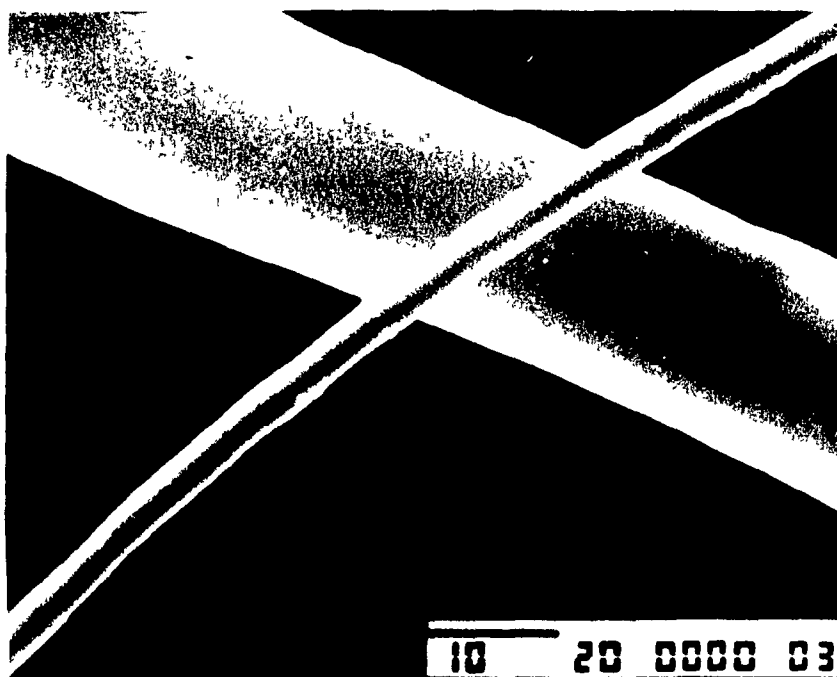


Figure 4.2: Enlargement of the thin fiber visible in Figure 4.1. The scale marker is 10 μm long. The thinner fiber is 3 μm in diameter.



Figure 4.3: SEM micrograph of fiber exhibiting bulbous features. The scale marker is $100\text{ }\mu\text{m}$ long. The ratio of bulb diameter to fiber diameter is approximately 2::1.

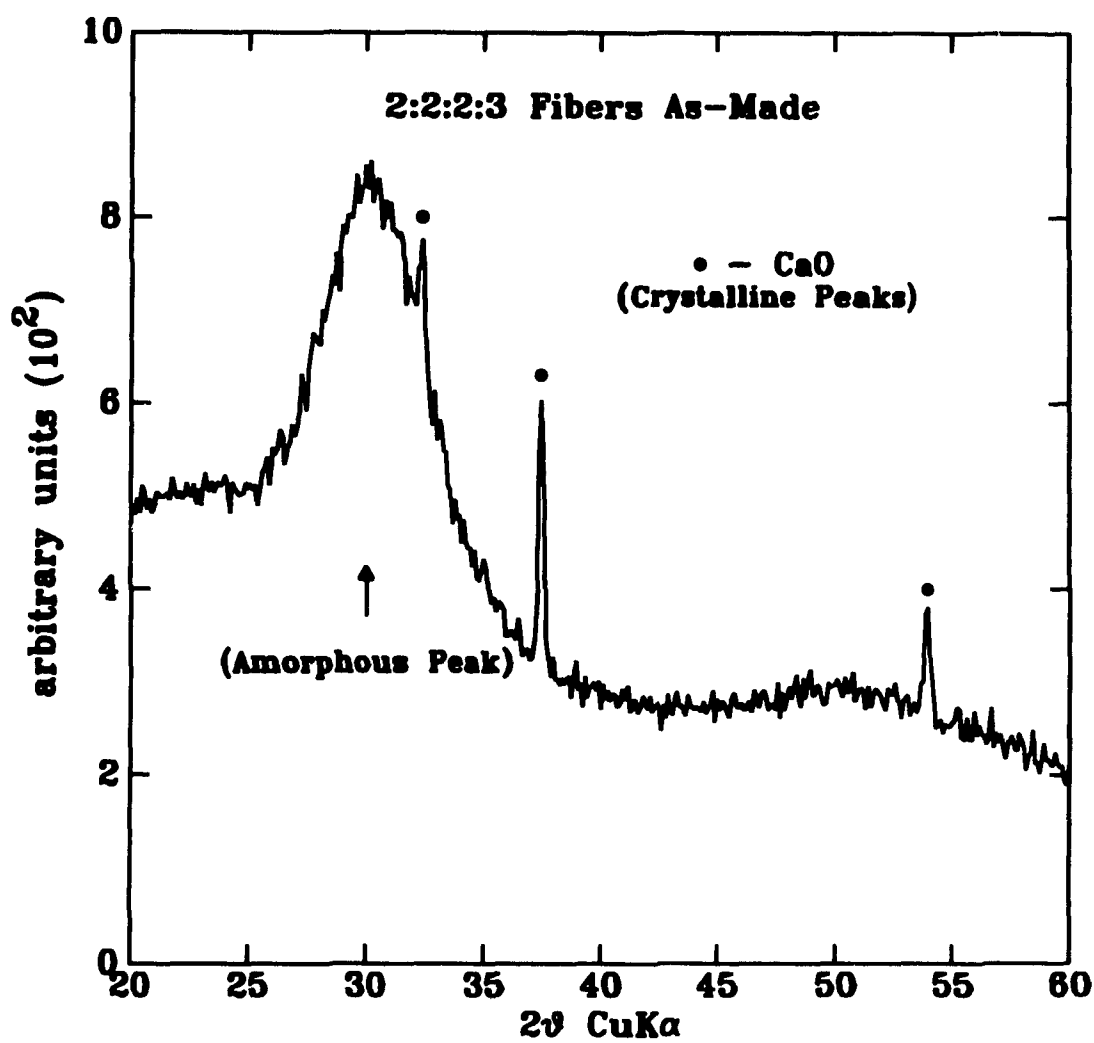


Figure 4.4: X-ray diffraction pattern of 2:2:2:3 as-made fibers. The broad peaks are indicative of an amorphous structure and the sharp crystalline peaks are indexed as CaO precipitates.

atomic distances for both Bi-Ca (3.67 Å) and Bi-Sr (3.85 Å).¹ One might expect to see a large peak corresponding to the Bi-Bi interatomic distance (3.40 Å) since the heavier Bi atoms scatter x-rays more effectively than the other lighter elements in the system. However the structure of the quinary Bi-Sr-Ca-Cu-O amorphous system is highly complex and the reasons behind the domination of the structure factor by the Bi-Ca and Bi-Sr contributions could be many. There are no detailed studies of the amorphous phase of the Bi-Sr-Ca-Cu-O compound to the knowledge of the author.

Crystalline peaks indexed as CaO were also observed, (see Figure 4.4. The volume fraction of amorphous material in the fibers is estimated to be 80% ($\pm 10\%$) by comparison of the integrated peak intensities for amorphous and crystalline peaks (weighted appropriately for atomic number). The 2:2:2:3 composition is on the edge of the glass forming region for Bi-Sr-Ca-Cu-O (Zheng, Xu and Mackenzie, 1989). Figure 4.5 shows a phase diagram indicating the glass forming region of the $\text{BiO}_{1.5}\text{-Ca}_{0.5}\text{Sr}_{0.5}\text{-CuO}$ system. The amount of calcium in the initial composition exceeds the solubility limit of calcium in the Bi-Sr-Ca-Cu-O glass so that CaO precipitates on solidification.

4.1.2 SEM and TEM Studies

Scanning electron microscopy of the as-made fibers shows that some of the fibers exhibit dark spots (see Figure 4.6) and rough regions (see Figure 4.7). EDX microanalysis performed on these areas revealed that the dark spots are calcium-rich and the rough regions are copper-rich (see Table 4.1). The rough regions generally appear on the free side of the fiber, suggesting that copper precipitates come out of solution due to phase separation of the glass. The absence of Cu or copper oxide lines in the XRD patterns for as-made fibers (see Section 4.1.1 indicates that these copper-rich regions are amorphous or, if crystalline, consist of grains too small in size (< 50 Å) and/or few in quantity ($< 5\%$) to be detected by our diffractometer. This is in con-

¹Based on the metallic radii (coordination number 12) for these elements

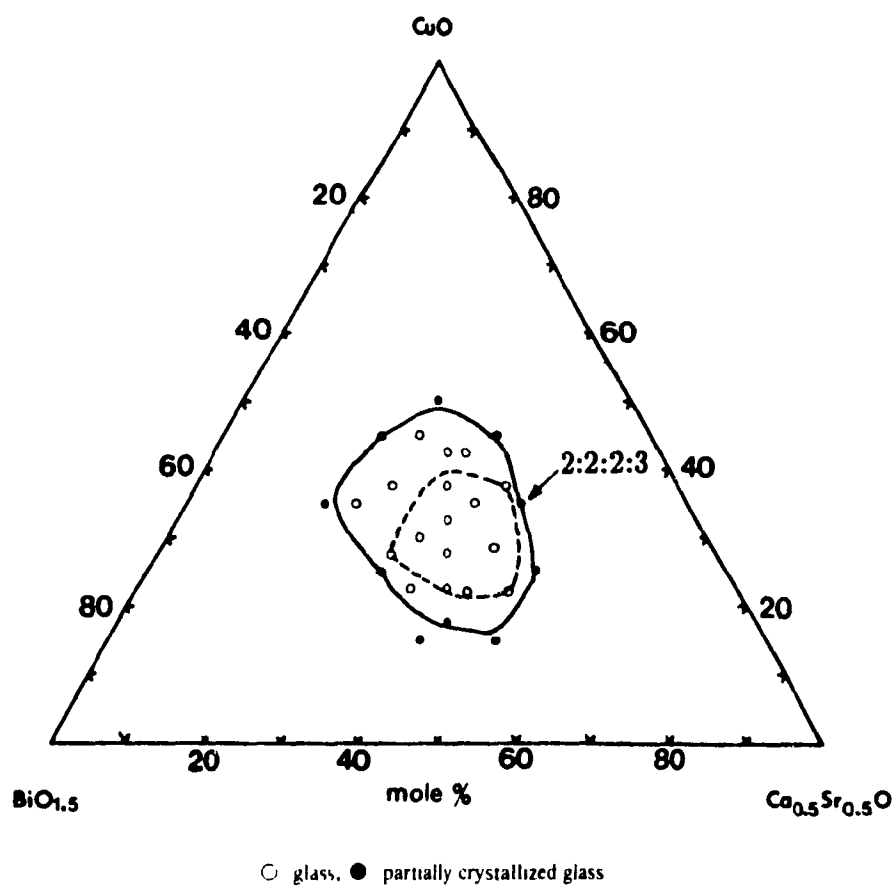


Figure 4.5: Phase diagram showing the glass forming region of the $\text{BiO}_{1.5}$ - $\text{Ca}_{0.5}\text{Sr}_{0.5}\text{O}$ - CuO system (taken from Zheng, Xu and Mackenzie (1989)).

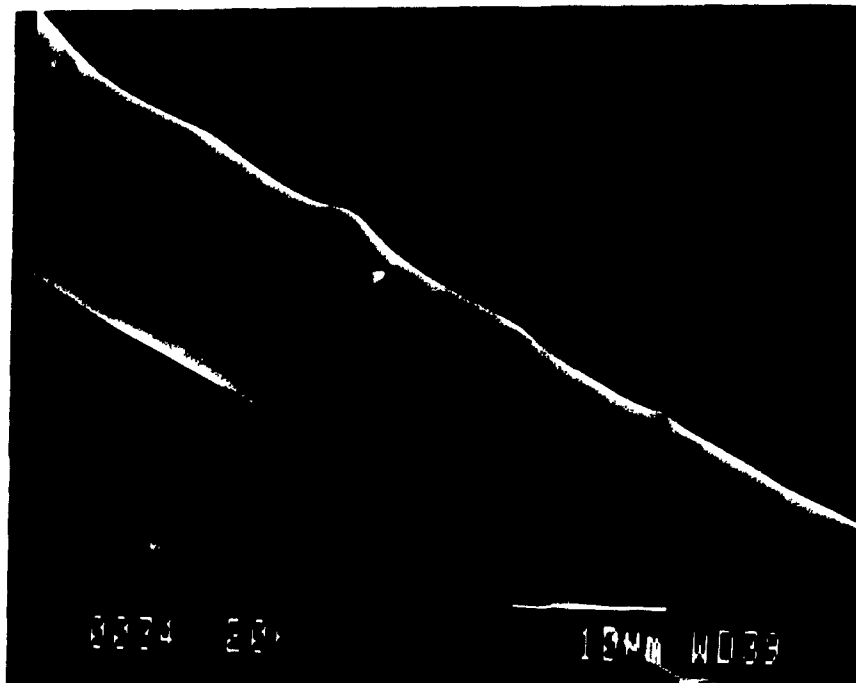


Figure 4.6: SEM micrograph of as-made fiber with dark spots. The scale marker is 10 μm long.

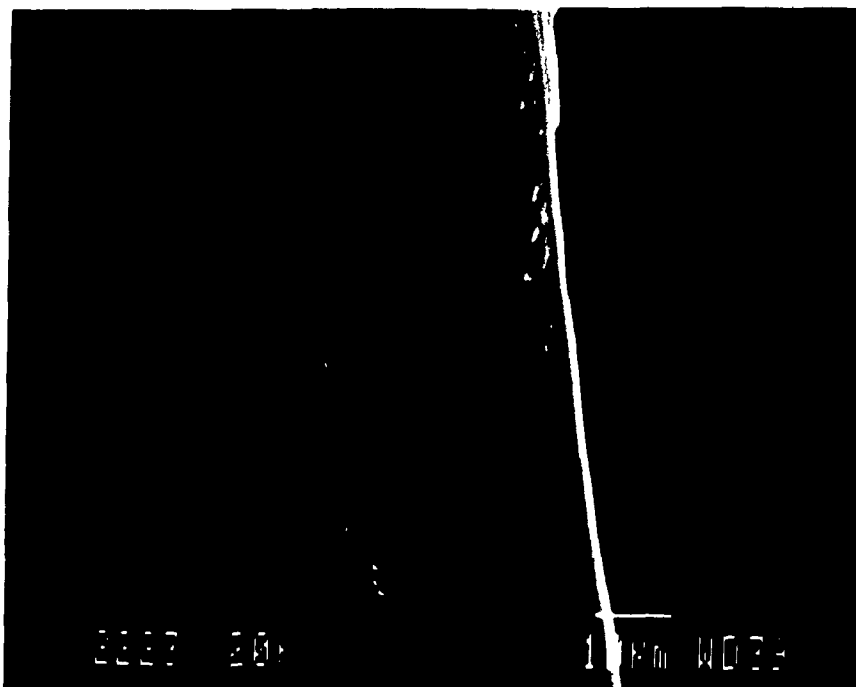


Figure 4.7: SEM micrograph of as-made fiber with rough regions. The scale marker is 10 μm long. The right edge of the fiber was in contact with the wheel. Notice how the rough features form preferentially on the free side of the fiber.

element	atomic percent (%)				
	SEM ($\pm 20\%$)			TEM ($\pm 10\%$)	
	dark	rough	smooth	crystalline	amorphous
Bi	14	7	35	5	28
Sr	3	21	17	6	29
Ca	70	11	14	83	15
Cu	13	61	34	6	28

Table 4.1: SEM EDX microanalysis of as-made 2:2:2:3 fibers.

trast to the crystalline CaO precipitates found in the as-made fibers. Typical EDX spectra of the dark, rough, and smooth regions are shown in Figures 4.8, 4.10, and 4.9. The SEM analysis of the smooth regions was averaged over many fibers with a typical standard deviation of a few percent. Data for the dark spots and rough regions are for scans of individual locations as shown in Figures 4.6 and 4.7.

TEM EDX microanalysis was also performed on the as-made 2:2:2:3 fibers. Amorphous and crystalline fragments were identified with selected area diffraction and the results of compositional analysis are given in Table 4.1. Representative spectra are shown in Figures 4.11 and 4.12. The high calcium content of the crystalline fragments is consistent with the XRD results of Section 4.1.1.

Lead was detected in amounts consistent with initial compositions for fibers made from lead-substituted initial compositions (*e.g.* $\approx 1\%$ for (1.8:0.2):2:2:3). However, it was excluded from the compositional analysis since these amounts were much smaller than the estimated uncertainties for these results ($\pm 20\%$ for SEM, $\pm 10\%$ for TEM).

It should be noted that compositions as determined by EDX from both SEM and TEM are only semi-quantitative due to a lack of reliable reference standards, even though care was taken to choose x-ray lines close in energy for the microanalysis calculations (so that bulk absorption corrections were applied uniformly). SEM EDX results are further hindered by the inability to meet the requirement that samples

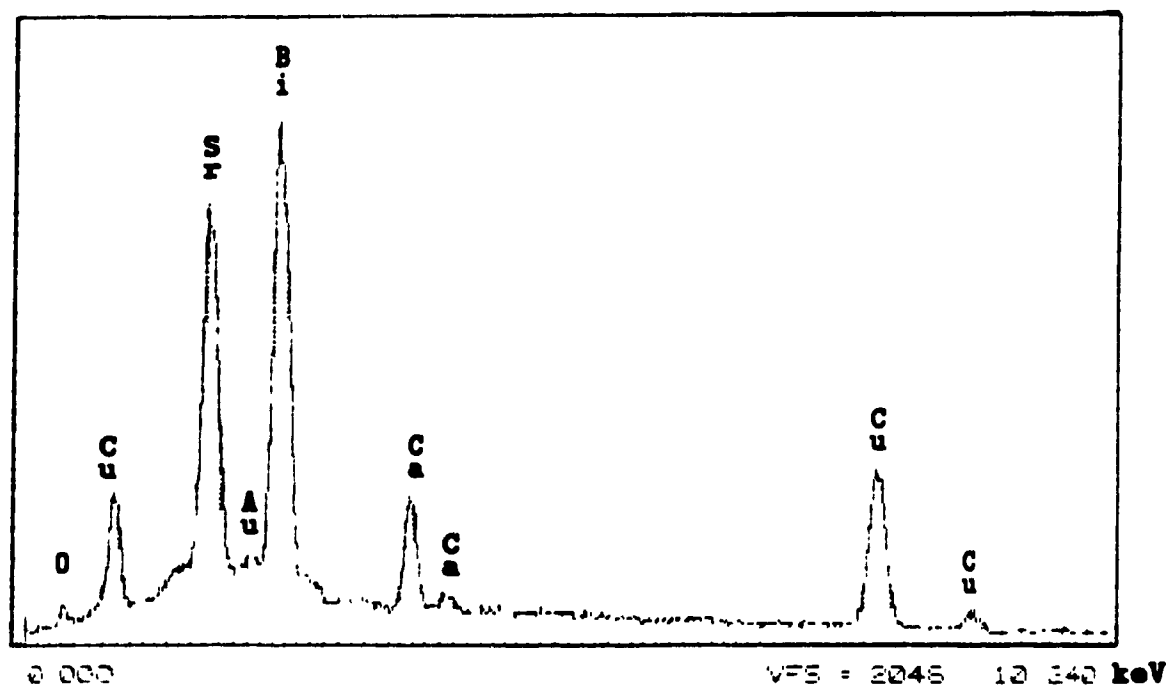


Figure 4.8: SEM EDX spectra of smooth region on as-made 2:2:2:3 fibers. (The Au peak to the right of the Sr peak is due to the gold coating used to prepare the samples.)

have flat surfaces (thus, the higher estimated uncertainty). However, the measurements indicate the relative differences in atomic concentrations between samples or between regions within a sample. Furthermore, the consistency of results from TEM EDX microanalysis on annealed fiber samples with expected values (see Section 4.3.4) suggests that the TEM results accurately reflect absolute compositions.

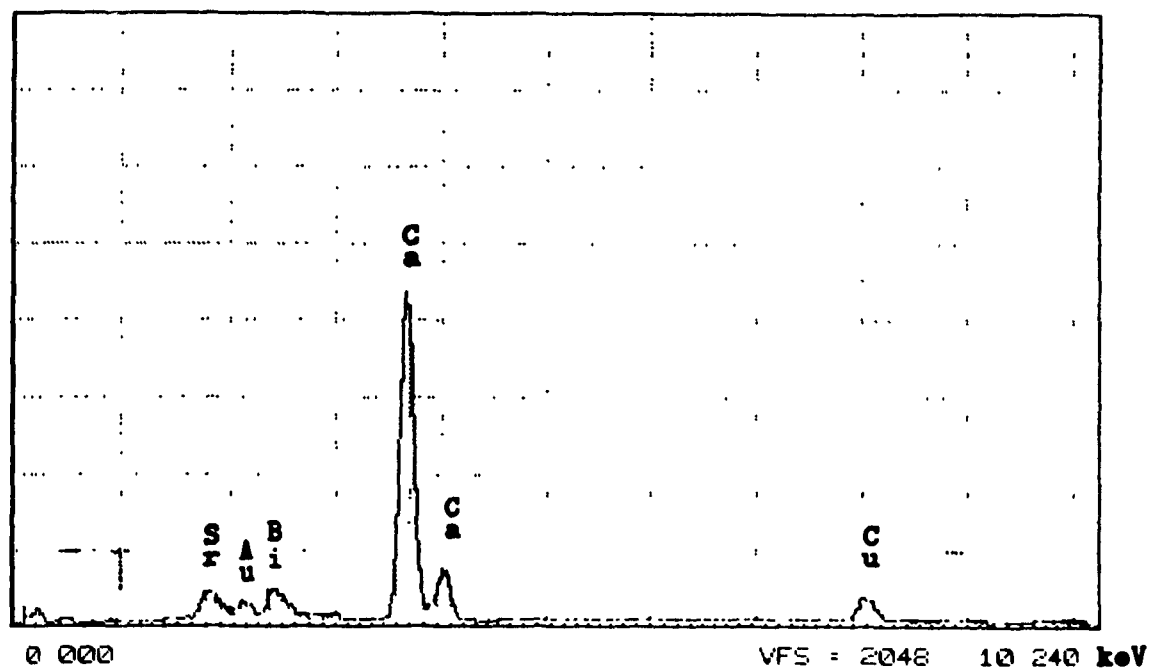


Figure 4.9: SEM EDX spectra of dark spot on as-made 2:2:2:3 fibers. (The Au peak to the right of the Sr peak is due to the gold coating used to prepare the samples.)

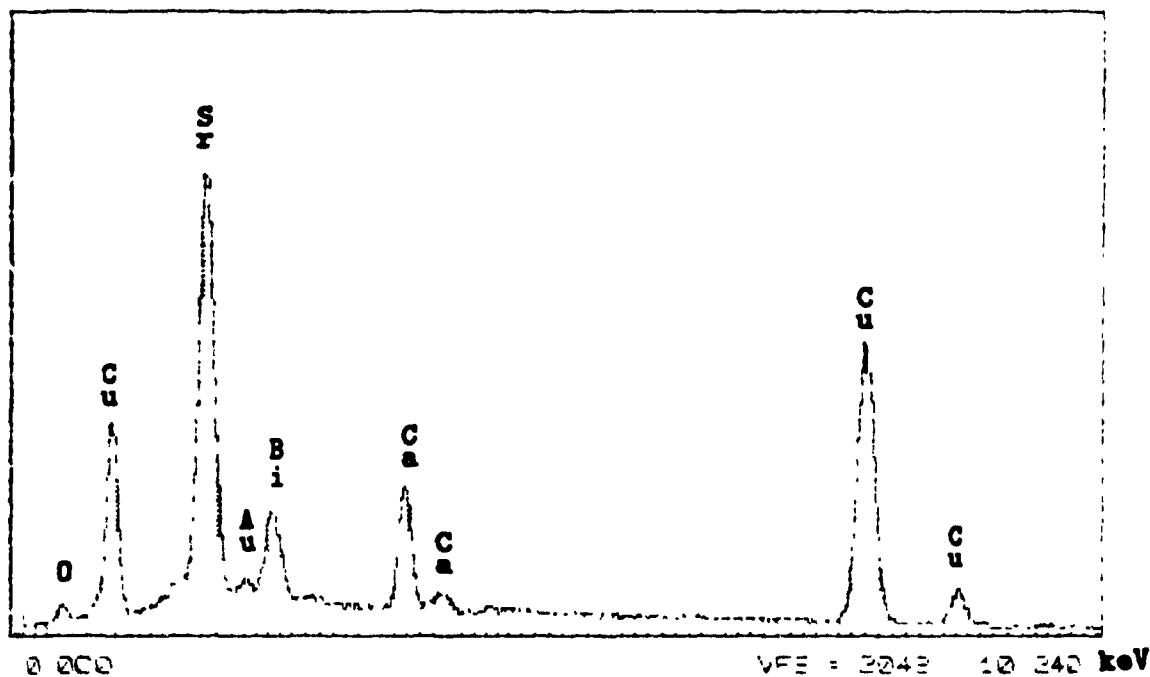


Figure 4.10: SEM EDX spectra of rough region on as-made 2:2:2:3 fibers. (The Au peak to the right of the Sr peak is due to the gold coating used to prepare the samples.)

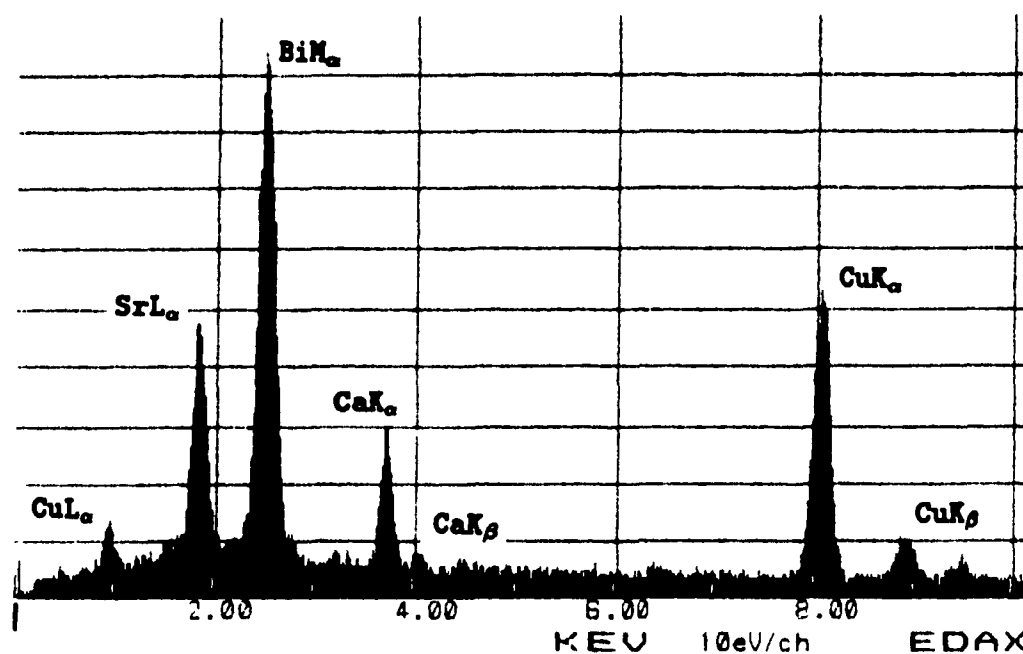


Figure 4.11: TEM EDX spectra of amorphous fragment from as-made 2:2:2:3 fibers.

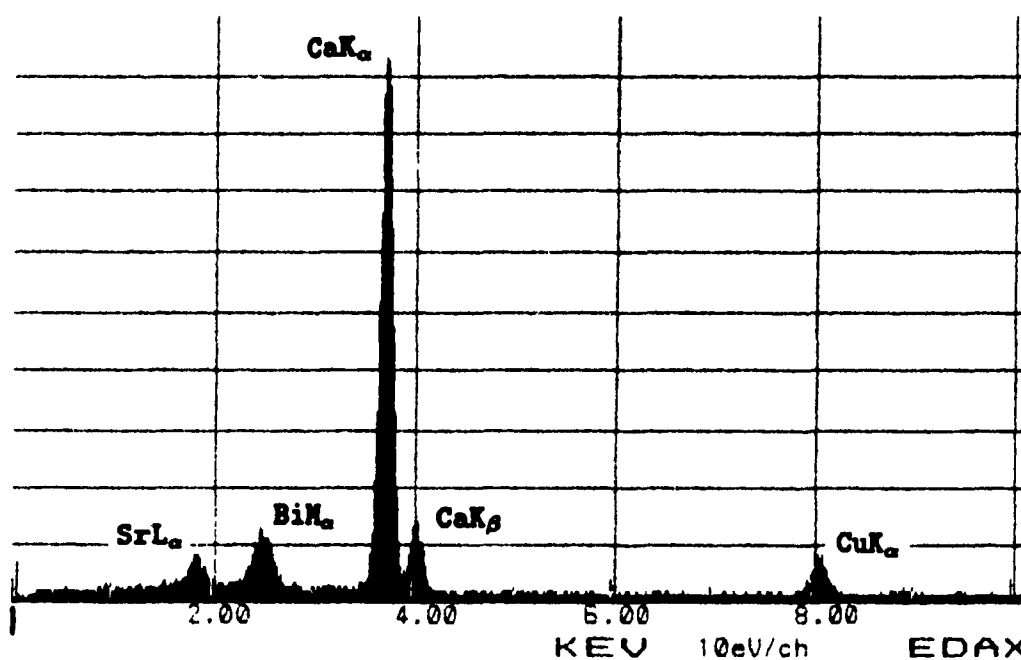


Figure 4.12: TEM EDX spectra of crystalline fragment from as-made 2:2:2:3 fibers.

4.2 Precursor Crystalline Phases

This section describes characterization of the early stages of crystallization of amorphous Bi-Sr-Ca-Cu-O fibers. Most rapid solidification work to date has concentrated on growth of the 2212 and 2223 phases and has ignored the initial amorphous-to-crystalline transition. This study pertains to thin amorphous fibers produced via melt extraction but may have relevance to crystallization of amorphous precursors produced by other rapid solidification techniques.

4.2.1 DSC Analysis

DSC measurements were performed on as-made amorphous fibers, as described in Section 3.4. A plot of heat flow vs. temperature for an isochronal run is shown in Figure 4.13. As temperature is increased, the first feature visible is the glass transition with midpoint at $T_g \simeq 685$ K. The apparent endotherm is characteristic of the glass transition but what is actually measured is an increase in the heat capacity c_p due to volume expansion as the amorphous solid melts.

A set of exotherms between 730 K and 810 K follows the glass transition. The size, shape, and peak temperature of these exotherms varies between samples, even those from the same melt-extraction run. This is probably due to small differences in composition and structure in individual fibers (see Section 4.1.2). However, two prominent peaks at approximately 750 K and 790 K are consistently present. The third exotherm at approximately 860 K is much smaller and broader but is also consistently present. The remaining small exothermic background may be due to differences in specific heat of the full sample pan and empty pan used for the background run (see Section 3.4). (The perturbations near 340 K are an instrumental artifact caused by oscillations in heat flow at the start of the run which dissipate after the DSC has stabilized.)

The results from our DSC analysis are consistent with those for differential thermal analysis reported in the literature for rapidly solidified Bi-Sr-Ca-Cu-O materials

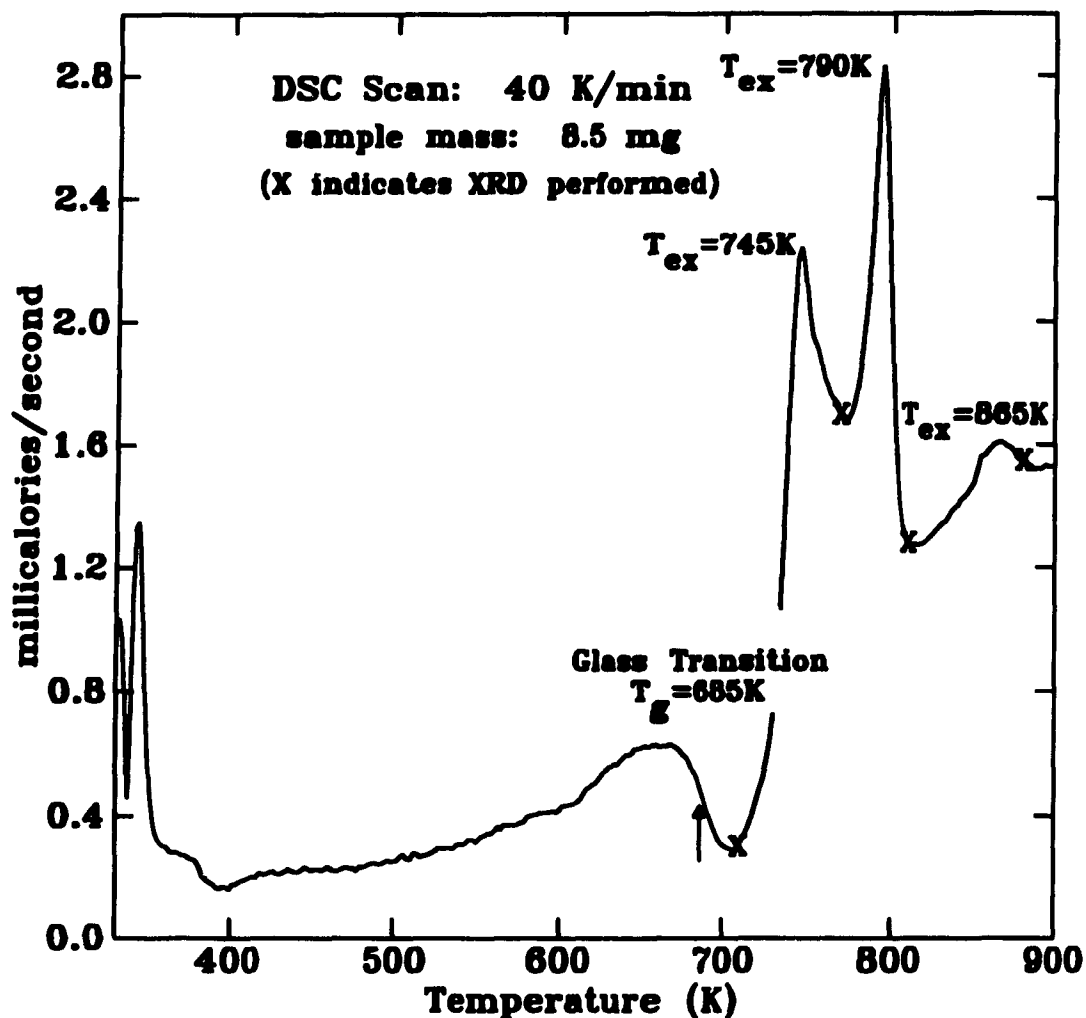


Figure 4.13: DSC isochronal run performed on 2:2:2:3 amorphous fibers (scan rate 40 K/minute, temperature range 330 K to 900 K). Note the glass transition at $T_g \approx 685\text{ K}$ and exotherms at approximately 745 K, 790 K, and 865 K. The X's indicate key points on the isochronal curve where XRD was performed. (The perturbations near 340 K are an instrumental artifact.)

(Nassau *et al.*, 1989; Shi *et al.*, 1989b; Yoshimura *et al.*, 1989; Singh and Zacharias, 1990, for example). All quote a glass transition with midpoint in the range 680 K to 685 K. The published size, shape, and peak temperature of exotherms are highly dependent on sample composition, sample preparation, and the atmosphere in which the measurements were performed. However, the general features seen in the present work agree with those seen in splat and roller quenched materials. The combined enthalpy of the first set of exotherms (730 K to 810 K) is approximately 60 J/g and is consistent with values reported by Nassau *et al.* (1989). The enthalpy of the small exotherm at 860 K is approximately 2.5 J/g. To identify the crystallization processes, x-ray diffraction was performed.

4.2.2 XRD Analysis

The crystallization of precursor phases in fibers made from a 2:2:2:3 initial composition was investigated using XRD on samples crystallized to different extents in the DSC (see Figure 4.13). The results of XRD performed on DSC samples quenched at key points on the isochronal curve and displayed in Figure 4.14. The lack of crystalline peaks in the diffraction pattern for the sample scanned to 710 K confirms that the transformation at 685 K is a glass transition. The pattern at 770 K shows a partial crystallization and at 810 K the sample is completely crystallized.

The peaks are indexed to the 2201 low T_c phase and a BCC solid-solution of randomly distributed metallic cations with lattice parameter $a=4.25$ Å proposed by Tessier (1991) for amorphous Bi-Sr-Ca-Cu-O samples produced by ball-milling. Table 4.2 lists the Miller indices, d-spacings, and $\text{CuK}\alpha$ scattering angles for the BCC phase. The BCC solid-solution is likely to be a candidate for the intermediate metastable phase formed in the conversion of the amorphous Bi-Sr-Ca-Cu-O matrix into the 2201 phase. The disordered BCC cells could form building blocks that stack

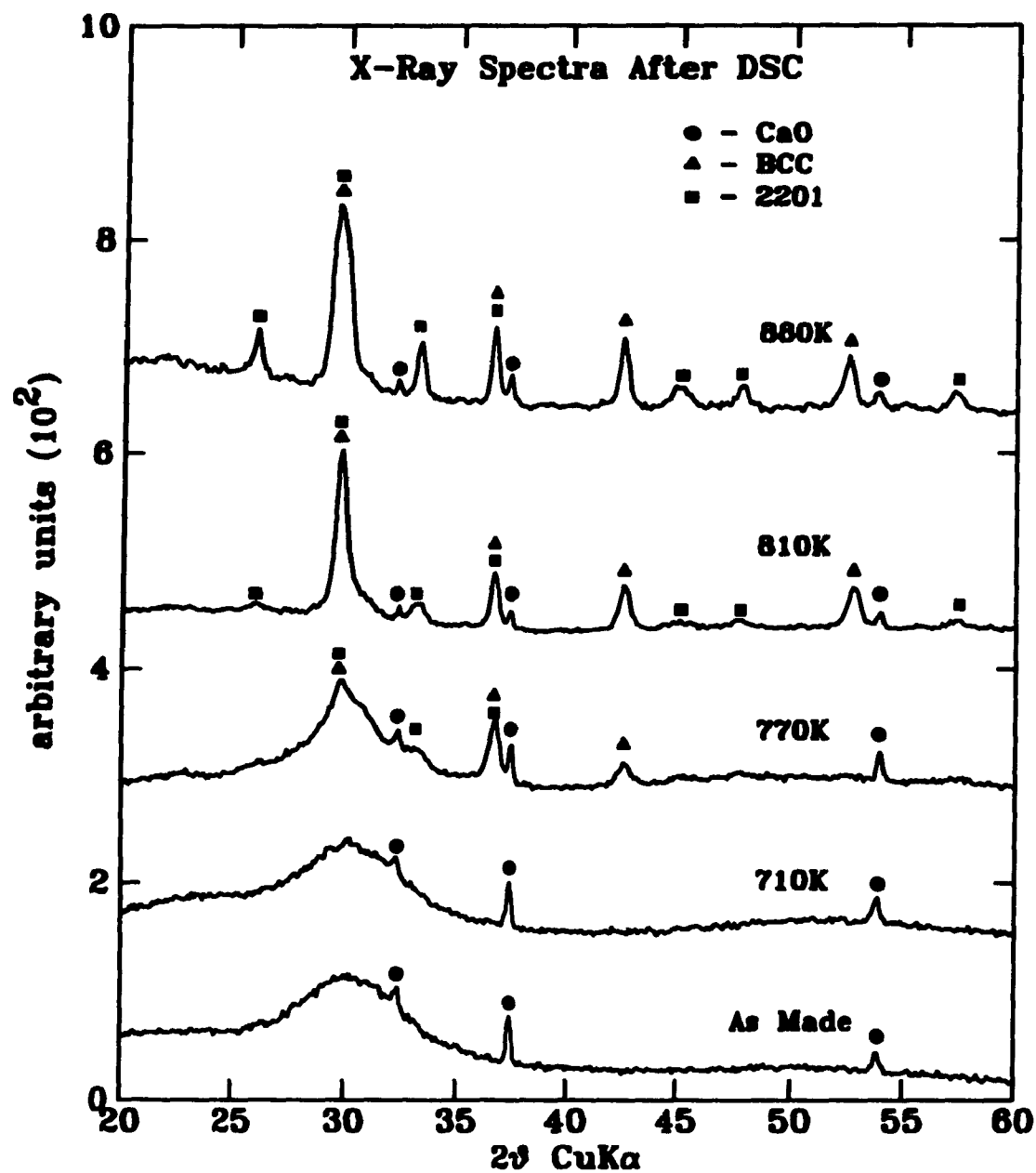


Figure 4.14: XRD patterns for DSC samples at scanned to 710 K, 770 K, 810 K, and 880 K. The spectra have been indexed to the 2201 phase and a BCC solid-solution.

BCC Solid-Solution		
Miller indices	d-spacing (Å)	scattering angle (2θ)
[110]	3.005	29.73°
[111]*	2.454	36.62°
[200]	2.125	42.54°
[210]	1.901	47.86°
[211]	1.735	52.76°

Table 4.2: Miller indices, d-spacings, and $\text{CuK}\alpha$ scattering angles for the BCC solid-solution (* forbidden reflection).

one on top of the other and convert to the nearly tetragonal 2201 phase after appropriate ordering of the atoms.² The peak at $2\theta=36.6^\circ$ is indexed to three weak 2201 lines which are not strong enough to account for the measured intensity of this peak. The [111] reflection for the BCC structure, which also lies on this peak, is forbidden. However, a degree of ordering in the BCC solid-solution towards that of the 2201 phase might account for the presence of this forbidden peak.

After the small exotherm at 860 K, the existing 2201 lines have sharpened and become stronger. A comparison of the relative intensities of the 2201 and BCC peaks for samples quenched at 810 K and 880 K shows that the BCC phase grows more quickly, and possibly earlier than the 2201 phase. At 880 K, the 2201 lines are much stronger, suggesting that the small exothermic peak centered at 860 K is related to a transformation from the BCC phase into the 2201 phase, as proposed by Tessier. Both Nassau *et al.* and Tessier report that the 2201 phase is not seen until after the exotherm near 860 K. However, Figure 4.14 shows clearly that the 2201 phase is present after scanning to 810 K.

²By examination of the schematic diagram for the 2201 crystal structure in Figure 2.4, one can imagine a vertical column of BCC cells expanding in the a-b directions, contracting in the c direction, and re-ordering to form the 2201 phase.

Isothermal experiments performed on the 2:2:2:3 samples confirm that the BCC solid-solution is a metastable intermediate phase, eventually converting to the 2201 phase. Samples held at 810 K for 1 hour have similar XRD patterns to those scanned to 880 K and quenched (see Figure 4.15). For fibers held at 880 K for 1 hour, the relative strength of the BCC lines is much weaker than in the other two patterns. The BCC phase gradually transforms into the 2201 phase over time.

In summary, the crystallization of amorphous Bi-Sr-Ca-Cu-O fibers into the superconducting 2201 phase has been shown to proceed via the formation of a disordered metastable intermediate phase. The growth of the higher T_c 2212 and 2223 phases is discussed in the following section.

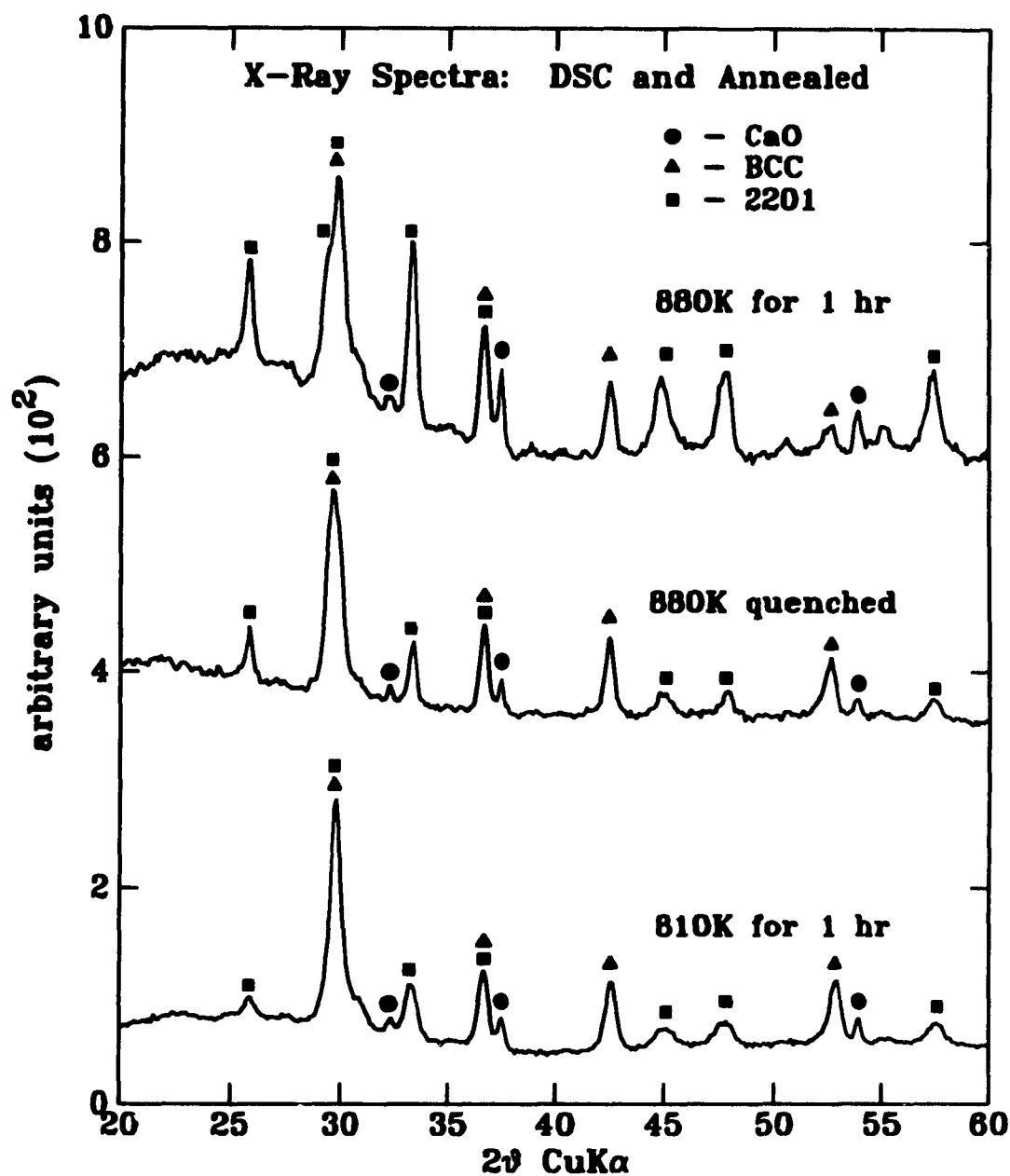


Figure 4.15: XRD patterns for 2:2:2:3 fibers held isothermally at 810 K for 1 hour, scanned to 880 dgk and quenched, and held isothermally 880 K for 1 hour. The lines are indexed as in Figure 4.14. (The broad peak centered at $2\theta=25^\circ$ in the scan at 880 K for 1 hour is due to background from the sample holder.)

4.3 High T_c Phases

As-made amorphous fibers fabricated from precursor pellets with initial compositions listed in Section 3.1 were subjected to heat treatment as described in Section 3.3. The growth of 2212 and 2223 phases was studied as a function of initial composition and annealing conditions. The evolution of grain structure with anneal time and the effect of fiber diameter on grain growth was examined using SEM analysis. Transmission electron microscopy (including High Resolution TEM) and EDX microanalysis were used to identify the 2212 and 2223 phases in annealed fibers.

4.3.1 Lead-Free Initial Compositions

Fibers produced from precursor pellets with initial compositions of 2:2:2:3, 2:2:3:4, and 2:2:4:5 crystallized mainly into the 2212 ($T_c=85$ K) phase. Samples were annealed at temperatures between 1125 K and 1145 K, these being the optimal temperatures reported in the literature (Shi *et al.*, 1989b). No difference was found between samples annealed at different temperatures in this range. As a rule, fibers of diameter less than about 10 μm did not survive the heating process, probably because they coarsened and broke apart. However, on occasion fibers with diameters as small as 1 μm were crystallized into *continuous* filaments of single-grain chains as shown in Figure 4.16. The ability to produce such crystalline filaments has been reported by workers using the gas-jet fiberization technique mentioned in Section 1.3.3 (Miller *et al.*, 1990).

A marginal enhancement of the fraction of 2223 phase ($T_c=110$ K) was affected by the presence of excess calcium and copper. Figure 4.17 shows XRD patterns for annealed 2:2:2:3 and 2:2:3:4 fibers indexed to the 2212 and 2223 phases. This finding is similar to those of Shi *et al.* (1989c).

4.3.2 Lead-Substituted Initial Compositions

Fibers of initial composition (1.8:0.2):2:2:3, (1.8:0.2):2:3:4, and (1.6:0.4):2:2:3 (where the order of the cations is listed in Section 3.1) had roughly twice the volume fraction

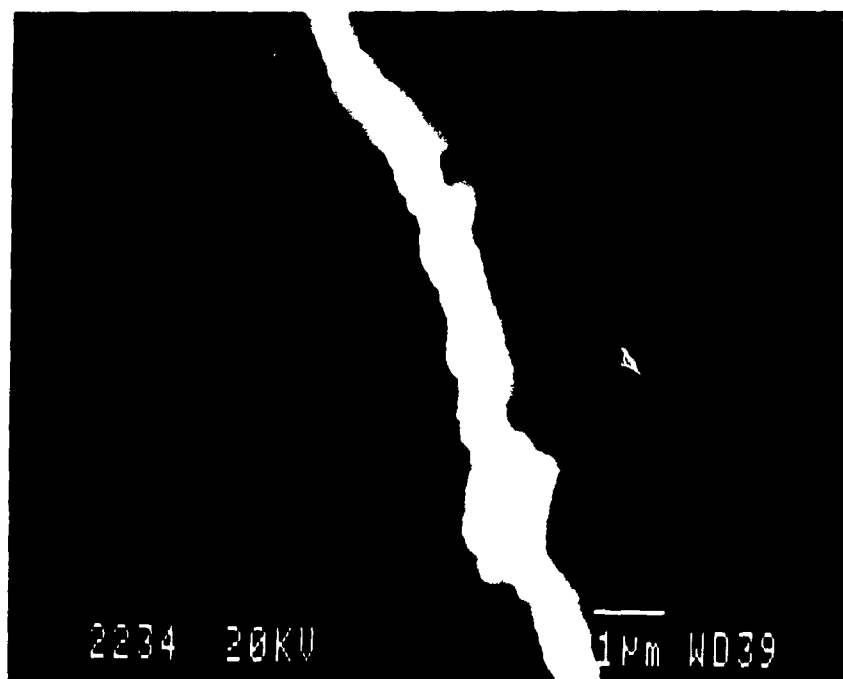


Figure 4.16: SEM micrograph of a $1\text{ }\mu\text{m}$ Bi-Sr-Ca-Cu-O fiber crystallized into a continuous filament with single-grain chains. The scale marker is $1\text{ }\mu\text{m}$ long.

of the 2223 phase after heat treatment as those without lead substitution, though 2212 was still the majority phase (see Figure 4.17). No quantitative analysis was attempted due to the complex nature of the diffraction patterns. No consistent difference in the amount of 2223 phase could be detected in samples annealed at 1135 K and 1145 K for equal times. Variations in sample composition likely dominate over effects due to anneal temperature. Nor was an increase in the volume fraction of 2223 phase with anneal time found by XRD (see Figure 4.18). The amount of 2223 phase seems to have saturated after annealing for 1 hour. Figure 4.19 shows an XRD pattern for fibers of initial composition (1.8:0.2):2:3:4 annealed for 14.5 hours. (The shoulder visible at approximately 31.5° in all the lead-substituted annealed fibers is indexed to Ca_2PbO_4 .) The possibility of producing majority phase 2223 samples was demonstrated by annealing a (1.8:0.2):2:3:4 precursor pellet at 1145 K for 9 days. The XRD pattern of Figure 4.20 shows that this sample is almost single phase 2223. The insets in Figures 4.19 and 4.20 show the [002] peaks for the 2212 and 2223 phases.

The lack of overlap between peaks of the different phases for this reflection allows unambiguous determination of the majority phase.

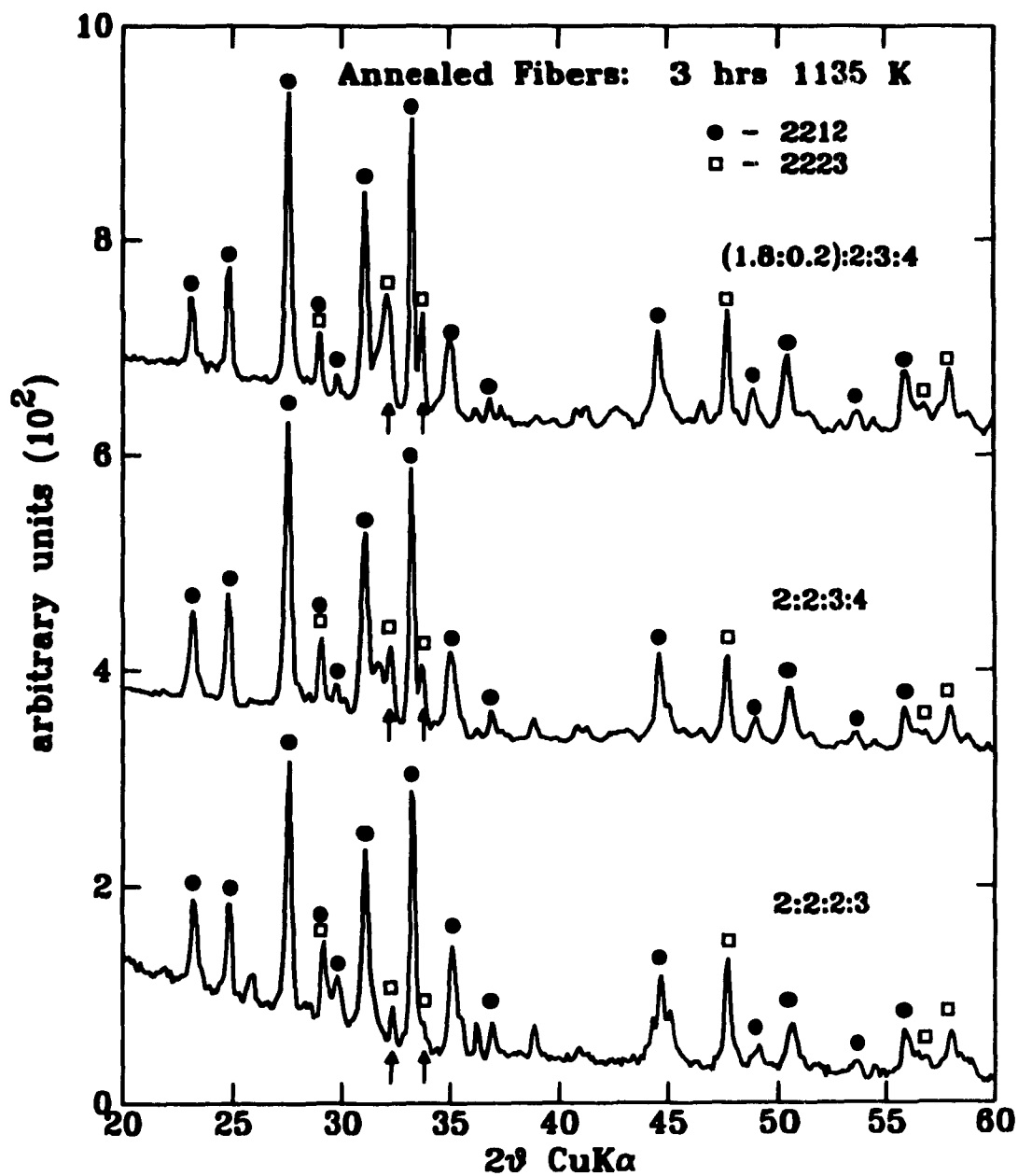


Figure 4.17: XRD patterns of annealed 2:2:2:3, 2:2:3:4 and (1.8:0.2):2:3:4 fibers (1135 K for 3 hours). Notice the increasing intensity of the 2223 lines (denoted by the arrows) as the composition changes from 2:2:2:3 to 2:2:3:4 to (1.8:0.2):2:3:4.

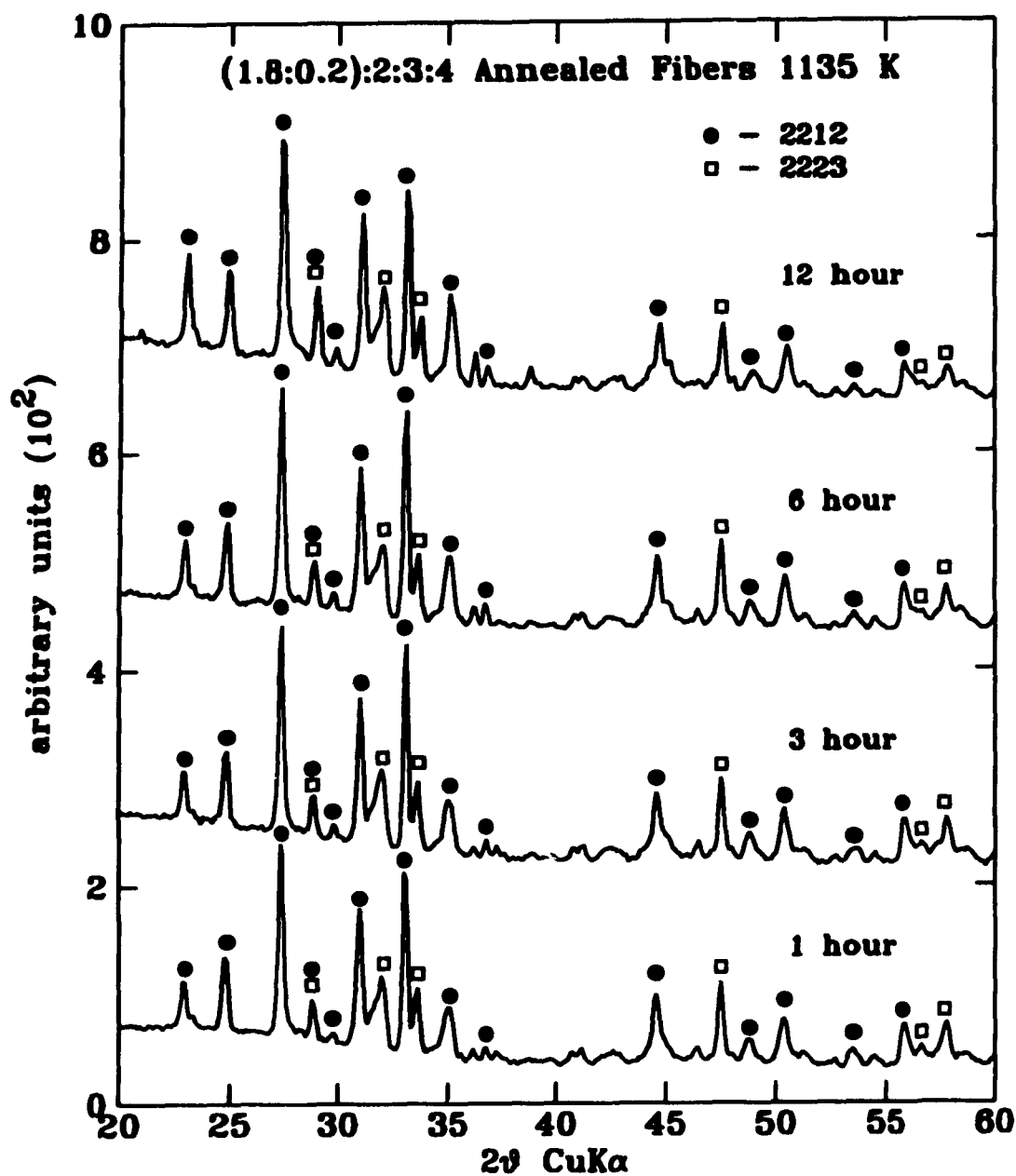


Figure 4.18: XRD patterns for (1.8:0.2):2:3:4 fibers annealed at 1135 K for 1, 3, 6, and 12 hours. (The peaks are indexed to 2212 and 2223 phases. The shoulder at 31.5° is indexed to Ca_2PbO_4 .)

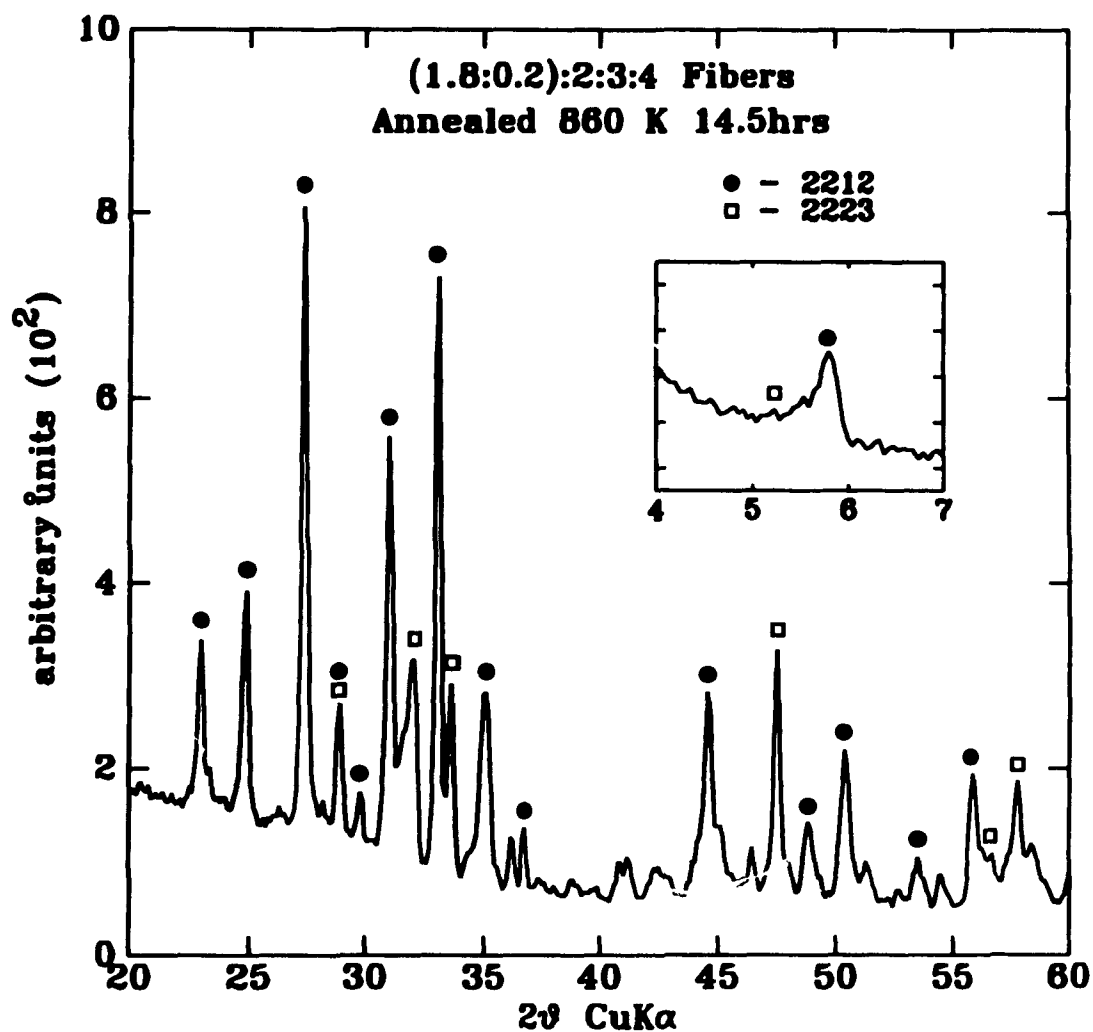


Figure 4.19: XRD patterns for (1.8:0.2):2:3:4 fibers annealed at 1135 K for 14.5 hours. The inset shows the [002] peak for 2212 and 2223 phases. (The shoulder at 31.5° is indexed to Ca_2PbO_4 .)

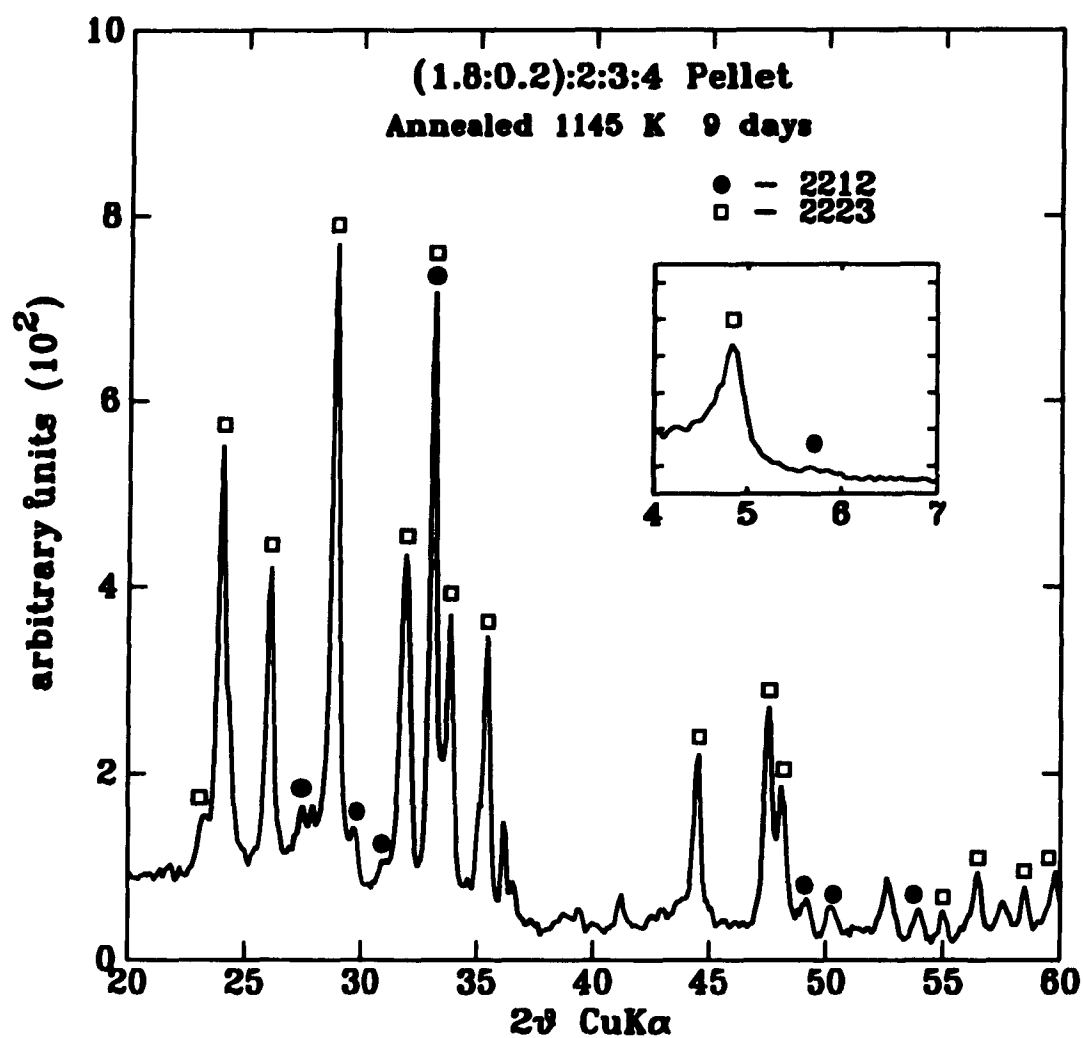


Figure 4.20: XRD pattern of (1.8:0.2):2:3:4 pellet annealed at 1145 K for 9 days. The majority phase is 2223.

4.3.3 SEM analysis

Fibers of composition (1.8:0.2):2:2:3 were annealed at 1135 K for 1, 3, 6, and 12 hours and examined using SEM analysis. Figures 4.21 through 4.24 show SEM micrographs of time evolution of grain structure for these fibers (all between 10 μm and 20 μm in diameter). Grain size increased with anneal time from 2.5 μm long and 0.3 μm thick after annealing for 1 hr to 5 μm to 6 μm long and 0.5 μm thick after annealing for 12 hours, both at 1135 K. The rate of grain growth is also dependent on fiber diameter. Thinner fibers annealed for short anneal times have similar morphology to thicker fibers annealed for longer times.

There is little texturing apparent in the annealed fibers. Two distinct grain structures are apparent: long, thin grains (*acicular*) and thick, fat grains (*equiaxed*). The two structures are generally interspersed throughout each fiber but some segregation occurs, as is visible in Figure 4.21. SEM EDX microanalysis indicates that the acicular grains are possibly 2212 and 2223 phase and that the equiaxed grains are deficient in bismuth (see Figures 4.25 and 4.26).³ In addition, a plate-like morphology is exhibited in samples annealed for longer times (see Figure 4.24). This characteristic is often reported in the literature (Asthana *et al.*, 1991, for example).

³See Section 4.1.2 for a description of the limitations of SEM EDX microanalysis.

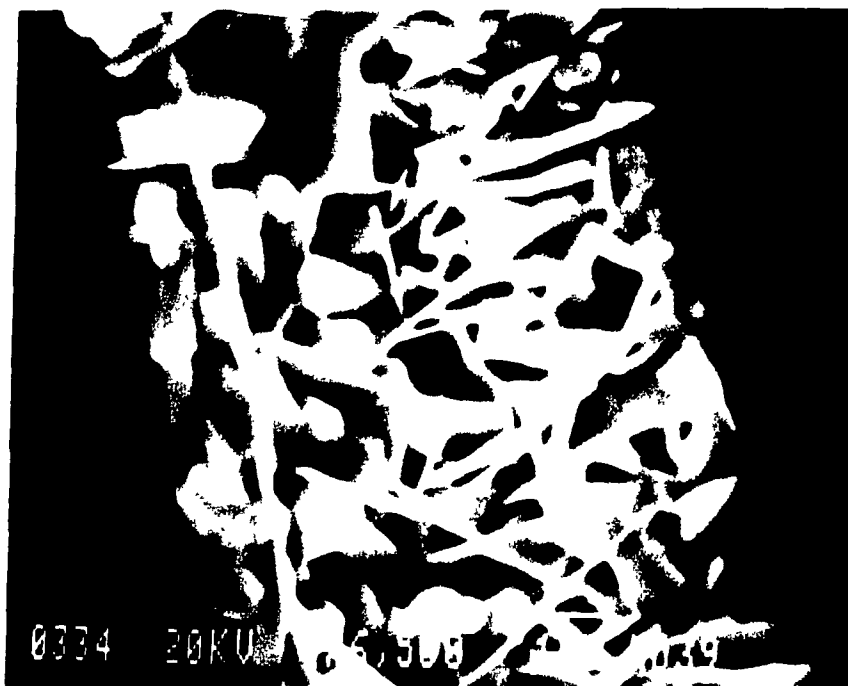


Figure 4.21: SEM micrograph of (1.8:0.2):2:2:3 fibers annealed for 1hr at 1135 K. The scale marker is 1 μm long. The thin grains on the right are approximately 2.5 μm long and 0.3 μm thick. Note the segregation of thin grains and thick grains.



Figure 4.22: SEM micrograph of (1.8:0.2):2:2:3 fibers annealed for 3 hours at 1135 K. The scale marker is 1 μm long. The thin grains are approximately 3.5 μm long and 0.4 μm thick.



Figure 4.23: SEM micrograph of (1.8:0.2):2:2:3 fibers annealed for 6 hours at 1135 K. The scale marker is 1 μm long. The thin grains are approximately 4.5 μm long and 0.5 μm thick.

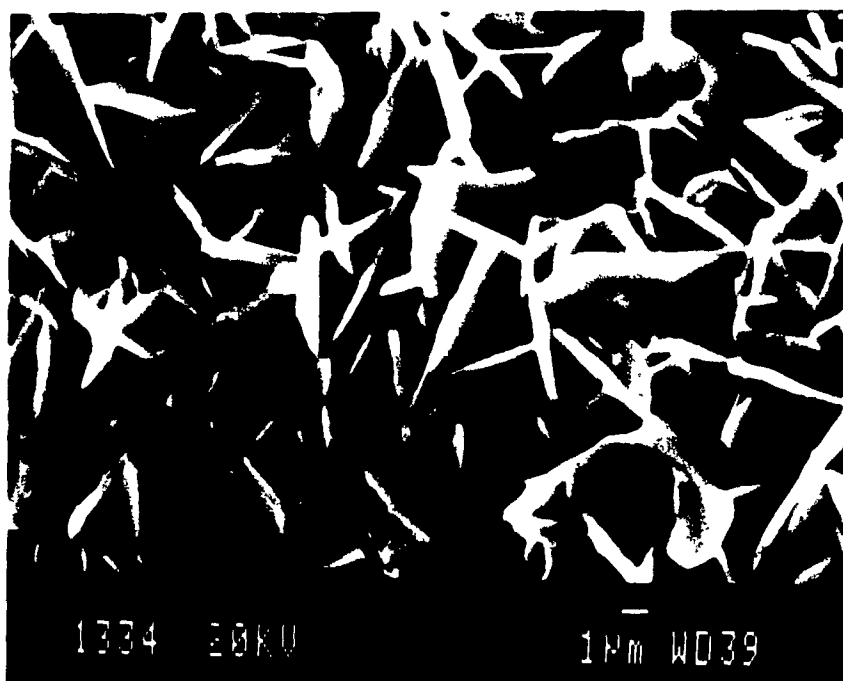


Figure 4.24: SEM micrograph of (1.8:0.2):2:2:3 fibers annealed for 12 hours at 1135 K. The scale marker is 1 μm long. The thin grains are approximately 5 μm to 6 μm long and 0.5 μm thick (note the plate-like morphology and lack of texturing).

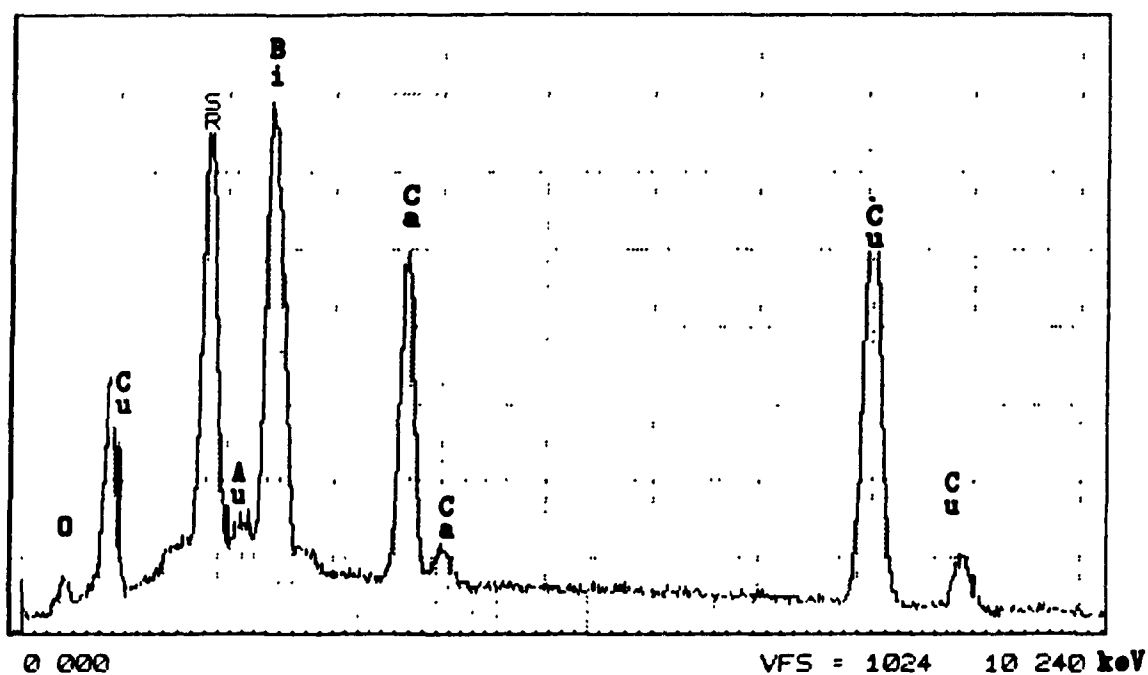


Figure 4.25: SEM EDX spectra for thin grain in annealed (1.8:0.2):2:2:3 fibers. (The Au peak to the right of the Sr peak is due to gold plating used to prepare the samples.)

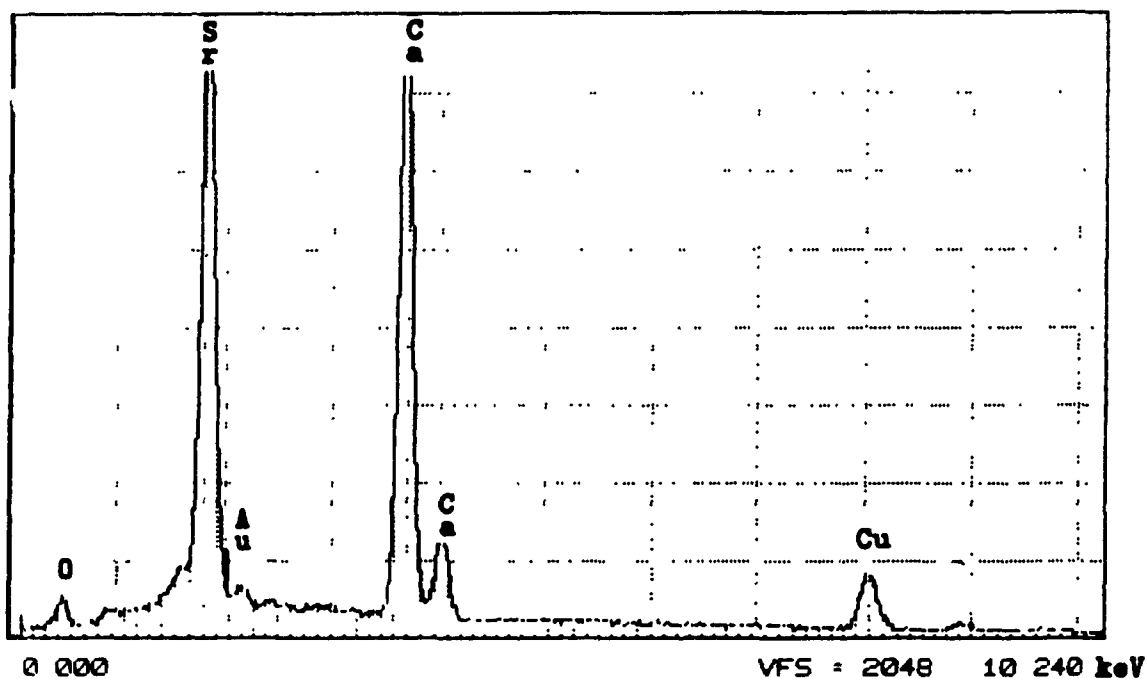


Figure 4.26: SEM EDX spectra for thick grain in annealed (1.8:0.2):2:2:3 fibers. (The Au peak to the right of the Sr peak is due to gold plating used to prepare the samples.)

4.3.4 TEM Analysis

TEM EDX microanalysis on annealed 2:2:3:4 and (1.8:0.2):2:3:4 fibers confirmed the presence of the high T_c 2212 and 2223 phases. Figures 4.27 and 4.28 show typical EDX spectra for 2212 and 2223 crystal grains and Table 4.3 lists the measured composition for these grains. In addition to the superconducting phases, crystal grains containing

Element	atomic percent ($\pm 10\%$)	
	2212	2223
bismuth	25	20
strontium	33	23
calcium	13	19
copper	29	38

Table 4.3: Composition of 2212 and 2223 crystal grains found in annealed (1.8:0.2):2:3:4 fibers (atomic percent (%)).

predominantly calcium and copper were identified by EDX. They were found to occur consistently in regions surrounding 2223 crystal grains. Figures 4.29 through 4.30 show spectra of typical fragments from such crystal grains with composition ranging from nearly pure calcium to nearly pure copper. This finding supports the model of Shi *et al.* (Shi *et al.*, 1989b) involving diffusion of calcium and copper into 2212 grains to form the 2223 phase. However, the XRD results for our samples do not show the presence of Ca_2CuO_3 as was reported by this group.

The excess calcium and copper is expected since the initial stoichiometry is rich in these two elements. Also found in the annealed fibers were crystal grains rich in calcium, copper, and strontium (see Figure 4.31). There was no correlation between the location of these grains and the high T_c phases. The apparent deficiency in bismuth in the 2212 and 2223 grains relative to the initial composition (see Table 4.3) and presence of excess strontium, calcium, and copper in the remainder of the fibers

suggests that bismuth was lost during fiber fabrication and/or heating.⁴ This is consistent with the greater volatility of bismuth oxide.

The superconducting 2212 and 2223 phases were also identified by High Resolution TEM analysis (HRTEM). Figure 4.32 shows a lattice fringe image of a grain fragment containing 2212 and 2223 phases. In most of these fragments, c-axis was found to be perpendicular to the long dimension of the grain, as is seen here. This is consistent with findings reported in the literature (Xu *et al.*, 1990, for example). Diffraction patterns and lattice fringe images showed lattice spacings of approximately 15 Å and 18 Å. These spacings correspond to half the c-axis lattice parameters of the 2212 and 2223 phases (see Section 2.3). Figure 4.33 shows enlarged HRTEM lattice fringe images for 2212 and 2223 crystal grains and Figure 4.34 shows TEM diffraction patterns for the same crystal grains. Visible in the lattice fringe images are intergrowths of 2212 and 2223 phases which can be identified by the number of copper oxide layers between darker BiO₂ layers. The incommensurate modulation of the Bi-Sr-Ca-Cu-O systems is also apparent in the HRTEM lattice fringe images (see Figure 4.35), the dark regions being Bi-concentrated zones (Matsui *et al.*, 1988). Figure 4.36 the corresponding diffraction pattern exhibiting satellite spots resulting from the incommensurate modulation.

⁴As mentioned in Section 4.1.2, the compositions as determined by EDX are unreliable due to a lack of reference standards. However, the combined evidence strongly suggests that there is a real deficiency of Bi in the as made fibers fibers.

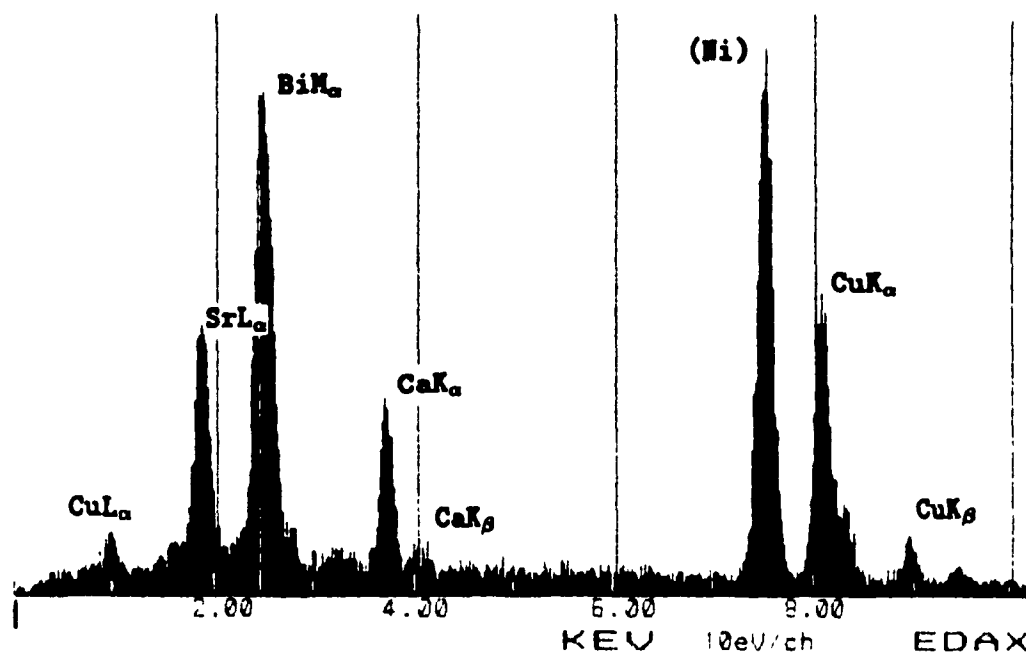


Figure 4.27: TEM EDX spectra of 2212 crystal grain found in annealed (1.8:0.2):2:3:4 fiber. (The peak at 7.5 keV is NiK_α from the nickel grid.)

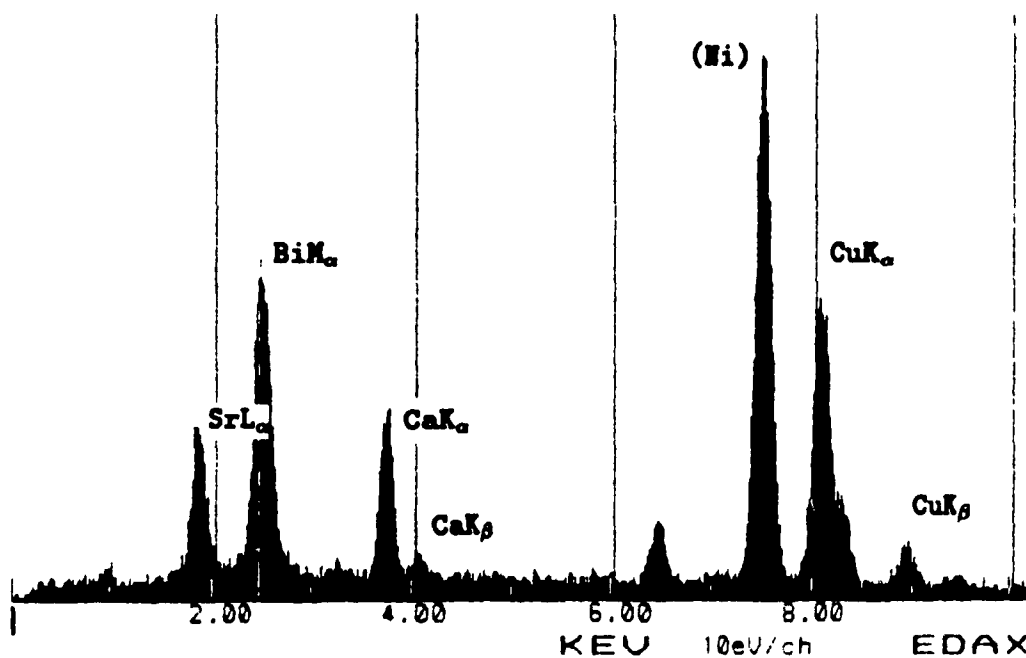
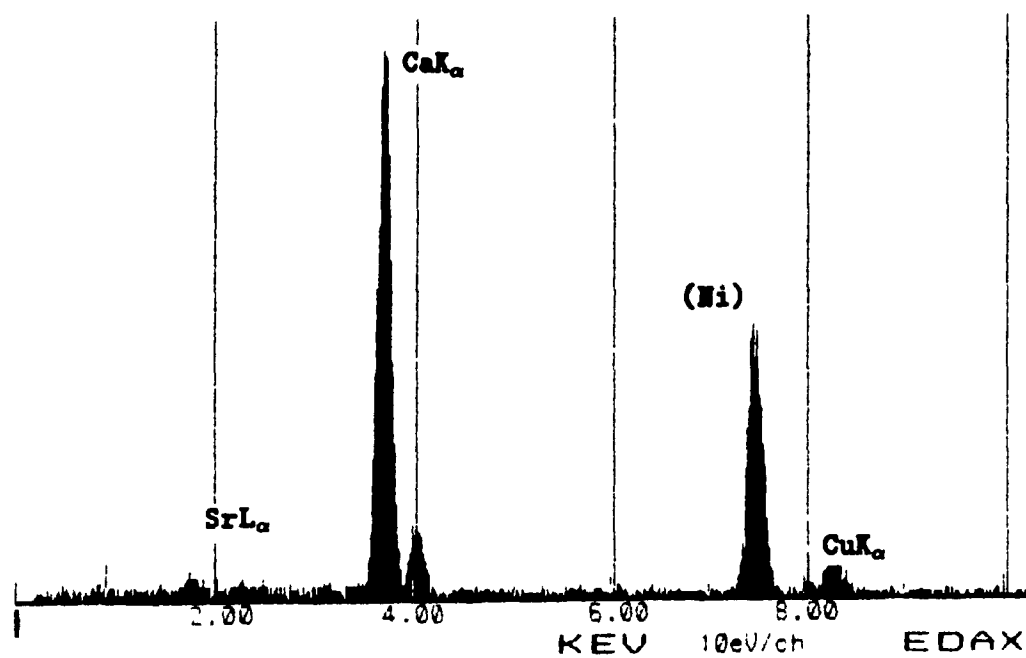
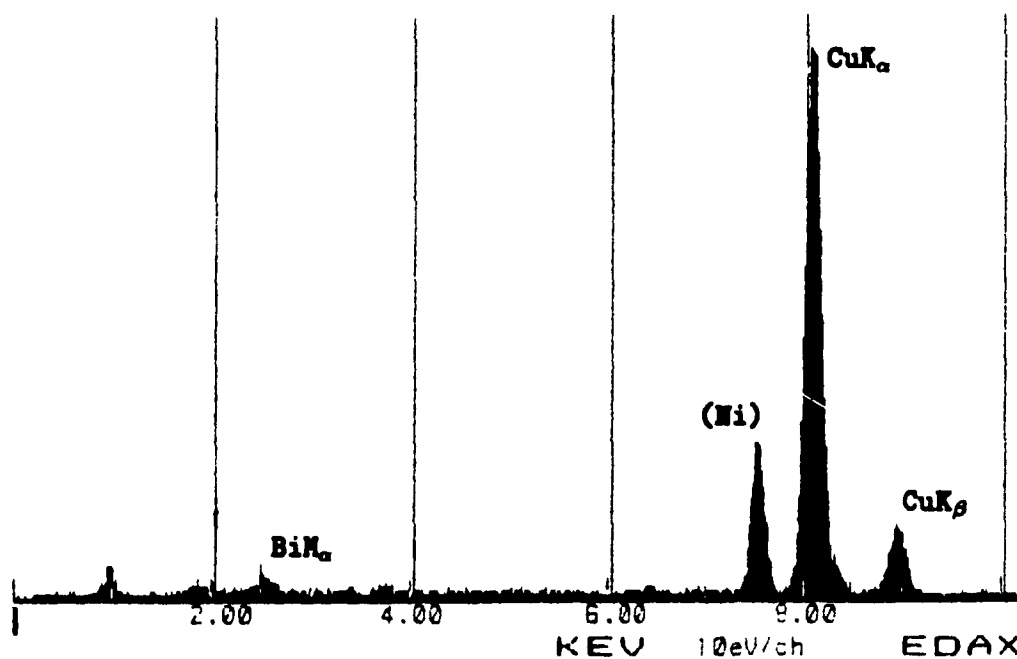


Figure 4.28: TEM EDX spectra of 2223 crystal grain found in annealed (1.8:0.2):2:3:4 fiber. (The peak at 7.5 keV is NiK_α from the nickel grid and the peak at 6.4 keV is background from the sample holder.)



(a)



(b)

Figure 4.29: TEM EDX spectra of calcium (a) and copper (b) rich crystal grains found in annealed (1.8:0.2):2:3:4 fiber. (The peak at 7.5 keV is NiK α from the nickel grid.)

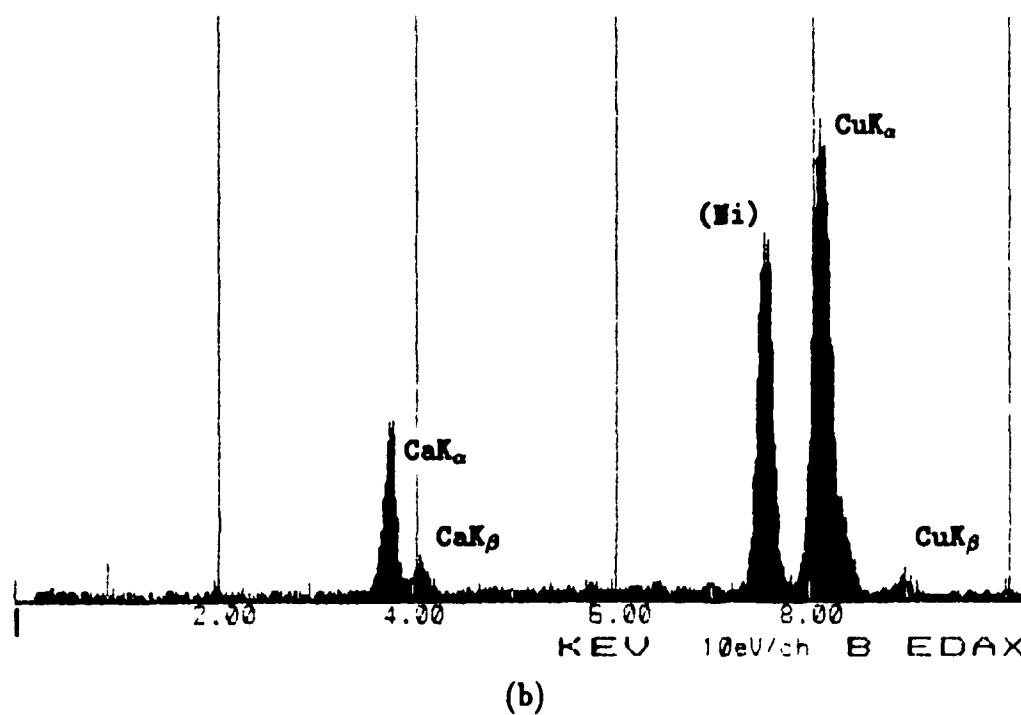
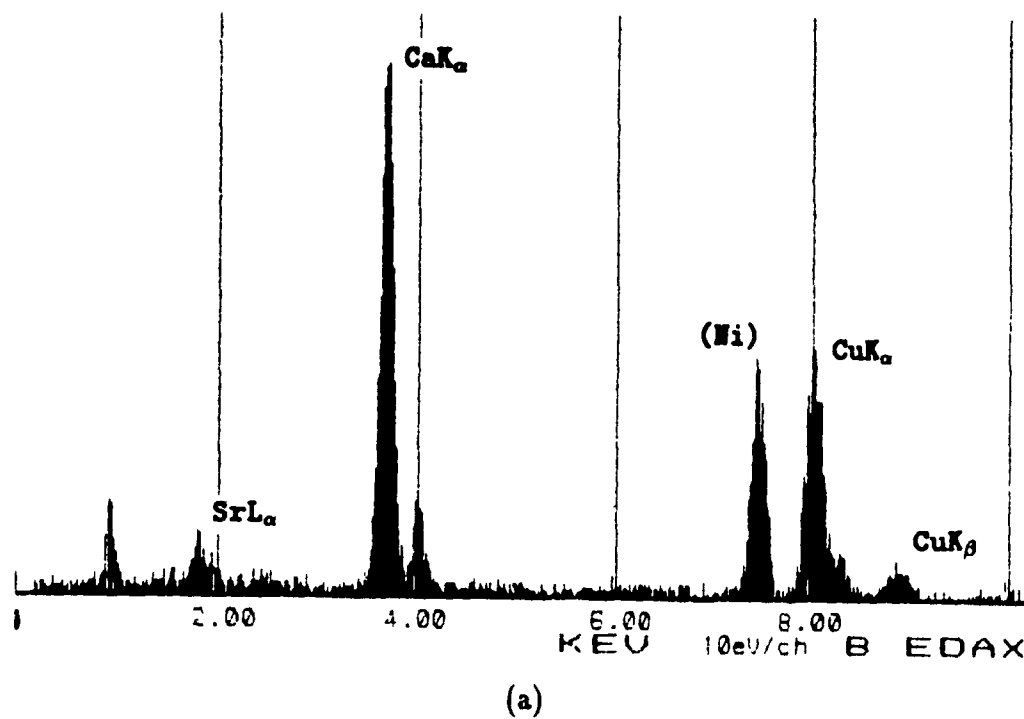


Figure 4.30: TEM EDX spectra of calcium and copper (mixed) crystal grains found in annealed (1.8:0.2):2:3:4 fiber. (The peak at 7.5 keV is NiK α from the nickel grid.)

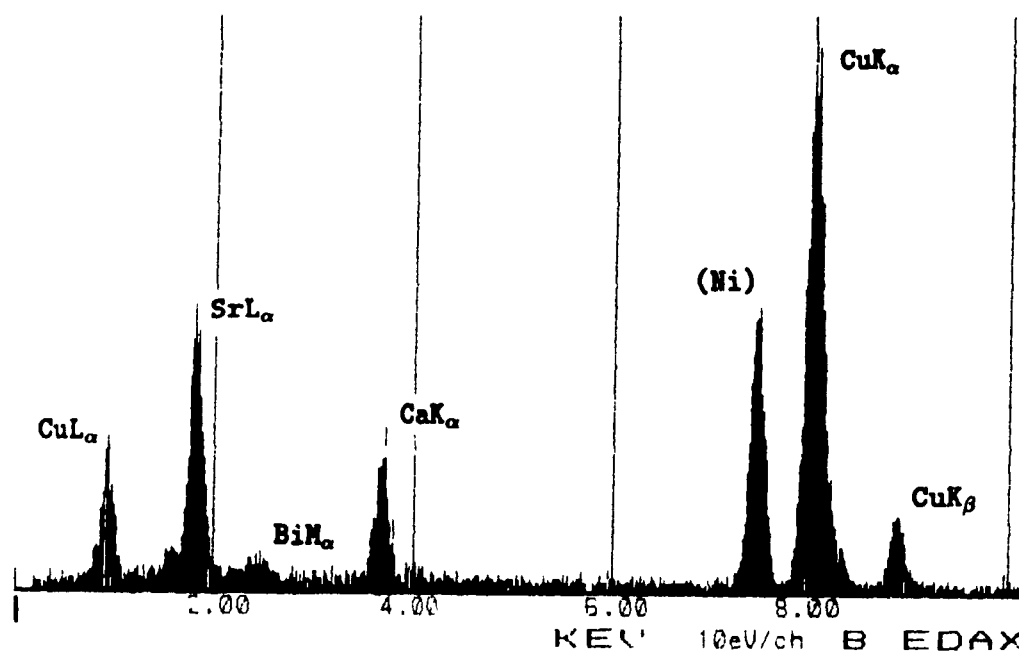
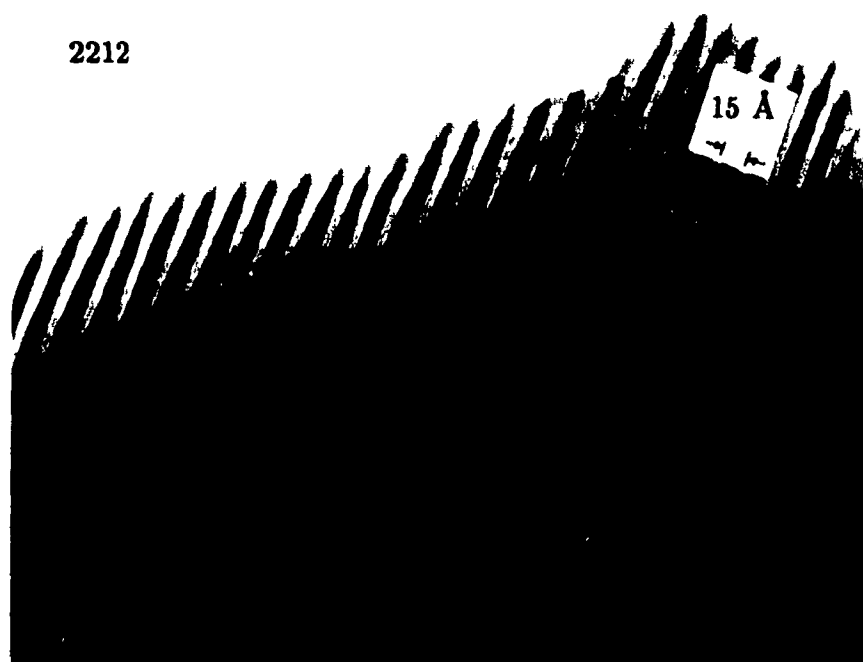


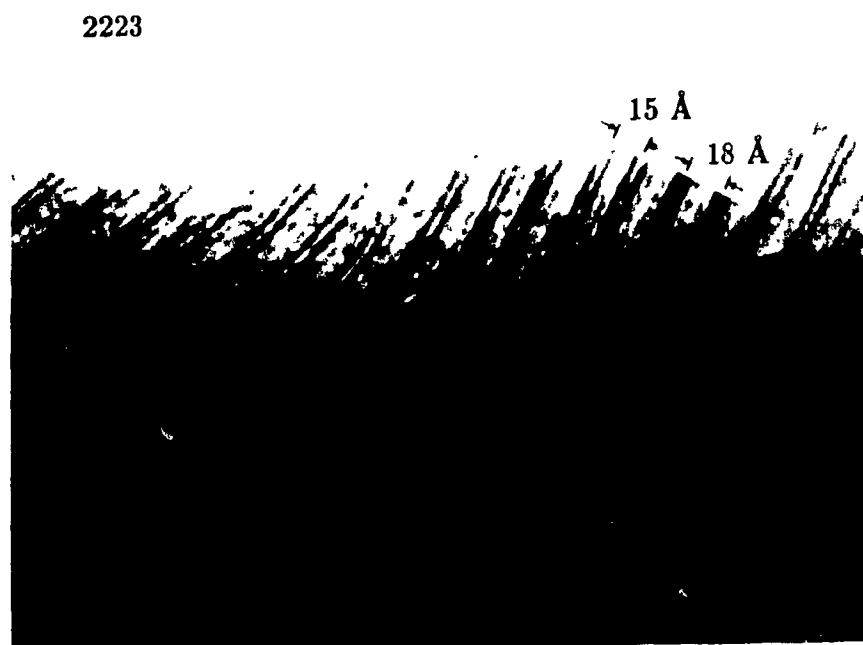
Figure 4.31: TEM EDX spectra of calcium, copper and strontium crystal grains found in annealed (1.8:0.2):2:3:4 fiber. (The peak at 7.5 keV is NiK_α from the nickel grid.)



Figure 4.32: HRTEM lattice fringe image of crystal grain containing superconducting phases. Notice the alignment of the c-axis lengthwise with the crystal grain.

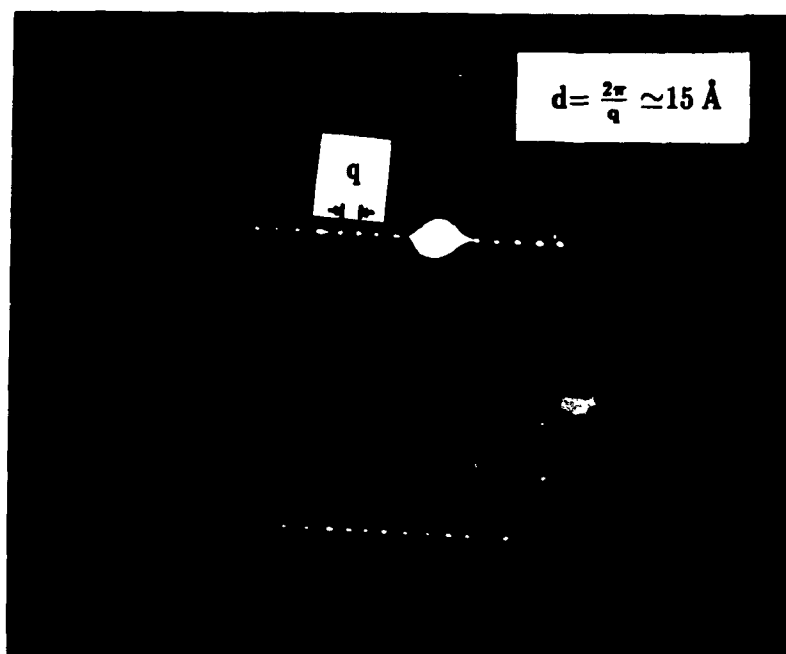


(a)

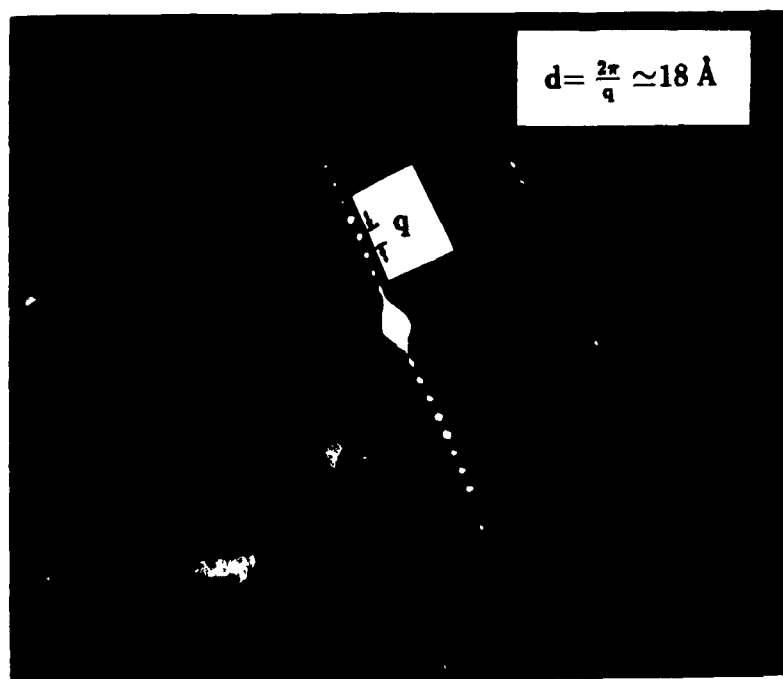


(b)

Figure 4.33: HRTEM lattice fringe images of 2212 (a) and 2223 (b) crystal grains found in annealed (1.8:0.2):2:3:4 fiber. The 15 Å layer in (b) is a 2212 intergrowth within the 2223 crystal grain.



(a)



(b)

Figure 4.34: TEM diffraction patterns for 2212 (a) and 2223 (b) crystal grains found in annealed (1.8:0.2):2:3:4 fiber. The q -spacings (scattering wavevector) between spots correspond to lattice spacings of approximately 15 Å (a) and 18 Å (b).

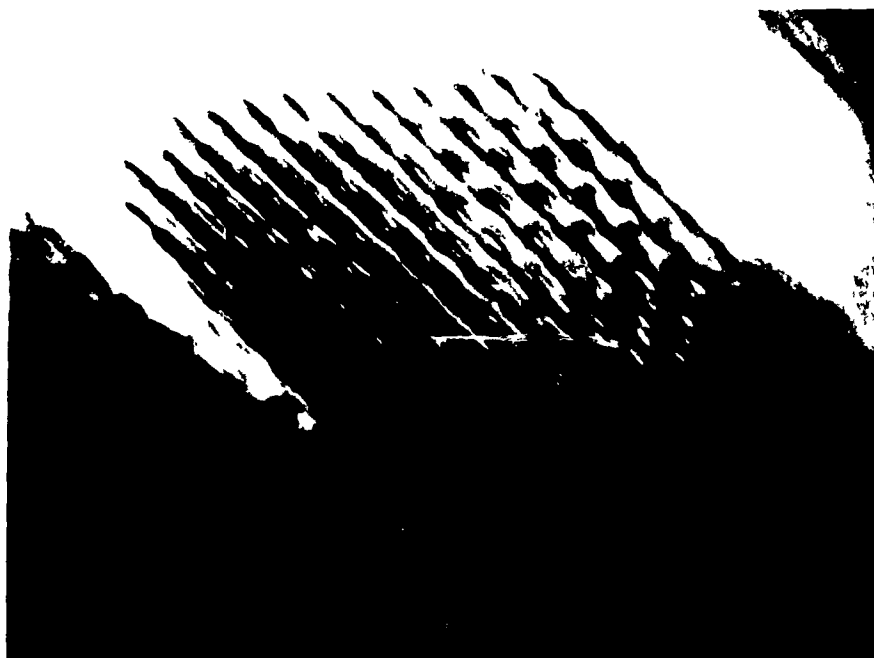


Figure 4.35: HRTEM lattice fringe image showing incommensurate modulation in the a-b plane in a 2212 crystal grain. The dark regions are Bi-concentrated zones.

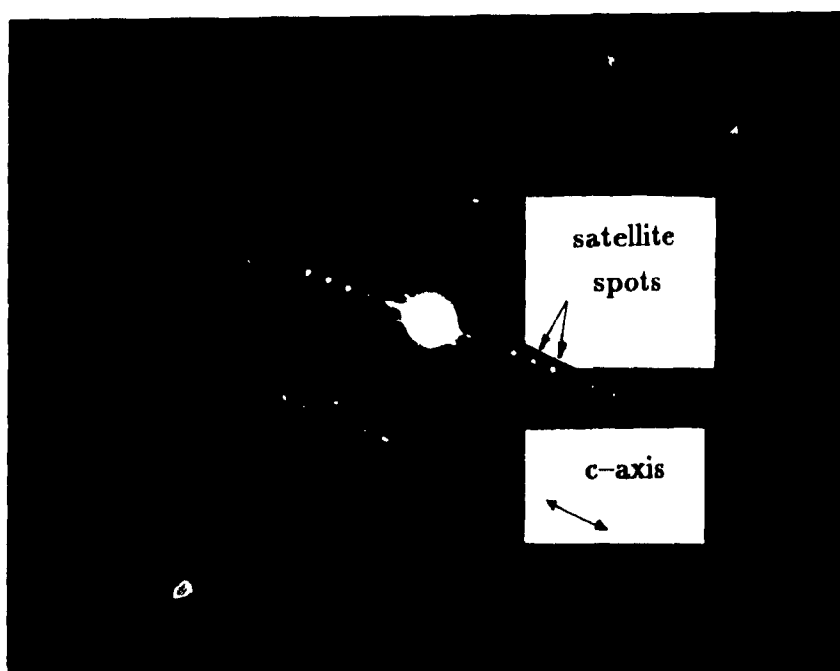


Figure 4.36: TEM diffraction pattern showing showing satellite spots due to incommensurate modulation in the a-b plane in a 2212 crystal grain.

4.3.5 SQuID Magnetometry

SQuID magnetometry performed on (1.8:0.2):2:3:4 fibers annealed at 870°C for 12 hours shows two superconducting transitions: one at 82 K and another at 105 K. A plot of magnetization vs. temperature for (1.8:0.2):2:3:4 fibers annealed at 870°C for 12 hours is shown in Figure 4.37. The two curves are for zero-field cooled (ZFC) and field cooled (FC) as labelled. The applied field was 50 mT.

Superconducting transitions are visible at 105 K and 82 K. These transitions correspond to the 2212 and 2223 superconducting phases respectively. The volume fractions of these phases were determined from the ZFC to be approximately 30% 2212 and 5% 2223 at 30 K. These values were calculated using Equation 2.1 (see Section 2.1.1) and a theoretical value for the density $\rho \simeq 7 \text{ g/cm}^3$ (Matheis and Snyder, 1990). The penetration depth for the Bi-Sr-Ca-Cu-O superconducting compounds is approximately 150 Å (LeBeau *et al.*, 1989; Uemura *et al.*, 1989; Gygax *et al.*, 1989) which is of the same order as the grain size in the annealed fibers (see Section 4.3.3). Therefore, some flux penetration is to be expected and the actual volume fractions are likely to be higher than the calculated values. A more precise determination of the volume fraction of superconducting material is complicated by the random orientation of the crystal grains and the unknown nature of the intergranular links within the annealed fibers. A comparison of the FC and ZFC curves reveals that a significant amount of flux pinning is present.

Magnetization measurements on other annealed fiber samples showed only the transition at 82 K. Figure 4.38 shows the magnetization curve for (1.6:0.4):2:2:3 fibers annealed at 870°C for 12 hours. The volume fraction of 2212 phase was determined to be approximately 20%. The response below 80 K of these fibers is identical to that of the (1.8:0.2):2:3:4 fibers. The absence of detectable amounts of 2223 phase in annealed (1.6:0.4):2:2:3 fibers suggests that 20% substitution of Pb for Bi exceeds the optimal value and that excess Ca and Cu are necessary for growth of this phase.

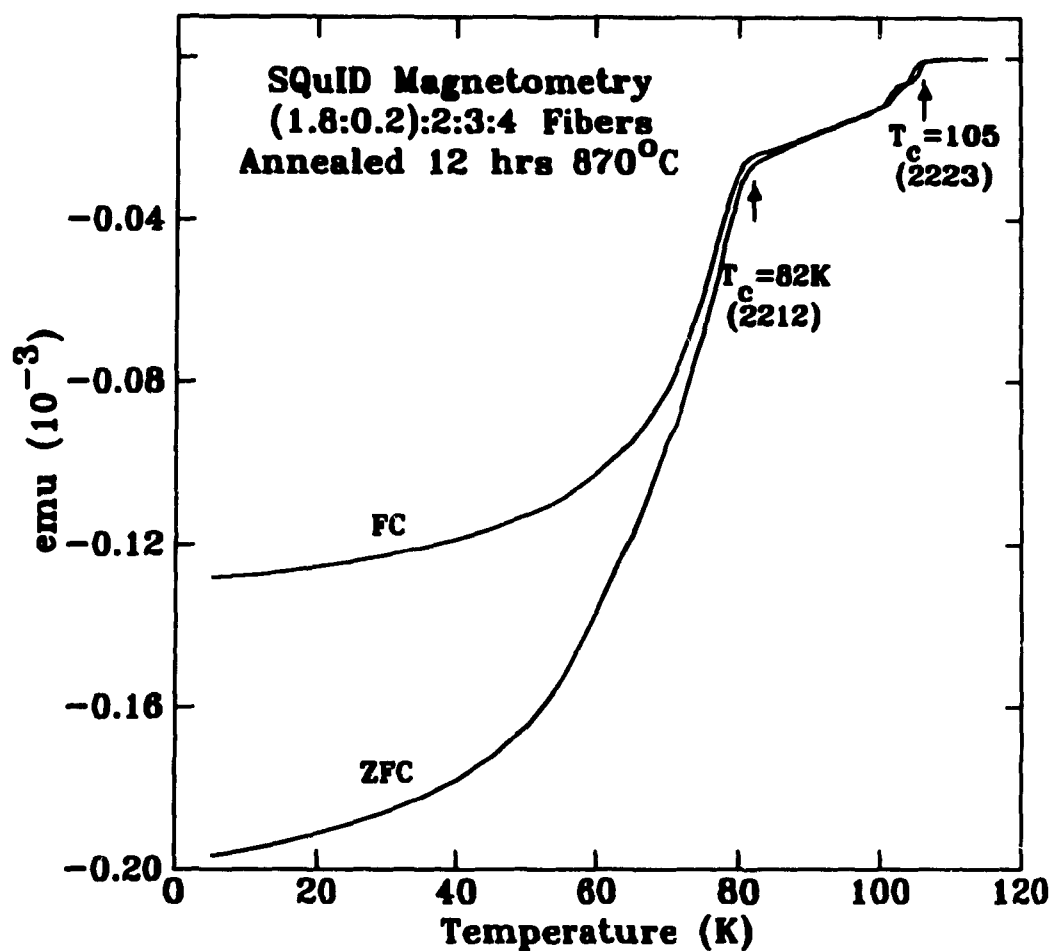


Figure 4.37: Magnetization curve for (1.8:0.2):2:3:4 fibers annealed at 870°C for 12 hours. Superconducting transitions are visible at 105 K and 82 K. The field cooled and zero-field cooled curves are labelled FC and ZFC, respectively.

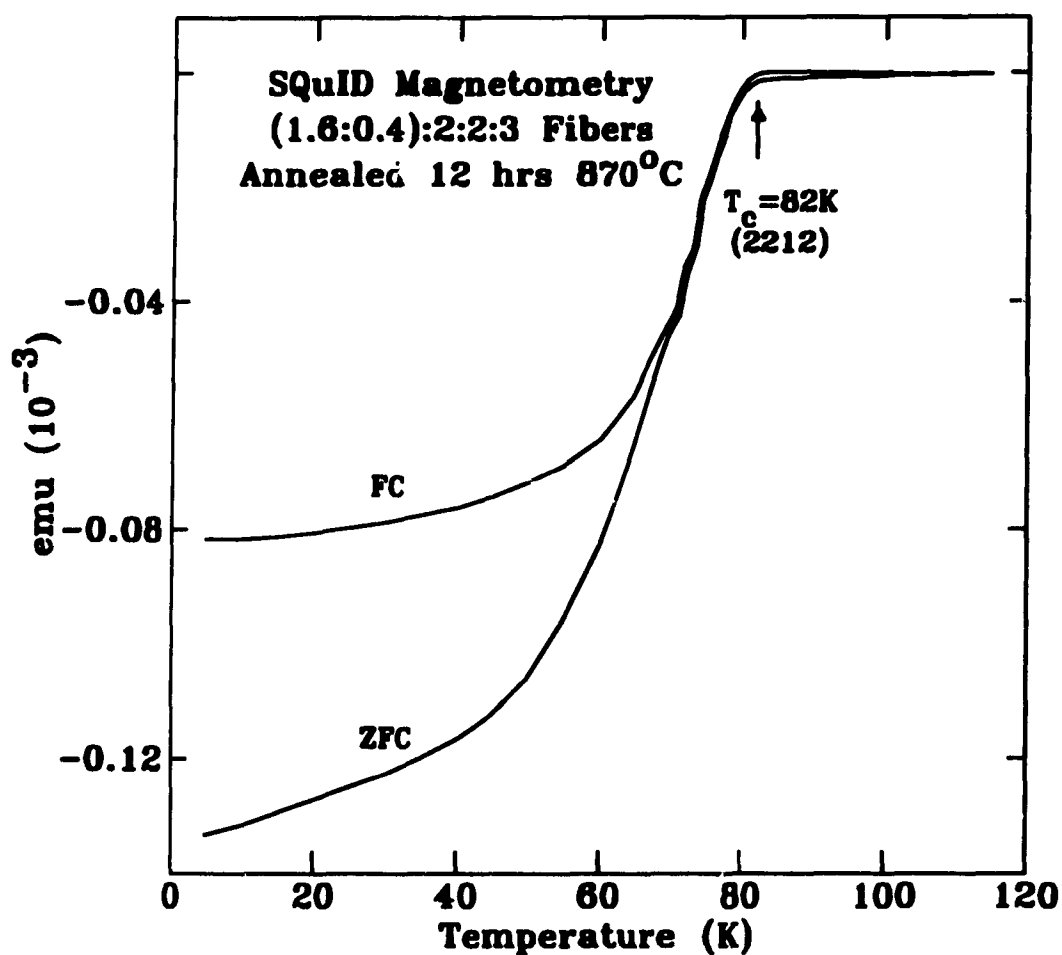


Figure 4.38: Magnetization curve for (1.6:0.4):2:2:3 fibers annealed at 870°C for 12 hours. A superconducting transition is visible at 82K. The field cooled and zero-field cooled curves are labelled FC and ZFC, respectively.

Chapter 5

Conclusions

Bismuth-based amorphous precursor fibers were made by melt extraction by adapting a technique originally designed for casting of fine metallic glass fibers. The extracted Bi-Sr-Ca-Cu-O fibers were subsequently transformed into high T_c superconductors by heat treatment in air. The as-made fibers, the precursor crystalline phases, and the high T_c phases were characterized.

Fiber dimensions ranged from 0.7 μm to 100 μm in diameter and 0.2 cm to 5 cm in length. Median dimensions were approximately 30 μm in diameter and 1.5 cm in length. The fibers were brittle but could be easily handled with fine tweezers. As-made fibers were approximately 80% ($\pm 10\%$) amorphous with the remainder being composed of crystalline calcium oxide (CaO) that precipitated on solidification. The results of characterization performed on these fibers were consistent with other rapid solidification work on Bi-Sr-Ca-Cu-O compounds.

The amorphous fibers were found to crystallize into the 2201 low T_c phase and a BCC solid-solution phase (lattice parameter = 4.25 Å). The simpler and less ordered BCC phase formed preferentially but eventually transformed to the 2201 phase after prolonged annealing. The samples underwent a series of exotherms (from 730 K to 880 K) after passing through the glass transition ($T_g \simeq 685$ K). The 2201 phase is seen immediately after the initial crystallization, in contrast to the findings of Nassau *et al.* (1989) and Tessier (1991).

Annealing at higher temperatures (1125 K to 1145 K) transformed the fibers into the 2212 and 2223 superconducting phases ($T_c=85$ K and 110 K respectively). Fibers with diameters as small as 1 μm were crystallized to form continuous filaments of single-grain chains. The crystallized fibers proved very difficult to handle due to their increased brittleness. As much as possible of the required manipulation must be performed while the fibers are in the as-made amorphous state.

No texturing was apparent in the annealed fibers. The volume fraction of 2223 phase was found to increase with initial compositions rich in calcium and copper and/or with lead substituted for bismuth. The consistent occurrence of calcium and copper rich impurity phases near 2223 crystal grains strongly suggests that calcium and copper diffuse into 2212 grains to form the 2223 compound. Individual grains of the 2212 and 2223 phases exhibited preferential growth in the a-b plane. Intergrowths of 2212 and 2223 phases and the incommensurate modulation along the a-b plane characteristic of the Bi-Sr-Ca-Cu-O compounds were observed. The crystallization of the fibers into the high T_c phases is consistent with that of samples prepared by more conventional rapid solidification techniques such as splat or roller quenching.

Fibers of initial composition (1.8:0.2):2:3:4 annealed at 1145 K for 12 hours show superconducting transitions at 82 K and 105 K corresponding to the 2223 and 2212 phases. The volume fractions of 2212 and 2223 phases were determined to have a lower limit of 30% and 5% respectively.

The physical characteristics of the as-made and annealed fibers prepared in this work are similar to those fabricated by gas-jet fiberization (Miller *et al.*, 1990). Such fibers have already been successfully incorporated into metal-high T_c superconductor multifilamentary composites to form flexible wires (see Section 3.9). This technique might be successfully applied using fibers made by the melt extraction method.

More processing is required to enhance texturing of crystal grains along the a-b plane in the annealed fibers. This will increase the critical currents of conductors made from these fibers. The initial composition used for precursor pellets must be optimized to allow maximum conversion to the 2223 phase. This would involve deter-

mining the elemental loss during fiberization and further investigation of the amount of lead (or other) substitution required. Improvements to the fiberization technique are needed to increase the yield of useful fibers. Parameters such as wheel speed, melt temperature, and feed rate can be varied to enhance production of fibers with the desired dimensions.

While this research has demonstrated the feasibility of fabricating superconducting Bi-Sr-Ca-Cu-O fibers by melt extraction, further work as described above is necessary before before this technology can be implemented in practical applications.

References

- Abrikosov, A. 1957. *Soviet Phys.-JETP*, **5**, 1174.
- Asthana, A., Han, P., Xu, Z., Chang, L., Payne, D., and Gilbert, P. 1991. *Physica*, **C174**, 33.
- Bansal, S., Bansal, T., Jha, A., and Mendiratta, R. 1991. *Physica*, **C173**, 260.
- Bardeen, J., Cooper, L., and Schrieffer, J. 1957. *Physical Review*, **108**, 1175.
- Batlogg, B., Cava, R., Jarayaman, A., van Dover, R., Kourouklis, G., Sunshine, S., Murphy, D., Rupp, L., Chen, H., White, A., Short, K., Muijsce, A., and Rietman, E. 1987a. *Physical Review Letters*, **58**, 2333.
- Batlogg, B., Kourouklis, G., Weber, W., Cava, R., Jayaraman, A., White, A., Short, K., Rupp, L., and Reitman, E. 1987b. *Physical Review Letters*, **59**, 912.
- Bednorz, J. and Müller, K. 1986. *Zeitschrift für Physik*, **B64**, 189.
- Bhan, S., Khan, Y., and Rothaemel, B. 1989. *Supercond. Sci. Technol.*, **2**, 265.
- Brodkey, R. 1967. *The Phenomena of Fluid Motions*, Chapter 17. Addison-Wesley Publishing Company, Don Mills.
- Cava, R. 1990a. *Science*, **247**, 656.
- Cava, R. 1990b. *Scientific American*, **263**(2), 42.
- CRC 1990. *Handbook of Chemistry and Physics*. CRC Press, Inc., Cleveland, 71st edition. Edited by R.C. Weast.
- Gao, W., Li, S., Rudman, D., Yurek, G., and vander Sande, J. 1989. *Physica*, **C161**, 71.
- Ginzburg, V. and Landau, L. 1950. *Zh. Eksperim. i Teor. Fiz.*, **20**, 1064.
- Grader, G., Gyorgy, E., Gallagher, P., O'Bryan, H., D.W. Johnson, J., Sunshine, S., Zahurak, S., Jin, S., and Sherwood, R. 1988. *Physical Review*, **B38**, 757.
- Gurvitch, M. and Fiory, A. 1987. *Physical Review Letters*, **59**, 1337.
- Gygax, S., Xing, W., Rajou, D., and Carzon, A. 1989. *Physica*, **C162-164**, 1551.
- Hazen, R. 1988. *Scientific American*, **258**(6), 74.
- Hinks, D., Solderholm, L., D.W. Capone, II, Mitchell, A., and Shi, D. 1988. *Applied Physics Letters*, **53**, 423.

- Kajitani, T., Kusaba, K., Kobayashi, M., Syono, Y., Williams, T., and Hirabayashi, M. 1988. *Japanese Journal of Applied Physics Letters*, **27**, L587.
- Khare, N., Walia, D., Reddy, G., Ojha, V., Kataria, N., Tomar, V., and Gupta, A. 1989. *Supercond. Sci. Technol.*, **1**, 1237.
- Kittel, C. 1986. *Introduction to Solid State Physics*, Chapter 12. John Wiley & Sons, Inc., Toronto, sixth edition.
- Knauf, N., Harnischmach, J., Müller, R., Borowski, R., and Wohlleben, D. 1991. *Physica*, **C173**, 414.
- Komatsu, T., Hirose, C., Ohki, T., Sato, R., and Matusita, K. 1990. *Applied Physics Letters*, **57**, 183.
- Komatsu, T., Imai, K., Sato, R., Matusita, K., and Yamashita, T. 1988a. *Japanese Journal of Applied Physics*, **27**, L533.
- Komatsu, T., Sato, R., Imai, K., Matusita, K., and Yamashita, T. 1988b. *Japanese Journal of Applied Physics*, **27**, L550.
- Kumakura, H., Togano, K., Dietderich, D., Maeda, H., Kase, J., and Morimoto, T. 1991. *IEEE Transactions on Magnetics*, **27**, 1250.
- LeBeau, S., Righi, J., Ostenson, J., Sanders, S., and Finnemore, D. 1989. *Applied Physics Letters*, **55**, 292.
- London, F. and London, H. 1935. *Proc. Roy. Soc. (London)*, **A149**, 71.
- Maeda, H., Tanaka, Y., Fukutomi, M., and Asano, T. 1988. *Japanese Journal of Applied Physics*, **27**, 209.
- Maringer, R. and Mobley, C. 1975. U.S. Patent No. 3.871.439.
- Marshall, G. 1986. Thermal annealing and superconductivity in Zr-based metallic glasses. Master's thesis, McGill University, Montréal, Québec.
- Matheis, D. and Snyder, R. 1990. *Powder Diffraction*, **5**(1), 8.
- Matsui, Y., Maeda, H., Tanaka, Y., and Horiuchi, S. 1988. *Japanese Journal of Applied Physics*, **27**, L372.
- Meissner, W. and Ochsenfeld, R. 1933. *Naturwissenschaften*, **21**, 787.
- Michel, C., Hervieu, M., Borel, M., Grandin, A., Deslandes, F., Provost, J., and Raveau, B. 1987. *Zeitschrift für Physik*, **B68**, 4007.
- Miller, T., Sanders, S., Ostenson, J., and Finnemore, D. 1990. *Applied Physics Letters*, **56**, 548.

- Miller, T., Schwartzkopf, L., Ostenson, J., Finnemore, D., Righi, J., Gleixner, A., and Zeigler, D. 1991. *IEEE Transactions on Magnetics*, **27**, 909.
- Minami, T., Akamatsu, Y., Tatsumisago, M., Tohge, N., and Kowada, Y. 1988. *Japanese Journal of Applied Physics*, **27**, L777.
- Nassau, K., Miller, A., Gyorgy, E., and Siegrist, T. 1989. *Journal of Materials Research*, **4**, 1330.
- Ong, N. 1990. *Physical Properties of High-Temperature Superconductors II*. World Scientific, Singapore. Edited by D.M. Ginsberg.
- Onnes, K. 1911. *Akad. van Wetenschappen*, **14**(113), 818. Amsterdam.
- Qiao, G., Zhang, J., Huang, J., Jiang, M., Ge, Y., Wang, Y., and Hu, Z. 1989. *Physica*, **C162-164**, 907.
- Richter, R. 1988. *Quantum Corrections to the Conductivity of Simple Metallic Glasses*. PhD thesis, McGill University, Montréal, Québec.
- Rudkowski, P., Rudkowska, G., and Ström-Olsen, J. 1991. *Materials Science and Engineering*, **A133**, 158.
- Schrieffer, J., Wen, X., and Zhang, S. 1988. *Physical Review Letters*, **60**, 944.
- Schrieffer, J., Wen, X., and Zhang, S. 1989. *Physical Review*, **B39**, 11663.
- Sheng, Z. and Hermann, A. 1988. *Nature*, **332**(55), 138.
- Shi, D., Boley, M., Chen, J., Xu, M., Vandervoort, K., Liao, Y., Zangvil, A., Akujieze, J., and Segre, C. 1989a. *Applied Physics Letters*, **55**, 699.
- Shi, D., Tang, M., Hash, M., Vandervoort, K., Claus, H., and Lwin, Y. 1989b. *Physical Review*, **B40**, 2247.
- Shi, D., Tang, M., Vandervoort, K., and Claus, H. 1989c. *Physical Review*, **B38**, 9091.
- Singh, R. and Zacharias, E. 1990. *Journal of Physics D: Applied Physics*, **23**, 199.
- Steglich, F. 1988. *Materials and Mechanisms of Superconductivity*. North-Holland, Amsterdam. *Physica* **C153-155**. Edited by J. Müller and J.L. Olsen.
- Sunshine, S., Siegrist, T., Schneemeyer, L., Murphy, D., Cava, R., Batlogg, B., van Dover, R., Fleming, R., Glarum, S., Nakahara, S., Farrow, R., Krajewski, J., Zahurak, S., Waszczak, J., Marshall, J., Marsh, P., L.W. Rupp, J., and Peck, W. 1988. *Physical Review*, **B38**, 893.
- Tarascon, J., McKinnon, W., Barboux, P., Hwang, D., Bagley, B., Greene, L., Hull, G., LePage, Y., Stoffel, N., and Giroud, M. 1988. *Physical Review*, **B38**, 8885.

- Tessier, P. 1991. High- T_c Bi oxides by crystallization of an amorphous precursor. Master's thesis, McGill University, Montréal, Québec. Unpublished.
- Tietz, L., Carter, C., Lathrop, K., Russek, S., and Buhrman, R. 1989. *Journal of Materials Research*, **4**, 1072.
- Timusk, T. and Tanner, D. 1990. *Physical Properties of High-Temperature Superconductors II*. World Scientific, Singapore. Edited by D.M. Ginsberg.
- Tinkham, M. 1975. *Introduction to Superconductivity*. International Series in Pure and Applied Physics. McGraw-Hill, Inc., New York.
- Uemura, Y., Le, L., Luke, G., Sternlieb, B., Brewer, J., Kadano, R., Keifl, R., Kretzmann, S., and Riseman, T. 1989. *Physica*, **C162-164**, 857.
- Wheatley, J., Hsu, T., and Anderson, P. 1988. *Nature*, **333**, 121.
- Wu, M., Ashburn, J., Torng, C., Hor, P., Meng, R., Gao, L., Huang, Z., Wang, Y., and Chu, C. 1987. *Physical Review Letters*, **58**, 908.
- Xu, Z., Han, P., Chang, L., Asthana, A., and Payne, D. 1990. *Journal of Materials Research*, **5**, 39.
- Yoshimura, M., Sung, T., Nakagawa, Z., and Nakamura, T. 1989. *Journal of Materials Science Letters*, **8**, 687.
- Yvon, K. and François, M. 1989. *Zeitschrift für Physik*, **B76**, 413.
- Zheng, H., Hu, Y., and Mackenzie, J. 1991. *Applied Physics Letters*, **58**, 1679.
- Zheng, H., Xu, R., and Mackenzie, J. 1989. *Journal of Materials Research*, **4**, 911.
- Zhuang, H., Kozuka, H., and Sakka, S. 1989. *Japanese Journal of Applied Physics*, **28**, L1805.
- Zou, Z. and Anderson, P. 1988. *Physical Review*, **B37**, 627.